UNIVERSITÄT BONN
Physikalisches Institut

Search for Excited Leptons in ep Scattering at HERA Using the ZEUS Detector

von

Ainas Weber

A search for heavy excited electrons and neutrinos has been performed with the ZEUS detector at HERA. The ep scattering data used were taken at a centre-of-mass energy of 318 GeV in the years 1998–2000. Excited electrons have been searched for in e^-p and e^+p collisions corresponding to integrated luminosities of 16.7 pb^{-1} and 66.1 pb^{-1}, respectively. The decay channels $e^* \to e\gamma$, $e^* \to \nu W \to \nu q\bar{q}'$ and $e^* \to eZ \to eq\bar{q}$ have been considered. Excited neutrinos have been sought in the e^-p data set via the decay channels $\nu^* \to \nu\gamma$, $\nu^* \to eW \to eq\bar{q}'$ and $\nu^* \to \nu Z \to \nu q\bar{q}$. The event selection has been performed employing both fixed cuts and a probability-based method as alternatives, with the latter yielding better overall performance. No evidence for an e^* or ν^* signal is observed in any of the channels analysed. Upper limits (95 % confidence level) as a function of the excited-lepton mass have been set on the cross section times the branching ratio, $\sigma \times \mathrm{BR}$, and on the coupling over the compositeness scale, f/Λ. In many cases, these limits extend up to higher masses and are more stringent than the existing ones.

Post address:
Nussallee 12
53115 Bonn
Germany

BONN-IR-2002-05
Bonn University
March 2002
ISSN-0172-8741

UNIVERSITÄT BONN
Physikalisches Institut

Search for Excited Leptons in *ep* Scattering at HERA Using the ZEUS Detector

von
Ainas Weber

Dieser Forschungsbericht wurde als Dissertation von der Mathematisch-Naturwissenschaftlichen Fakultät der Universität Bonn angenommen.

1. Referent: Prof. E. Hilger
2. Referent: Prof. N. Wermes

Tag der Promotion: 14. 03. 2002

Contents

Chapter 1

Introduction

Apparently simple questions can be difficult to answer. One such question is: What are the smallest entities in nature? This problem has been troubling thinkers and scientists for quite a while. Our present notion of elementarity is represented by the Standard Model (SM) of particle physics. The SM contains more than 20 particles (plus their antiparticles) that are regarded as fundamental: leptons and quarks, which have half-integral spin and therefore are fermions, and gauge bosons, which mediate the fundamental interactions. In addition, the so-far undiscovered Higgs boson is believed to account for the particle masses.

During the past 100 years, it was discovered several times that microscopic objects once believed to be elementary were in fact composite. For particle accelerators with higher and higher beam energies have made it possible to probe smaller and smaller constituents of matter. What reason do we have to expect no further layer of structure than the smallest presently known? Why should leptons and quarks be the final answer?

There exist electrically charged and uncharged leptons. The latter are the neutrinos. The lightest charged lepton is the electron. This thesis presents several searches for heavy excited states of electrons, e^*, and neutrinos, ν^*. The discovery of such excited states would provide unambiguous evidence that electrons and neutrinos are composite rather than elementary particles.

As will be discussed in Chapter 2, it is not only the fundamental interest in even smaller constituents of matter that has motivated theoretical models proposing fermion compositeness, but also specific shortcomings of the Standard Model that are hoped to be overcome.

The experimental setup will be described in Chapter 3. At the electron-proton collider HERA, excited leptons with masses up to the kinematic limit of 318 GeV could be produced directly via t-channel exchange of a gauge boson. Once produced, the excited leptons would decay into standard leptons and gauge bosons, detectable by ZEUS. In

Chapter 4, the event kinematics and the reconstruction of characteristic quantities will be laid out.

In order to search for heavy excited leptons, one needs to have an idea how the angles and momenta of their decay particles are distributed. For that purpose, a Monte Carlo generator, which is based on a specific phenomenological compositeness model, is employed to simulate the production and decays of excited leptons. The simulated events are used to determine the efficiency of the selection criteria. Furthermore, known sources of background are simulated, i.e. SM processes leading to similar experimental signatures as the types of reactions searched for.

It is impossible to decide whether an individual data event showing the characteristic features of an excited-lepton decay is actually the sign of an excited lepton or due to some background process. Thus the discovery of a signal is possible on a statistical basis only: in a narrow mass region, one would observe a significant excess of candidate events over the expected number of background events.

The data analysed for the search presented here were collected with the ZEUS detector in the years 1998–2000 and correspond to an integrated luminosity of $82.8\,\mathrm{pb}^{-1}$. In 1998 and in the first half of 1999, the HERA collider operated with electrons and protons. After that, the lepton beam was switched to positrons. The subset of data collected during the first running period corresponds to an integrated luminosity of $16.7\,\mathrm{pb}^{-1}$. Excited neutrinos have been sought only in the electron-proton data, since the ν^* production cross-section is expected to be much higher in e^-p than in e^+p collisions because of the W exchange involved. For e^* production, the charge sign of the lepton beam does not matter. Consequently, the e^* search has been performed using the whole data set 1998–2000.

In both the e^* and the ν^* searches, three decay modes have been considered, comprising decays with any of the three gauge bosons γ, Z and W in the final state (see Chapter 5). To select excited-lepton candidates, two different methods have been applied. Both of them start with a preselection by cuts, chosen to test the agreement between the data and the background simulation in the respective channel. The first method then selects events by a set of fixed cuts, whereas the second selection method works on a probabilistic basis. Derived from a set of characteristic variables, every event is assigned a total probability value. This probability is then used as a single cut variable. The probability method is shown to yield higher sensitivity than the cut selection.

With both selection methods, the result of all searches is negative: In none of the six decay channels an excess of candidates over the expected background is observed, i.e. no evidence for any excited lepton is found. This result, however, does not completely rule out lepton compositeness, since the masses of the excited states could lie beyond the centre-of-mass energy of HERA. Even in the mass range tested here, excited leptons could well exist, but with a production cross-section too small to be detectable given the available amount of data.

The search results can thus be used to place upper limits on the cross section for e^* and ν^* production in ep collisions, as will be described in Chapter 6. The limits are derived from the numbers of observed events, of expected events, the size of the data samples and the selection efficiencies. Only the latter quantity depends on the theoretical model used.

Under more model-specific assumptions, the cross-section limits can be transformed into upper limits on the coupling strength between excited and standard leptons. These limits allow for a comparison with the corresponding results from other collider experiments. Currently, the HERA collider experiments set the most stringent limits for e^* and ν^* masses above 200 GeV. The exclusion limits presented here also supersede corresponding limits from former ZEUS publications, which were derived using a smaller amount of data.

With the present experimental data, there is no evidence for a substructure inside electrons or neutrinos. Yet lepton compositeness remains a compelling hypothesis, with a possible discovery being left to the forthcoming luminosity upgrade of HERA or to other future experiments.

Chapter 2

Theoretical foundations

This chapter starts with an outline of the key concepts and contents of the Standard Model of electroweak and strong interactions. Subsequently, known deficiencies of that model as well as alternative approaches are discussed. What follows is an introduction to the concept of compositeness, which has partly been motivated by shortcomings of the prevalent theory. The final section of the chapter deals with the phenomenological Hagiwara model which constitutes the specific theoretical basis for the analysis presented in this thesis.

2.1 The Standard Model

2.1.1 Fundamental particles and interactions

The present notion of the smallest particles and their interactions is represented by the Standard Model (SM) of particle physics [1]. What appeared as an incoherent "zoo" of observational facts some 40 years ago, has been reduced to a relatively small number of fundamental particles and forces in the SM.

According to the SM, the basic constituents of matter are leptons and quarks – structureless, point-like fermions (spin 1/2). Both leptons and quarks are organised in three families, as listed in the table below. Stated as well are the particles' electric charges, Q, expressed in multiples of the elementary charge:

				Q
Leptons	ν_e	ν_μ	ν_τ	0
	e	μ	τ	-1
Quarks	u	c	t	$+2/3$
	d	s	b	$-1/3$

When counting the number of fundamental fermions, the six quark flavours are to be multiplied by a factor of three, because each of the quarks can carry three different colour charges (denoted by "red", "green" and "blue"). Strictly speaking, the resulting 24 particles constitute only half of the fundamental fermions, since for each of them an anti-particle exists.

Formulated within the framework of relativistic quantum field theory, the SM is built upon a symmetry principle, namely the invariance of the theory under local gauge transformations. The corresponding group structure is $\mathrm{SU}(3)_c \times \mathrm{SU}(2)_\mathrm{L} \times \mathrm{U}(1)_\mathrm{Y}$, accounting for the strong, weak and electromagnetic interactions.[1] The quanta associated to the gauge fields are the fundamental bosons listed below.[2] The gauge bosons are point-like particles carrying spin 1. The electrically neutral gauge bosons are their own anti-particles, and W^+ is the anti-particle of W^-.

interaction	boson	Q	$m\,(\mathrm{GeV})$
electromagnetic	γ	0	0
weak	$W^\pm$	±1	80.42
	Z	0	91.188
strong	8 gluons	0	0

$\mathrm{SU}(3)_c$ is the symmetry group of the strong colour force. The associated gauge field is the gluon colour octet G^a_ν. To participate in strong interactions, a particle must carry colour charge, which is the case for quarks and gluons but not for leptons. The theory describing the strong interactions is quantum chromodynamics (QCD).

The electromagnetic and weak interactions are unified by the Glashow-Weinberg-Salam theory [3–5]. The underlying symmetry group is $\mathrm{SU}(2)_\mathrm{L} \times \mathrm{U}(1)_\mathrm{Y}$. The group $\mathrm{SU}(2)_\mathrm{L}$ describes transformations of left-handed multiplets of the weak isospin, whereas $\mathrm{U}(1)_\mathrm{Y}$ is related to phase transformations of the weak hypercharge, Y. Associated to the groups $\mathrm{SU}(2)_\mathrm{L}$ and $\mathrm{U}(1)_\mathrm{Y}$ are an isotriplet of vector fields, $\vec{W}_\nu$, and an isoscalar vector field, B_ν, respectively. From the mixing of these fields arise the photon field, A_ν, and the weak gauge fields, $W^\pm_\nu$ and Z_ν.

All electrically charged particles, fermions as well as the $W^\pm$ bosons, are subject to electromagnetic interactions. Both leptons and quarks participate in weak interactions. However, in case of $W^\pm$ exchange, that holds exclusively for their left-handed states.

[1] The fourth fundamental interaction, gravity, is not a genuine part of the SM. One still lacks a proper quantum theory of gravity, which would allow for a unified theory of all four interactions. That situation, however, poses no serious problem for the SM, because for sub-atomic phenomena the gravitational force can savely be neglected.

[2] The photon and gluon masses are zero per definition. The W and Z masses are stated up to the last significant digit, according to [2].

Other than $U(1)_Y$, the groups $SU(2)_L$ and $SU(3)_c$ are non-Abelian, allowing for self-couplings of the respective gauge bosons. In case of QCD, the self-couplings and the masslessness of the gluons give rise to quark "confinement". The potential energy between quarks increases proportionally to their mutual distance, so that quarks, which carry colour charge, are not observed as isolated particles. Rather, they are confined to colourless bound states, which are baryons (qqq) or mesons ($q\bar{q}$). For similar reasons, gluons are not directly observable.

Generally speaking, gauge symmetry requires the bosons associated to the gauge fields to be massless. The $W^{\pm}$ and Z bosons, however, have non-zero masses. Rendering these bosons massive and, at the same time, preserving the gauge invariance of the theory is achieved by the mechanism of spontaneous symmetry breaking [6–8]: gauge bosons and fermions attain their masses by interacting with the scalar Higgs field. As a consequence, an additional massive particle is introduced, the scalar Higgs boson.

The values of the particle masses are not predicted by theory, but have to be determined experimentally. The masses of the charged leptons are 0.511 MeV (e), 105.7 MeV (μ) and 1777.0 MeV (τ) [2].[3] According to the current SM, neutrinos are massless. However, recent experiments have yielded evidence for neutrino oscillations [9, 10]. Such mixing between the different neutrino flavours (ν_e, ν_μ, ν_τ) requires the neutrinos to have small non-zero masses at most of order eV. The present upper bounds on the neutrino masses, however, are 3 eV (ν_e), 0.19 MeV (ν_μ) and 18.2 MeV (ν_τ) [2].

The quark masses are not well defined, as direct measurements are impossible due to quark confinement. Instead, the quark masses are inferred from the masses of bound states, which is no unequivocal business. In any case, similar to the masses of the charged leptons, the resulting masses do increase when stepping to a "higher" family.

In the SM description lepton flavour is conserved individually for each family. This conservation law is not due to an exact symmetry, but has been introduced ad hoc according to observational facts. For the charged leptons, no experimental indication of lepton-flavour violation has been found so far [11]. In contrast to that, the recently observed neutrino oscillations demonstrate that lepton flavour is not conserved in the neutrino sector.

Charged weak interactions ($W^{\pm}$ exchange) allow for transitions between the different quark flavours. The associated mixing parameters, three real angles and one phase, are contained in the CKM matrix [12, 13]. Those parameters are not predicted by the SM but need to be put in "by hand".

The observations of top quarks [14, 15] and tau neutrinos [16] have constituted the most recent steps towards experimental evidence for all fundamental fermions and gauge bosons of the SM. No particles that would not fit into the scheme provided by the SM have been found up to now. However, the Higgs boson has not been discovered yet. Thus, the Higgs mechanism, one of the crucial ingredients of the SM, still lacks experimental confirmation.

[3] The electron and muon masses are actually known to much higher accuracy than stated here.

2.1.2 Shortcomings and alternative concepts

The theories of the electroweak and strong interactions described above have been widely accepted as the 'Standard' Model of particle physics due to a number of convincing reasons. During the past three decades, the predictions of the SM have been subjected to numerous experimental tests. Apart from the recently found evidence for neutrino oscillations [9, 10], the agreement between the theoretical description and the observational facts is striking [1]. What counts as well in favour of the SM is its formulation as a renormalisable gauge theory, because establishing the fundamental interactions on the basis of a symmetry principle represents an appealing theoretical approach.

Despite its enormous successes and undoubted virtues, however, the SM is faced with a number of unsolved problems [1, 17]. A theory of the fundamental laws of nature is usually expected to accomplish complete unification of all interactions, including gravity. Moreover, such a theory should reduce the fundamental particles to a number as small as possible. Given the latter criterion, the SM does not score too well: six leptons plus 18 quarks plus the respective antiparticles plus 12 gauge bosons does not seem so small a number.

The SM offers no explanation for the organisation of leptons and quarks in three families. The family structure is merely put up reflecting the observational facts. The same holds for the spectrum of lepton and quark masses, which are not predicted by the SM but have to be taken from experiment. Furthermore, in the light of the recent findings on neutrino oscillations, the neutrino sector of the SM obviously requires modification, which would need to account for the non-zero neutrino masses and the mixing parameters.

In addition to the fermion masses, several other parameters are undetermined by theory, among them the four parameters of the CKM matrix and the three gauge coupling strengths. Requiring those parameters as experimental input rather than providing an explanation for their values is an unsatisfactory feature of the SM.

When considering the properties of quarks and leptons, the question arises why those particles do behave so similarly in certain respects. Quarks and leptons share multiples of the electric charge 1/3. Moreover, both types of particles exhibit the same behaviour with regard to weak interactions. No explanation for these similarities is offered by the SM.

The Higgs sector is a pending question mark, still lacking experimental confirmation. Failing to discover the Higgs boson even at future collider experiments would mean a serious challenge of the SM, since the Higgs mechanism is a vital element of the electroweak theory.

In the face of these deficiencies, the picture of the fundamental laws provided by the SM cannot be regarded as the final answer. To overcome the shortcomings, numerous models have been proposed either as extensions of the SM or as complete alternatives [17].

The main concepts followed in constructing new models have been grand unification, supersymmetry, technicolour and compositeness. With regard to theoretical aspects, each of these concepts features specific virtues as well as specific problems. Some of the various models proposed are already ruled out by experimental facts. However, experimental support in favour of a particular model has not yet been revealed.

Grand unified theories incorporate unification of the electroweak and strong interactions by embedding the SM symmetry structure in a higher-rank gauge group (the simplest approach being SU(5)). One of the most prominent features of grand unified theories is the prediction of proton decay.

Supersymmetry (SUSY) [18] features a close connection between fermions and bosons. The simplest SUSY model is the Minimal Supersymmetric Extension to the Standard Model (MSSM), which doubles the fundamental particles of the SM by predicting a bosonic partner for every fermion and vice versa. None of these SUSY particles has been discovered in the numerous experimental searches performed up to now. A crucial test of the MSSM will be provided by the LHC. The supersymmetry principle has been incorporated in a variety of different models. Among those, supergravity and superstrings are worth mentioning, as they feature the unification of all four fundamental interactions.

Technicolour [19] has been invented to overcome the flaws of the Higgs sector. Instead of a scalar Higgs, technicolour theories feature Higgs particles being composite of fermions and antifermions. The latter are bound by a new non-Abelian gauge interaction, denoted as technicolour.

Compositeness [17, 20] is the theoretical approach constituting the prerequisite for the excited-lepton search presented here. The compositeness hypothesis questions the elementarity of leptons and quarks by proposing a further layer of substructure. If the fermions were composite objects rather than pointlike particles, heavy excited states could be produced in high-energy particle collisions. Experimental searches for excited fermions at particle colliders could therefore reveal unequivocal evidence for lepton or quark compositeness [21–25].

2.2 The compositeness hypothesis

2.2.1 Overview

During the past century, the ever increasing beam energies provided by particle accelerators led to repeated discoveries of substructures inside objects that were formerly believed to be elementary. Thus it is legitimate to be suspicious about the present notion of elementarity. Why should one expect no further layer of structure beyond the smallest

presently known? Is it sensible to believe that contemporary physics is in the unique historical situation of having ultimately revealed the smallest entities in nature?

For that reason, compositeness is a compelling hypothesis. In addition, the shortcomings of the SM pointed out in the previous section ask for an alternative theoretical approach. Compositeness has been regarded a promising candidate to explain some of the questions left open by the SM. They concern the hierarchical family structure of leptons and quarks as well as the large numbers of both arbitrary parameters and fundamental particles. Moreover, compositeness is hoped to provide an explanation for the similarities of leptons and quarks with respect to electric charge and weak-interaction properties.

Compositeness models are based on the idea that leptons and quarks are not elementary but consist of common constituents [20, 26–35]. The latter are conventionally denoted as "preons". Similar to the colour interaction of quarks, the preons are thought to be confined by a non-Abelian gauge interaction, which is usually referred to as "hypercolour" force. The models proposed frequently feature composite weak gauge bosons and composite Higgs particles as well. Moreover, there exist approaches employing the concepts of both SUSY and compositeness [36, 37].

A variety of models to construct quarks and leptons from fermionic and/or bosonic preons has been invented. As for the number of different preons proposed, the "rishon" model [38–40] constitutes the simplest approach, as it features only two fermionic preons (plus their anti-particles) carrying electric charges of 0 and 1/3, respectively. Quarks and leptons are each composed of three such preons. The heavy weak gauge bosons are composite as well.

The most economic prototype model involving both fermionic and bosonic preons is the "haplon" model [41], which contains four different types of preons (plus the respective anti-preons). Pairs of those are supposed to build up leptons and quarks as well as the heavy weak gauge bosons and, possibly, the Higgs boson. In contrast, the photon and gluons as well as the bosons mediating the hypercolor force are fundamental. A common feature of both the rishon and haplon models is the occurence of right-handed neutrinos.

The energy scale of the hypercolour interaction, Λ, must be much larger than the colour energy scale. Lower bounds on the size of Λ are given by a number of experimental results on electric and magnetic properties of the leptons, such as form factors, electric dipole moments and anomalous magnetic moments [17]. From those findings the compositeness scale is inferred to be at least of $\mathcal{O}(1\,\mathrm{TeV})$.[4]

Apart from general criteria for rating theories, such as testability and economy, any specific compositeness model has to be judged with respect to its potential to cure deficiencies

[4] The energy scale, Λ, can also be interpreted as a length scale. Employing the uncertainty relation, $\Lambda = 1\,\mathrm{TeV}$ then corresponds to a spatial dimension of roughly $10^{-18}\,\mathrm{m}$, i.e. one per mille of the proton radius.

of the SM without at the same time introducing serious novel problems. As outlined above, there exist preon models that succeed in reproducing at least one family of leptons and quarks with the appropriate quantum numbers. That has been achieved using economically small numbers of different preons.

However, none of the preon models proposed is fully convincing. For the unsolved problems remaining are too serious. The family structure has been incorporated in some models by means of excitation states, but no compelling reason for the structure observed has been provided. Moreover, no convincing explanation has been found for the fermion masses. For those reasons, no 'standard' preon model has been established.

As for the phenomenological side, the situation is different though. The compositeness model of Hagiwara et al. [42–44], which is described in more detail in the next section, has been widely used in the course of experimental excited-fermion searches. Being purely phenomenological, this model provides a basis for simulations and quantitative calculations, and thus for proper comparison of experimental bounds.

Judging from the number of publications, the greatest interest in compositeness models arose in the early 1980s. In recent years, a number of experimental findings motivated theorists to reconsider the idea of fermion substructure: CDF's excess of dijet events at high E_T [45], the excess of high-Q^2 events observed by H1 and ZEUS [46–48] and, most recently, BNL's apparent $g-2$ anomaly [49–54]. In all three cases, however, the claims made for 'new physics' could not be maintained.

Fermion substructure would give rise to the existence of excited states. Those could be produced directly in high-energy particle collisions. Despite the tight bounds on the compositeness scale, Λ, experimental searches for heavy excited fermions are worthwile. For the masses of such excited states could lie well below Λ. During the past decade, dedicated searches for excited electrons and neutrinos as well as for excited quarks have been carried out at the LEP (e^+e^-), HERA (ep) and Tevatron ($p\bar{p}$) colliders.

Searches for quark substructure have been the domain of the Tevatron experiments [45, 55–61]. Being sensitive to the electroweak rather than to the strong q^* couplings, the q^* searches performed at LEP and HERA are considered complementary to those employing $p\bar{p}$ collisions. Excited electrons and neutrinos, on the other hand, have been sought mainly at LEP and HERA [62–73]. In ep collisions at HERA (Sect. 3.1), excited electrons and neutrinos could be produced directly via t-channel exchange of a gauge boson, as depicted in Fig. 2.1.

The outcome of all excited-fermion searches performed in the different experiments has been negative so far. As a consequence, upper limits have been set on the respective production cross-sections. Furthermore, it has become conventional to derive upper limits on the excited-fermion couplings in the framework of a specific phenomenological model. The latter is presented in the next section.

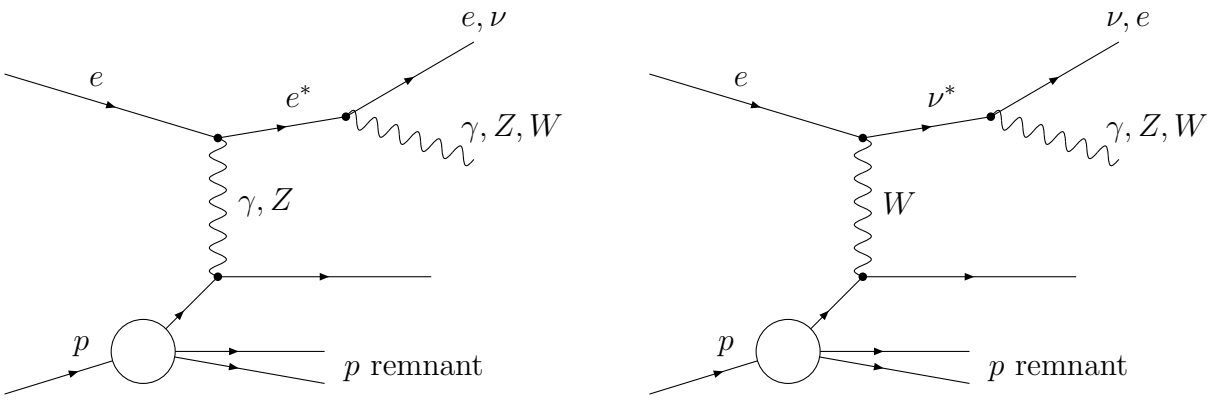

Figure 2.1: *Leading-order Feynman diagrams for the production of excited leptons in (inelastic) ep collisions, with subsequent decays to standard leptons and gauge bosons. Left: e^* production via γ/Z exchange. Right: ν^* production via W exchange.*

2.2.2 The Hagiwara model

Albeit not proposing a concept of the sub-lepton dynamics, the compositeness model of Hagiwara et al. [42–44] has gained broad popularity as a theoretical starting point for excited-lepton searches. Being purely phenomenological, that model provides a framework for the quantitative treatment of excited-lepton production and decays, including the programming of a Monte Carlo (MC) generator (Sect. 5.2.2).

The excited leptons are assumed to have spin and isospin 1/2 and to form both left-handed, l_L^*, and right-handed, l_R^*, weak isodoublets. The effective Lagrangian describing magnetic-moment type transitions between ordinary leptons, l_L, and excited states is given by[5]

$$\mathcal{L} = \frac{1}{\Lambda}\bar{l}_R^*\sigma^{\mu\nu}\left[gf\frac{\vec{\tau}}{2}\partial_\mu\vec{W}_\nu + g'f'\frac{Y}{2}\partial_\mu B_\nu\right]l_L + \text{h.c.}\,, \tag{2.1}$$

where Λ is the compositeness scale; $\vec{W}_\nu$ and B_ν are the $\mathrm{SU(2)_L}$ and $\mathrm{U(1)_Y}$ fields, respectively; $\vec{\tau}$ denotes the Pauli matrices, and $Y = -1/2$ is the hypercharge; g and g' are the SM electroweak coupling constants. Apart from Λ, the only free parameters are f and f'. Those are dimensionless weight factors[6] associated with the two gauge groups, their values depending on the underlying composite dynamics.

The total e^* or ν^* production cross-section is proportional to $(f/\Lambda)^2$. Therefore a specific value of f/Λ has to be chosen in order to calculate cross sections. For e^* production in

[5] The Lagrangian shown can be employed to describe $q \leftrightarrow q^*$ transitions as well. Moreover, it can be extended in a straight-forward way to also take into account colour interactions [43, 44].

[6] Being not quite precise, f and f' are commonly denoted as 'coupling constants' rather than as weight factors.

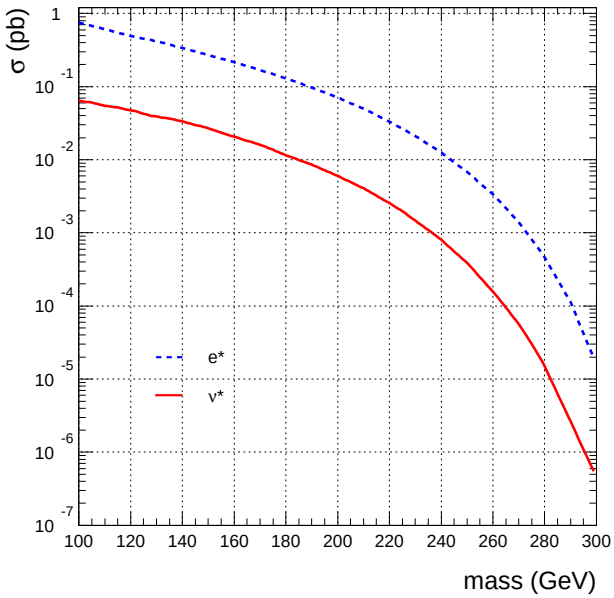

Figure 2.2: *Excited-electron (dashed curve) and excited-neutrino (solid curve) production cross-sections for e^-p collisions at 318 GeV centre-of-mass energy. The curves shown have been calculated with the HEXF MC generator (Sect. 5.2.2) assuming $f/\Lambda = 1/\,\mathrm{TeV}$; they have been used for deriving upper limits on f/Λ, as discussed in Sect. 6.1.*

ep collisions, roughly half of the cross section is contributed from elastic scattering. In contrast, ν^* production requires W exchange and thus proceeds inelastically only. Compared to ν^* (produced in e^-p collisions), the e^* cross section is higher by approximately one order of magnitude within the mass range accessible at HERA. In Fig. 2.2, e^* and ν^* cross sections calculated for e^-p collisions and $f/\Lambda = 1/\,\mathrm{TeV}$ are shown.

For e^* production, the charge sign of the lepton beam does not alter the cross section. Yet the situation is different for ν^*: compared to e^+p, the cross section for e^-p collisions is higher by about two orders of magnitude. That difference is partially explained by the different quark flavours taking part in the respective interaction. In addition, the cross section for e^+p is suppressed due to reasons of chirality.[7]

As for the decays of excited states to an ordinary lepton and a gauge boson, the partial widths are described by [43, 44]

$$\Gamma(l^* \to Vl) = \frac{\alpha}{4}\frac{M_*^3}{\Lambda^2} f_V^2 \left(1 - \frac{M_V^2}{M_*^2}\right)\left(1 + \frac{M_V^2}{2M_*^2}\right), \tag{2.2}$$

with $\alpha = 1/137$ denoting the electromagnetic coupling constant; M_* is the excited-lepton mass, and M_V is the mass of the respective gauge boson, $V = \gamma, W, Z$. The factors f_V associated to the three gauge bosons are given by

[7] That effect is similar to the high-Q^2 behaviour of charged-current cross sections (Sect. 4.1) in e^+p and e^-p collisions.

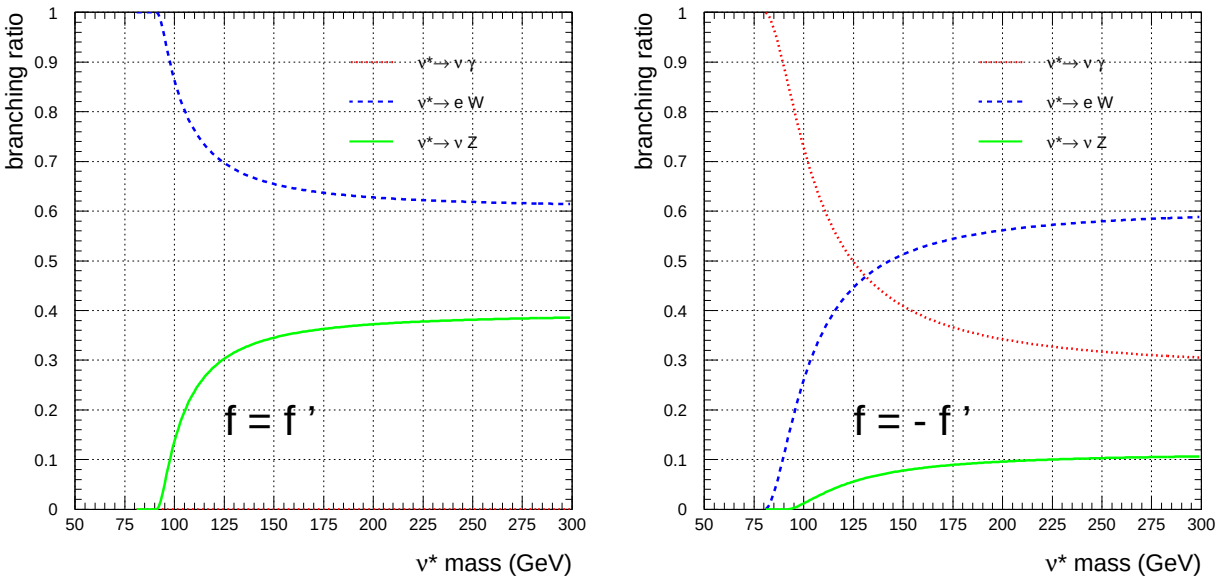

Figure 2.3: *Branching ratios of excited-neutrino decays. Left: $f = f'$, for which the photonic decay is suppressed. Right: $f = -f'$. The curves shown are identical to those for excited electrons when reversing the relations of f and f', i.e. the left (right) plot also displays the respective e^* branching ratios for $f = -f'$ ($f = f'$).*

$$f_\gamma = fT_3 + f'\frac{Y}{2}, \tag{2.3}$$

$$f_W = \frac{f}{\sqrt{2}\sin\theta_W}, \tag{2.4}$$

$$f_Z = \frac{fT_3\cos^2\theta_W - f'\frac{Y}{2}\sin^2\theta_W}{\sin\theta_W\cos\theta_W}, \tag{2.5}$$

where T_3 denotes the third component of the weak isospin of the excited lepton, and θ_W is the weak mixing angle. Assuming $\Lambda = 1\,\text{TeV}$, the resulting total widths are less than $1\,\text{GeV}$ for excited-lepton masses of up to about $500\,\text{GeV}$.

The branching ratios, $\text{BR}(l^* \to lV)$, of the individual decay modes are calculated from

$$\text{BR}(l^* \to lV) = \frac{\Gamma(l^* \to Vl)}{\sum_V \Gamma(l^* \to Vl)}. \tag{2.6}$$

Thus, the branching ratios depend only on the relation between the weight factors f and f'. As for experimental searches, it has been conventional to stick to the assumption $|f| = |f'|$ when deriving upper limits (Sect. 6.1). For excited electrons, the conventional assumption is $f = f'$, which allows for decays to all three gauge bosons. In contrast, for excited neutrinos, $f = f'$ as well as $f = -f'$ are considered separately. The latter

assumption allows for radiative ν^* decays, whereas $f = f'$ does not. Considering both cases rather than only $f = -f'$ for ν^* is due to the fact that $\nu^*\nu\gamma$ couplings may appear dubious, although they are imaginable if neutrinos contain charged constituents. In Fig. 2.3, the ν^* branching ratios according to the above formulae are depicted.

The $e^* \to e\gamma$ decay is expected to exhibit the following angular distribution [44]:

$$\frac{1}{\Gamma}\frac{\mathrm{d}\Gamma}{\mathrm{d}\cos\theta^*} \approx 1 + \cos\theta^* \,, \tag{2.7}$$

where θ^* denotes the polar angle between the incoming and the outgoing electron in the e^* rest frame. The corresponding angular distribution for e^* decays to heavy gauge bosons, $V = W, Z$, is given by

$$\frac{1}{\Gamma}\frac{\mathrm{d}\Gamma}{\mathrm{d}\cos\theta^*} \approx \frac{1 - \cos\theta^* + \frac{M_V^2}{2M_{e^*}^2}(1 + \cos\theta^*)}{2 + \frac{M_V^2}{M_{e^*}^2}} \,, \tag{2.8}$$

with θ^* now denoting the angle of the outgoing W or Z boson with respect to the electron beam, as measured in the e^* rest frame.

The Hagiwara model has been employed for generating excited-lepton MC samples with HEXF, as described in Sect. 5.2.2. These samples have been used for estimating selection efficiencies and reconstructed-mass resolutions (Sect. 5.6), which are needed as input to the limit-setting procedure (Sect. 6.1). The excited-lepton cross sections and branching ratios discussed above have been employed for the limit-setting as well.

Chapter 3

Experimental setup

3.1 The HERA collider

The HERA[1] accelerator complex [74] at DESY[2] in Hamburg consists of two independent storage rings operating with electrons[3] and protons, respectively. The rings are located in an underground tunnel of 6336 m circumference. There are four experimental halls. In two of them, housing the multi-purpose detectors H1 and ZEUS, head-on collisions of the beams are provided. The third experiment, HERMES, uses only the electron beam for studying polarised electron-nucleon scattering on a gas target. The fourth experiment, HERA-B, uses the proton beam-halo for scattering off a wire target.

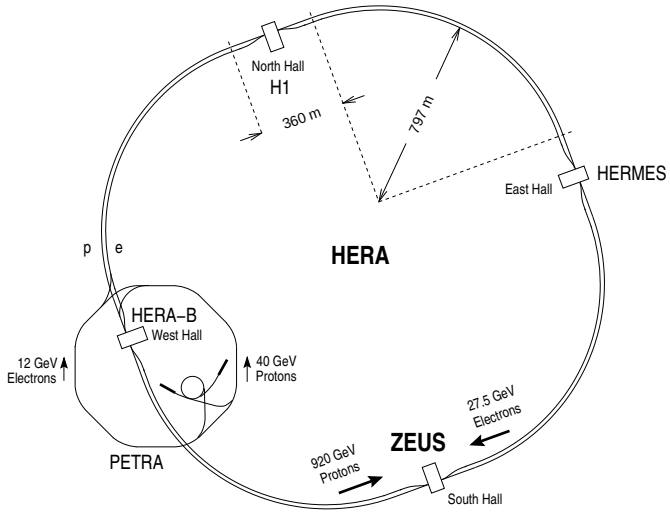

Figure 3.1: *Schematic view of the HERA accelerator complex.*

[1] Hadron-Elektron-Ring-Anlage

[2] Deutsches Elektronen-Synchrotron

[3] Throughout this thesis, if not stated otherwise, the term "electron" is used generically to refer to e^+ as well as e^-. Similarly, the term "neutrino" is used both for ν and $\bar{\nu}$.

Year	E_e [GeV]	E_p [GeV]	$\mathcal{L}$ [pb^{-1}]	
			e^-p	e^+p
1993	26.7	820	0.5	—
1994	27.5	820	0.3	3.0
1995–97	27.5	820	—	44.7
1998	27.5	920	4.6	—
1999	27.5	920	12.1	19.7
2000	27.5	920	—	46.4

Table 3.1: *Summary of HERA running periods, including the electron and proton beam-energies, E_e and E_p, as well as the integrated luminosity, $\mathcal{L}$, recorded by the ZEUS detector.*

Both storage rings were designed to accomodate up to 210 particle bunches. The time interval between two consecutive bunch crossings is 96 ns. At the ZEUS interaction region, the beamspot measures approximately 200 µm in horizontal and 50 µm in vertical direction. The 1σ length of the luminous region of about 10 cm is determined by the proton bunch-length.

Since 1998, HERA operated with electron and proton energies of 27.5 GeV and 920 GeV, respectively, resulting in a centre-of-mass energy of 318 GeV. In Table 3.1, the running parameters of the different data-taking periods are summarised. The analysis presented in this thesis is based on the ZEUS data recorded during the 1998 to 2000 running of HERA.

At the end of 2001, HERA resumed operation after one year of upgrade works intended to provide specific luminosities increased by a factor of about 3.5 for the collider experiments H1 and ZEUS. Furthermore, devices were installed to yield longitudinal polarisation of the electron beam in the interaction regions [75].

3.2 The ZEUS detector

3.2.1 Overview

The ZEUS detector is operated by an international collaboration of about 400 physicists. ZEUS is a multi-purpose detector system designed to measure as accurately as possible the energies and tracks of the final-state particles emerging from the high-energy *ep* collisions provided by HERA.

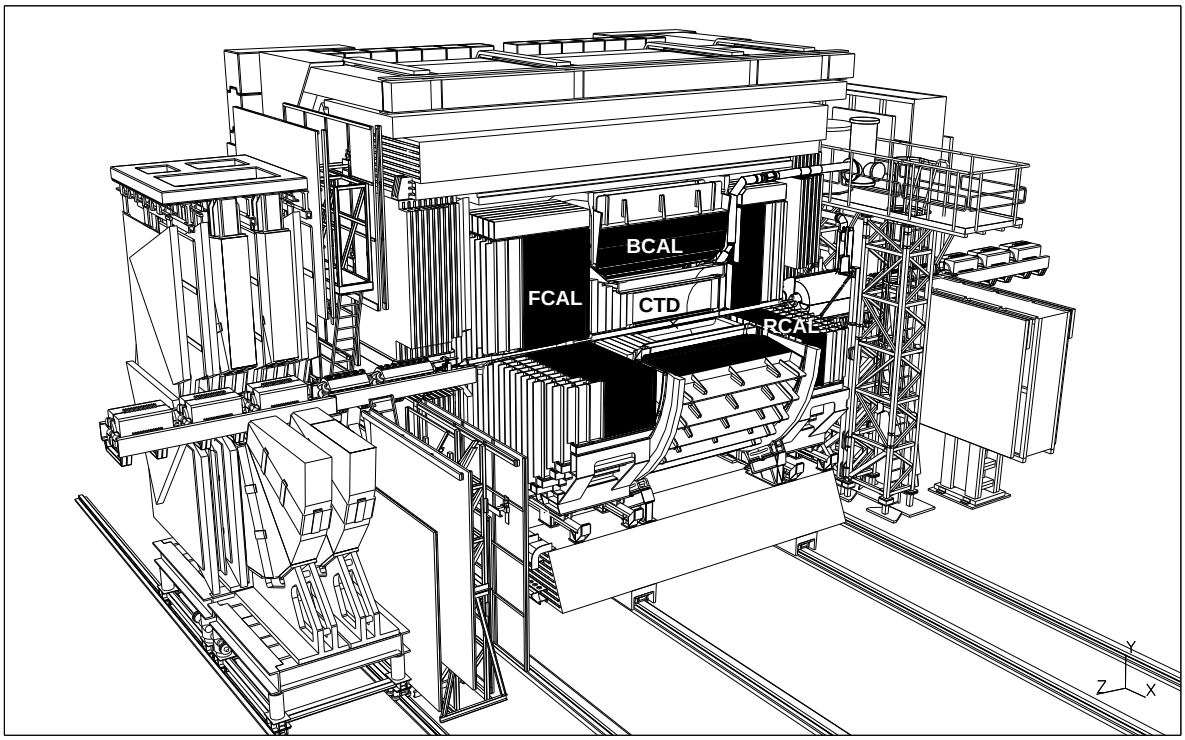

Figure 3.2: *The ZEUS detector. The main components are discussed in the text.*

Due to the different momenta of the colliding electrons and protons, the centre-of-mass of the ep system is boosted in the forward[4] direction with $\beta = 0.94$. The detector features a distinct forward-backward asymmetry and is thereby suited to this special kinematic situation with higher particle flows and energy deposits in the forward direction. Except for the two beampipe holes at the forward and rear ends, the interaction region is enclosed hermetically by the different shells of detector components, as depicted in Fig. 3.2

The innermost part of ZEUS is the central tracking detector (CTD). The CTD is a cylindrical drift chamber operating in a longitudinal magnetic field of 1.43 T which is provided by a superconducting solenoid. The tracking system is completed by planar drift chambers in the forward and rear directions (FTD 1,2,3 and RTD).

The tracking detectors and the solenoid are enclosed by the high-resolution uranium-scintillator calorimeter (CAL) which consists of three parts: the forward (FCAL), the barrel (BCAL) and the rear (RCAL) calorimeters.

[4] The ZEUS coordinate system is a right-handed Cartesian system, with the Z axis pointing in the proton-beam direction, referred to as the "forward" direction, and the X axis pointing left towards the centre of HERA. The coordinate origin is at the nominal interaction point. The pseudorapidity is defined as $\eta = -\ln(\tan\frac{\theta}{2})$, where the polar angle, θ, is measured with respect to the proton-beam direction. The azimuthal angle is denoted by ϕ.

The outermost shell of the central detector is represented by the backing calorimeter (BAC), which is the instrumented return yoke of the solenoid, and by a system of muon chambers (F/B/RMUON).

The luminosity is measured using the Bethe-Heitler reaction $ep \to ep\gamma$. The rate and energies of the resulting small-angle energetic photons are measured by the luminosity monitor (LUMI-γ), a lead-scintillator calorimeter placed in the HERA tunnel at $Z = -107\,\mathrm{m}$.

Detailed descriptions of all detector components can be found in [76], including a series of subdetectors not mentioned here. The components most relevant to this analysis are discussed in the following sections.

3.2.2 The central tracking detector

The CTD [77–79] represents the core of the ZEUS tracking system. It is a cylindrical drift chamber with inner and outer radii of 18.2 cm and 79.4 cm, respectively. Its active volume extends between $Z = -100\,\mathrm{cm}$ and $Z = 105\,\mathrm{cm}$ and covers the polar-angle region $15° < \theta < 164°$.

A total of 4608 sense wires and 19584 field wires are arranged in nine concentric superlayers. The wires are segmented into octants, one of which is shown in Fig. 3.3. The spatial resolution of the CTD in the transverse plane is about 190 µm. The CTD is operated in a solenoidal magnetic field of 1.43 T, so that from the track curvature the transverse momenta of charged particles can be determined. The transverse-momentum resolution for full-length tracks is parameterised as

$$\frac{\sigma(p_T)}{p_T} = 0.0058\,p_T[\,\mathrm{GeV}] \oplus 0.0065 \oplus \frac{0.0014}{p_T[\,\mathrm{GeV}]}\,, \tag{3.1}$$

where the symbol $\oplus$ denotes addition in quadrature.

In the superlayers 2, 4, 6 and 8, the sense wires are not parallel to the Z-axis but tilted by stereo angles of about $\pm 5°$. The Z-coordinates of track points are thereby measured with an accuracy of 1–1.5 mm. In addition, the superlayers 1, 3 and 5 are equipped with a Z-by-timing system, which allows for a second, independent Z measurement with a resolution of approximately 4.5 cm.

The reconstructed tracks are used in a fitting procedure to determine the primary event-vertex. The resolution obtained is 0.1 cm in the transverse plane and 0.4 cm in Z-direction.

3.2.3 The uranium calorimeter

The ZEUS CAL [80–84] is a high-resolution sandwich sampling-calorimeter, consisting of alternating layers of depleted uranium as absorber and plastic scintillator as active

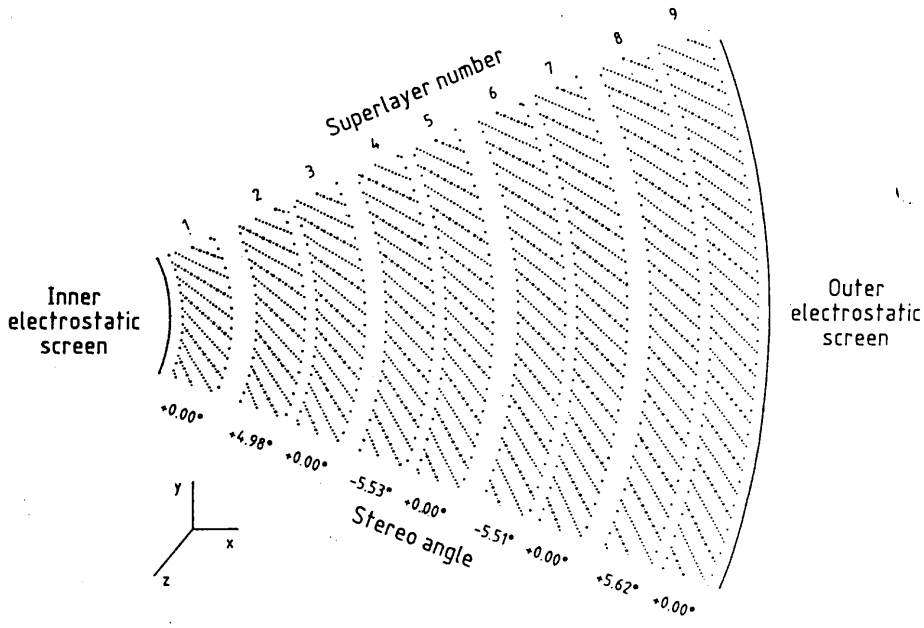

Figure 3.3: *Cross-section view of one octant of the CTD. Shown are the nine superlayers each of which contains eight layers of sense wires. The heavier dots indicate sense wires, while the lighter dots represent field wires.*

material. The thicknesses of the uranium (3.3 mm) and scintillator (2.6 mm) layers were chosen as to achieve compensation, i.e. equal response to both hadronic and electromagnetic particles, and thus optimum hadronic energy resolution.

The CAL is divided into three parts (Fig. 3.4), covering the polar-angle regions 2.2°–39.9° (FCAL), 36.7°–129.1° (BCAL) and 128.1°–178.4° (RCAL). Each of these three subcalorimeters consists of modules, which are subdivided in depth into an electromagnetic (EMC) section and two (RCAL: one) hadronic (HAC) sections. Each of the HAC sections consists of a single cell. The transverse segmentation of the EMC sections is finer, with each section consisting of four (RCAL: two) cells

The cells, of which there are 5918 altogether, are the smallest readout units of the CAL, each being read out at opposite sites by two photomultiplier (PM) tubes via wavelength-shifting light guides. This provides measurement redundancy, rendering the cell information available even if one of the two PMs fails. In addition, the twofold readout provides transverse position-information via signal-sharing.

The energy resolution, $\sigma(E)/E$, was determined by test-beam measurements, yielding $0.18/\sqrt{E[\,\mathrm{GeV}]} \oplus 1\,\%$ for electromagnetic showers and $0.35/\sqrt{E[\,\mathrm{GeV}]} \oplus 2\,\%$ for hadronic showers. The natural radioactivity of the depleted uranium provides a stable reference signal which is used to monitor and calibrate the absolute energy scale.

The segmentation into cells allows for a precise measurement of the spatial positions of energy deposits, which is particularly important in cases where the trajectory of the final-

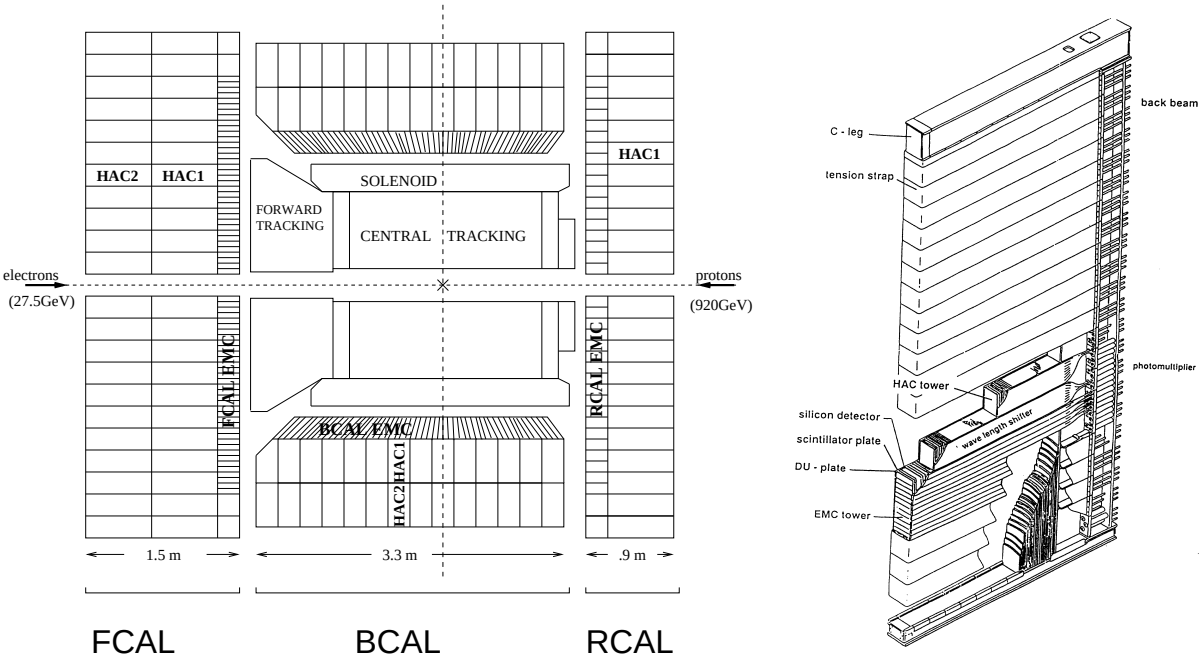

Figure 3.4: *Left: The ZEUS calorimeter (YZ projection). Right: An FCAL module, being subdivided into uranium-scintillator stacks (named towers).*

state electron happens to fall outside the angular acceptance of the tracking detectors. The CAL is hermetic except for the two beampipe holes of $20 \times 20\,\mathrm{cm}^2$ (FCAL) and $20 \times 8\,\mathrm{cm}^2$ (RCAL), respectively. The arrival time of CAL energy deposits is measured with sub-nanosecond resolution for energy deposits above 4.5 GeV, allowing the rejection of non-ep background.

3.2.4 Luminosity measurement

To determine the integrated luminosity provided by HERA, the rate of hard bremsstrahlung photons from the Bethe-Heitler process $ep \to ep\gamma$ [85] is measured. The cross section of this reference process is high and is known theoretically to an accuracy of less than 0.5 %.

The final-state photons emerge under polar angles of less than 0.5 mrad with respect to the beam axis. Undisturbed by the HERA bending magnets they leave the beampipe through a thin exit window, to be detected by a lead-scintillator sampling calorimeter (LUMI-γ) at $Z = -107\,\mathrm{m}$ [86–88]. A carbon/lead filter installed in front of the calorimeter provides shielding against synchrotron radiation.

The Bethe-Heitler rates are sufficiently high to render the statistical errors of the measurement negligibly small. The total systematic uncertainty of the luminosity measurement is 1.8 % (2.25 %) for the data taken during the 98/99 e^-p (99/00 e^+p) running.

3.3 The trigger and data-acquisition system

At the HERA design luminosity of $1.6 \cdot 10^{31}\,\mathrm{cm}^{-2}\,\mathrm{s}^{-1}$, the rate of *ep* reactions detectable by ZEUS is a few ten Hz or even considerably less, depending on the types of reactions. These numbers are to be contrasted with the background rate, which, depending on the beam conditions and the residual pressure in the beampipe, is higher by about a factor of 10^3. The dominant contribution comes from upstream interactions of the proton beam with residual gas molecules (beam-gas reactions). Further sources of background are the scattering of beam particles off the beampipe (beam-wall reactions), synchrotron radiation emitted by the electron beam in the bending magnets, as well as muons from the beam halo and cosmic muons.

Fishing the actual *ep* reactions out of the overwhelming amount of background is a demanding task. To accomplish it ZEUS employs a sophisticated pipelined trigger-system which features increasingly selective filtering on three successive levels.

The first-level trigger (FLT) is hardware-based. The global FLT decision combining the trigger signals from the individual FLT electronics of the different components is provided 4.4 μs (i.e. 46 bunch crossings) after the original event occured. Taken into account are calorimeter data, CTD data and signals recorded in the muon detectors. The FLT output rate is supposed to be less than 1 kHz.

The events thus accepted are handed to the transputer-based second-level trigger (SLT) which, compared to the FLT, employs a higher level of precision and a larger number of variables. Thereby a further reduction of the event rate by about a factor of ten is achieved.

If accepted by the SLT, the events are then transferred to the event builder (EVB), an array of transputers the task of which is to combine and format the data before sending them to the third-level trigger (TLT).

The TLT is software based, running part of the offline reconstruction code on a workstation farm. It is the only of the three trigger levels having access to the complete information from all components. The events finally accepted are written to disk at a rate of 5–10 Hz. It takes about 0.3 sec for all three trigger levels to analyse one event. The bunch-crossing rate is as high as 10.4 MHz. Yet due to the pipelining used the trigger system is capable of analysing every bunch crossing.

Before the data are made available for offline analysis, the stored events are fully reconstructed by a PC farm. During reconstruction, various so-called DST (data summary tape) bits are assigned to events that fulfil different sets of preselection cuts. This marking by DST bits allows to quickly access a given type of event for offline analysis.

Chapter 4

Kinematics and event reconstruction

4.1 Deep inelastic scattering

The domain of HERA is deep inelastic *ep* scattering (DIS) [89–96], which, in leading order, proceeds via t-channel exchange of a gauge boson between the incoming electron and a quark out of the proton. Two classes are to be distinguished: neutral current (NC) and charged current (CC) reactions. The former proceed via γ/Z exchange, so that the final state contains the scattered electron; the latter require the exchange of a W boson, leading to a neutrino in the final state (Fig. 4.1). With the neutrino escaping unobserved from the detector, a net amount of total transverse momentum measured is characteristic of CC reactions.

In addition to the scattered lepton, the final state of DIS reactions contains a hadronic system. In lowest order, two hadronic jets emerge. The remnant jet goes in the proton direction, typically leaving energy deposits in the first inner ring of the FCAL. The current jet indicates the direction of the struck quark. In higher orders, the QCD interactions

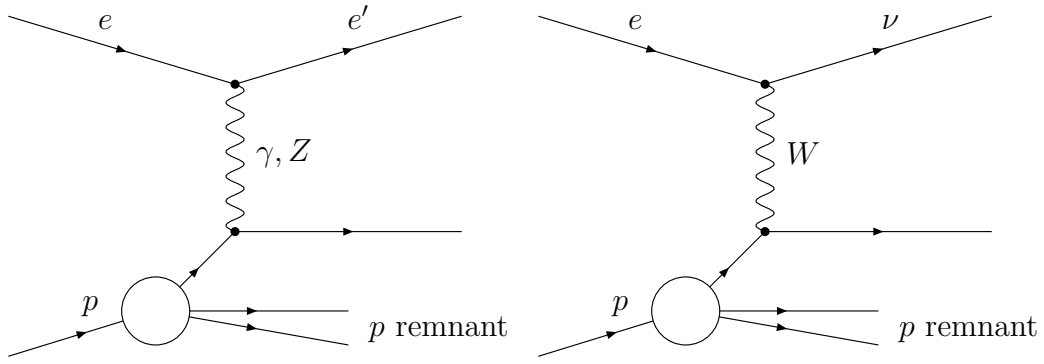

Figure 4.1: *Leading-order Feynman diagrams for neutral (left) and charged current (right) DIS reactions.*

between the struck quark and the proton remnant can give rise to events with more than two jets.

The four-momenta and energies of the particles involved in the scattering are denoted as follows (lab system):

	four-mom.	energy
incoming electron	k	E_e
scattered lepton	k'	E'_e
incoming proton	P	E_p
exchanged gauge boson	q	

The square of the centre-of-mass energy is given by $s = (k + P)^2$; neglecting the particle masses yields $s = 4E_eE_p$.

To describe the kinematics of DIS reactions it is conventional to use the following Lorentz-invariant variables:

$$\begin{aligned} Q^2 &= -q^2 = -(k - k')^2 \ , \\ x &= \frac{Q^2}{2Pq} \ , \\ y &= \frac{Pq}{Pk} \ . \end{aligned}$$

The negative square of the four-momentum transfer, Q^2, describes the virtuality of the gauge boson exchanged. In the quark parton model (QPM) the proton is regarded as a collection of massless quarks with zero transverse momentum, off which the virtual photon is scattered elastically. In this picture, the Bjorken scaling variable, x, can be interpreted as the fraction of the proton momentum carried by the struck quark. Consequently, $0 < x < 1$. The second scaling variable, y, is related to the scattering angle, θ^*, in the electron-quark centre-of-mass system by: $y = 1/2(1 - \cos\theta^*)$, with $\theta^* = 0$ corresponding to no deflection. The value of y is a measure for the inelasticity of the event, with a possible range of $0 < y < 1$ and high values characterising the deep-inelastic regime. The above-mentioned variables are related via $Q^2 = sxy$.

As described in Sect. 5.2.1, neutral and charged current DIS constitute considerable sources of background for the excited-lepton decays being searched for. Two further Standard Model processes have been taken into account as potential backgrounds and are thus to be mentioned here: photoproduction and QED-Compton events.

The majority of HERA events stems from photoproduction reactions, which are characterised by the exchange of a real or quasi-real photon, i.e. $Q^2 \approx 0\,\mathrm{GeV}^2$. In such events, the scattered electron is not contained in the central detector but disappears through the rear beampipe. Yet isolated hadrons or photons from π^0 decays may be misidentified as electrons.

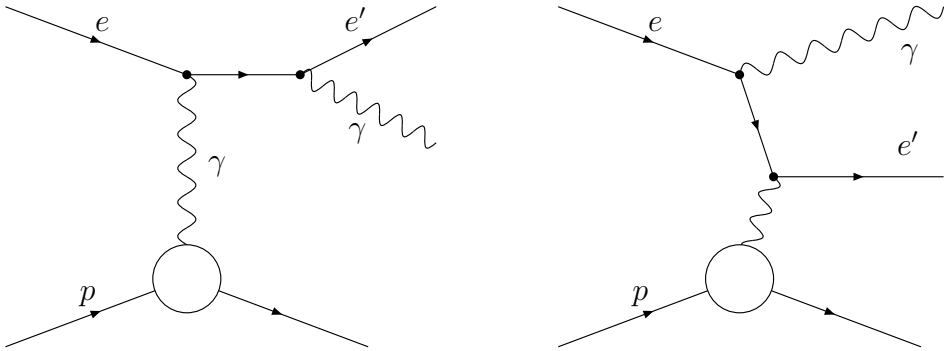

Figure 4.2: *Leading-order Feynman diagrams for elastic QED-Compton reactions. This process may as well occur inelastically.*

A distinction is made between direct and resolved photoproduction. In the former case, the exchanged photon interacts directly with a parton, whereas in the latter case, the photon exhibits a dynamic structure of quarks and gluons itself, where one of them interacts with a parton out of the proton.

QED-Compton events, which are sometimes referred to as wide-angle bremsstrahlung, feature an electron plus a photon in the final state. The corresponding leading-order Feynman diagrams are shown in Fig. 4.2. With the electron and photon emerging with considerable transverse momenta, QED-Compton events constitute an important background process in the $e^* \to e\gamma$ search.

4.2 Reconstruction of kinematic quantities

4.2.1 Energy corrections

Prior to the reconstruction of event variables, the measured CAL data are subjected to a number of correction routines [97, 98]:

- noise suppression:
  the natural radioactivity of the depleted uranium leads to a constant level of noise in the CAL cells. This noise is suppressed by a cut on the minimum energy of 60 (110) MeV for all EMC (HAC) cells;
- energy scale:
  based on detailed studies of energy measurements and simulated detector responses in the different parts of the CAL, algorithms are available to correct the absolute energy scale. The remaining uncertainty in the energy scale lies between 1 % and 3 %, depending on the sort of particle (electrons or hadrons) and on the subcalorimeter considered (F/B/RCAL);

- dead material:
  energy losses in the inactive material between the interaction point and the calorimeter are corrected for by using dead-material maps which contain detailed descriptions of the detector layout for the different periods of ZEUS operation;
- non-uniformity:
  the CAL response is degraded by energy losses in the boundaries between cells and modules. These non-uniformity effects are corrected for separately in data and MC;
- alignment:
  for different data-taking periods, the relative and absolute positions of the calorimeter parts can exhibit slight changes. Such alignment effects are taken into account.

4.2.2 Global event-variables

Event variables are denoted as global in case they are derived in the same manner for every event, regardless of the outcome of the electron finding. The CAL-related global quantities used in this analysis are listed below:

- the total energy deposited in the calorimeter:

$$E_{\text{tot}} = \sum_i E_i \ , \tag{4.1}$$

  where the summation index, i, runs over all calorimeter cells;
- the momentum vector of the total energy deposited in the CAL:

$$\begin{aligned} p_X^{\text{tot}} &= \sum_i E_i \sin\theta_i \cos\phi_i \ , \\ p_Y^{\text{tot}} &= \sum_i E_i \sin\theta_i \sin\phi_i \ , \\ p_Z^{\text{tot}} &= \sum_i E_i \cos\theta_i \ , \end{aligned} \tag{4.2}$$

  where the angles associated to the geometric cell-centres are calculated with regard to the event vertex;
- the scalar sum of the transverse energy deposited in the CAL:

$$E_T^{\text{tot}} = \sum_i E_i \sin\theta_i \ ; \tag{4.3}$$

- the magnitude of the vector sum of the transverse energy, which is also referred to as missing transverse momentum:

$$\not{P}_T = \sqrt{(p_X^{\text{tot}})^2 + (p_Y^{\text{tot}})^2} \ ; \tag{4.4}$$

- the total invariant mass:

$$M_{\text{tot}} = \sqrt{(E_{\text{tot}})^2 - (p_X^{\text{tot}})^2 - (p_Y^{\text{tot}})^2 - (p_Z^{\text{tot}})^2} \ . \tag{4.5}$$

  As an additional variable, the ratio of the reconstructed e^* or ν^* mass (Sect. 4.3) and the total invariant mass is employed, being denoted by $M_{\text{tot}}/M_{\text{rec}}$;

- the difference between the total energy and the longitudinal momentum deposited in the CAL:

$$\delta = \sum_i E_i(1 - \cos\theta_i) \ , \tag{4.6}$$

  which is a measure of the longitudinal energy and momentum conservation. For events with all final-state particles being contained in the detector, e.g. clean NC events, the nominal value of δ should equal twice the electron-beam energy ($2E_e = 55\,\text{GeV}$). If, however, a final-state particle escapes undetected in the rear direction, as is the case with the scattered electron in PHP reactions, the value of δ is decreased by approximately twice the particle's energy. If, on the other hand, some energy is lost from detection into the forward region, e.g. part of the proton remnant, this does not change the measured value of δ.

Energy deposits from the proton remnant are typically confined to the first inner ring of the FCAL. In order to avoid a contribution from the remnant, the above-mentioned quantities E_{tot}, $p_{X,Y,Z}^{\text{tot}}$, E_T^{tot}, $\not{P}_T$ and M_{tot} are calculated not actually from all CAL cells, but excluding those belonging to the FCAL first inner ring.

In addition to the CAL-related quantities, the following tracking-related variable is used for some of the decay channels:

- the ratio of the number of tracks used for fitting the primary event-vertex and the number of all CTD tracks, $\#_{\text{trk}}^{\text{vtx}}/\#_{\text{trk}}^{\text{tot}}$.

4.2.3 Electron finding

An electron finder is used in all analysed excited-lepton channels to identify electromagnetic clusters in the final states. Some of the channels ($\nu^* \to \nu\gamma$, $\nu^* \to eq\bar{q}'$, $e^* \to e\gamma$, $e^* \to eq\bar{q}$) feature an electron or photon in the final state, whereas the others ($\nu^* \to \nu q\bar{q}$, $e^* \to \nu q\bar{q}'$) are characterised by the explicit absence of electromagnetic clusters. Thus the identification of electron or photon candidates serves as an important criterion for either selecting or vetoing events, depending on the decay channel considered.

The electron finder employed for this analysis is one of two such routines which are commonly used for physics analyses within ZEUS. A description of this routine, EM, can be found in [99, 100]. The EM electron finder is based on a detailed parameterisation of

the detector response for electrons. Seven variables are used to distinguish between electromagnetic and hadronic clusters; four of them are calorimeter variables, the remaining three are related to tracking information. For candidates which are outside of the tracking acceptance (Sect. 3.2.2) or which do not have a matching track, only the CAL variables are used. Thus, EM can also be employed to identify photons.[1]

From the distributions of these variables in selected data events with clean NC DIS signatures, probability distributions were derived and parameterised. On the basis of these parameterisations, a total probability is calculated by EM from the corresponding quantities measured by the detector for any calorimeter cluster under consideration.

The electron-finder probability thus derived is used as a cut variable to select electron or photon candidates, as described in Sect. 5.4.2. In addition, the following electron-related detector variables are employed in this analysis, either for selection purposes or for reconstructing excited-lepton masses:

- the energy, E_{el}, and the polar and azimuthal angles, θ_{el} and ϕ_{el}, of the electromagnetic cluster. For the calculation of the angles, the event vertex is taken into account. From these quantities the momentum vector and the transverse energy of the cluster are derived:

$$p_X^{el} = E_{el} \sin\theta_{el} \cos\phi_{el} \ , \tag{4.7}$$
$$p_Y^{el} = E_{el} \sin\theta_{el} \sin\phi_{el} \ , \tag{4.8}$$
$$p_X^{el} = E_{el} \cos\theta_{el} \ , \tag{4.9}$$
$$E_T^{el} = E_{el} \sin\theta_{el} \ ; \tag{4.10}$$

- the isolated energy, $E_{\rm iso}$, which is the sum of the CAL energy not associated to the electromagnetic cluster but within an η-ϕ cone of radius 0.8 centered on the cluster;
- the distance of closest approach, DCA, between the electromagnetic cluster and an attributed CTD track. To calculate DCA, the track is extrapolated into the CAL;
- the momentum of a matching track, $p_{\rm trk}$, which is inferred from the track curvature.

In cases where more than one electron candidate per event has been identified by the electron finder, a decision is taken in favour of the candidate that has been assigned the highest probability.

For decay channels featuring a final-state electron or photon, the calorimeter quantities of the hadronic final state – namely $E_{\rm had}$, $p_{X,Y,Z}^{\rm had}$, $E_T^{\rm had}$ and $M_{\rm had}$ – are calculated according to (4.1)–(4.5), but excluding those CAL cells belonging to the electromagnetic cluster (for $e^* \to e\gamma$, this holds for both clusters).

[1] Matching tracks are the only criterion to classify electromagnetic clusters in the ZEUS detector as originating from electrons.

In case of the channels $e^* \to \nu q\bar{q}'$ and $\nu^* \to \nu q\bar{q}$, the hadronic quantities are identical to the respective "total" quantities. For in the absence of an electromagnetic cluster the final state is entirely hadronic.

The ratio $M_{\mathrm{had}}/E_T^{\mathrm{had}}$ is employed as an additional variable.

The second electron finder available, SINISTRA 95, employs a neural network to identify electromagnetic clusters [101, 102]. In contrast to EM, only calorimeter information is used. This is related to the fact that SINISTRA 95 was optimised for low-Q^2 events where the electron is scattered in the rear direction and is likely to be outside of the CTD acceptance. Therefore SINISTRA 95 is less suited for electron finding in excited-lepton decays, many of which are characterised by a forward-going electron or photon. Yet in this analysis SINISTRA 95 is used as a systematic check, as will be described in Sect. 6.4.

4.3 Mass reconstruction of excited leptons

The general approach for the reconstruction of the invariant mass, M_{FV}, of the lepton-boson system emerging from an excited-lepton decay is given by

$$\begin{aligned} M_{FV}^2 &= (p_F + p_V)^2 && (4.11)\\ &= m_F^2 + m_V^2 + 2p_F p_V && (4.12)\\ &= m_V^2 + 2(E_F E_V - \vec{p}_F \cdot \vec{p}_V) \ , && (4.13) \end{aligned}$$

where the four-momenta of the final-state lepton and boson are denoted by p_F and p_V, respectively, and the masses, energies and momentum vectors are denoted by $m_{F,V}$, $E_{F,V}$ and $\vec{p}_{F,V}$; in (4.13) the lepton mass has been neglected.

To improve the mass resolution, it is convenient to apply the following kinematic constraints:

- in all decays involving a final-state W or Z, the excited electron or neutrino is assumed to be produced with negligible transverse momentum.
  Furthermore, in these channels the invariant mass of the W or Z decay products is assumed to equal the mass of the respective boson;
- except for $e^* \to e\gamma$, the longitudinal energy-momentum variable, δ, is constrained to its nominal value in case of detecting all final-state particles, i.e. twice the electron-beam energy.

Using these constraints, the mass formulae for the different channels turn out as follows:

- $\underline{\nu^* \to \nu\gamma}$:
  the $\nu\gamma$ invariant mass is obtained from

$$M_{\nu\gamma}^2 = 2(E_\nu E_\gamma - p_X^\nu p_X^\gamma - p_Y^\nu p_Y^\gamma - p_Z^\nu p_Z^\gamma) \ , \qquad (4.14)$$

where the energy, E_γ, and the momentum components, $p^\gamma_{X,Y,Z}$, of the photon are directly provided by measurement. The transverse components of the neutrino momentum are obtained from the $\not{P}_T$ vector; the longitudinal neutrino-momentum, p^ν_Z, is calculated using the measured value of δ ($2E_e = 55\,\text{GeV}$ being twice the electron-beam energy):

$$p^\nu_Z = \frac{(\not{P}_T)^2 - (2E_e - \delta)^2}{2(2E_e - \delta)} \; ; \tag{4.15}$$

- $e^* \to e\gamma$:
  for the $e\gamma$ final state, (4.13) reduces to

$$M^2_{e\gamma} = 2(E_{el}E_\gamma - p^{el}_X p^\gamma_X - p^{el}_Y p^\gamma_Y - p^{el}_Z p^\gamma_Z) \; , \tag{4.16}$$

  where the energies and the momentum components of the electron and the photon are provided by measurement;

- $\nu^* \to eW \to eq\bar{q}'$ and $e^* \to eZ \to eq\bar{q}$:
  in the following formulae, the subscript V stands for either W or Z, depending on the channel considered. For the eW or eZ final state, (4.13) together with the above-mentioned constraint on the excited-lepton transverse momentum gives

$$M^2_{eV} = m^2_V + 2(E_{el}E_V + (E^{el}_T)^2 - p^{el}_Z p^V_Z) \; , \tag{4.17}$$

  where $(E^{el}_T)^2 = (p^{el}_X)^2 + (p^{el}_Y)^2$ denotes the transverse momentum squared of the final-state electron. The energy, E_V, and the longitudinal momentum, p^V_Z, of the respective boson are obtained from

$$E_V = \frac{(2E_e - E_{el} + p^{el}_Z)^2 + m^2_V + (E^{el}_T)^2}{2(2E_e - E_{el} + p^{el}_Z)} \; , \tag{4.18}$$

$$p^V_Z = E_V - (2E_e - E_{el} + p^{el}_Z) \; ; \tag{4.19}$$

- $\nu^* \to \nu Z \to \nu q\bar{q}$ and $e^* \to \nu W \to \nu q\bar{q}'$:
  for the νZ and νW final states, the formulae derived for eZ and eW are applicable as well, the only difference being that the electron variables are replaced by the respective neutrino variables. The latter are obtained from the missing transverse momentum, $\not{P}_T$, and from the measured value of δ.

The mass resolutions obtained for the different e^* and ν^* channels are stated in Sects. 5.6.2 to 5.6.7. The corresponding graphical representations, as well as examples of the reconstructed-mass distributions are shown in Sect. 5.6.8.

Chapter 5

Search for excited leptons

5.1 Ingredients and strategy

The search for excited leptons presented in this chapter is based on three essential ingredients: the experimental data, the simulated signal events and the background simulation.

To search for some hypothetical phenomenon means to pose a question to nature concerning the existence of a hitherto undiscovered entity. The answer is then found on observational grounds, i.e. the experimental data constitute the empirical basis of the analysis.

To formulate this question requires some notion of the specific properties of the searched entity; in other words, one needs to have a clear image of what is actually to be sought. For that purpose, MC simulations of excited-lepton production and decays are employed,[1] allowing to develop and test selection criteria.

The observational answer found by applying these selection criteria is not as unambiguous as the question preceding it. For it must be interpreted within the framework of theoretical presuppositions: well-known particle reactions may yield the same experimental signature as the phenomena that are searched for. To quantify the backgrounds, MC simulations of the respective Standard Model processes are employed.[2]

Being equipped with these ingredients, the following strategy has been chosen to perform the search. In spite of the efficient ZEUS trigger system, the raw experimental data contain not only *ep* reactions but still considerable amounts of background due to non-*ep* reactions, e.g. beam-gas interactions and muon events. The overlay of both types of events is observed as well, e.g. regular *ep* events with additional CTD tracks emerging from beam-gas scattering upstream of the interaction region. Indeed, non-*ep* backgrounds are not part of the Monte Carlo simulation.

[1] In the following, the samples of simulated e^* and ν^* events are also referred to as "signal MC".
[2] These Monte Carlo samples are also referred to as "background MC".

A preselection is applied the aim of which is twofold: firstly, to minimise the data samples' being contaminated by non-ep background; secondly, to restrict the samples that are used for further analysis to events with potentially interesting final states (Sect. 5.4). These goals are achieved by requiring a conjunction of DST bits and by applying a number of cleaning algorithms. Furthermore, a set of cuts specific to each excited-lepton channel is applied to demonstrate that the data surviving these cuts are well described by the background simulation; these preselection cuts are similar to the final event-selection criteria but less restrictive. All kinds of samples considered are subjected to the same preselection – experimental data as well as background MC and signal MC.

Finally, the real and simulated events thus preselected are subjected to two different procedures of event selection (Sect. 5.5): the first employs fixed cuts which are basically more restrictive and refined variants of the channel-wise cuts applied for the preselection; in contrast to that, the second method is based on probabilities, following a more sophisticated approach in optimising its selection criteria than the first method. In spite of sharing the same preselection basis, the two methods are actually to be regarded as alternatives, offering the possibility of cross checking.

Both selection approaches yield pairs of candidate events and expected background events for the six decay channels studied (Sect. 5.6). Furthermore, selection efficiencies and mass resolutions are obtained with the help of the signal MC samples.

The resulting mass spectra undergo a statistical analysis, testing whether any evidence for a heavy excited lepton is observed. As no such evidence has been found, the search results obtained (mass spectra and efficiencies) are used to derive upper limits on e^* and ν^* production, as described in Sect. 6.1.

5.2 Monte Carlo simulations

Monte Carlo simulations with a high degree of verisimilitude are indispensable to the analysis of the particle reactions recorded by a complex detector system like ZEUS. Great collaborative effort has thus been invested into the development of elaborated event generators as well as of detailed detector simulations.

To start with, final states of a given type of ep reaction are to be provided by an event generator. The output of such a program comprises a list of the final-state particles together with their four-momenta. For the simulation of inelastic reactions, there exist different phenomenological approaches to model the development of the hadronic final state.

The final states thus generated are then used as input to the detector simulation. The passage of the final-state particles and of possible decay products and secondary particles are traced through the detector, simulating their interactions with the detector materials

and the resulting response of the active components. For this purpose, a tailor-made version of the simulation package GEANT 3.13 [103] containing a detailed virtual image of the ZEUS detector is available. In the simulation of the detector hardware and of the physics processes taking place, certain approximations are inevitable, e.g. small geometric structures not being reproduced in detail or shower developments being truncated.

Finally, the trigger decision is simulated, and the Monte Carlo data are subjected to the same offline event reconstruction as used for the experimental data.

5.2.1 Background processes

To determine the backgrounds arising from well-known types of ep reactions, samples of NC and CC DIS as well as photoproduction and QED-Compton scattering have been generated.[3] Aiming at negligible statistical errors for these background samples, the numbers of events generated should correspond to an integrated luminosity that is a multiple of the experimental-data luminosity. Furthermore, in case of NC and CC DIS, samples have been generated with lower cuts on increasingly large values of Q^2, thereby accounting for the fact that the respective differential cross sections fall off steeply with growing Q^2.

In the following, the MC samples generated for the different background processes are tabularised. Given the number of events, #, and the cross section, σ, the integrated luminosity represented by an individual sample, $\mathcal{L}_{MC}$, follows from $\mathcal{L}_{MC} = \#/\sigma$. Taking the ratio of the luminosities of the data, $\mathcal{L}$, and of a given MC sample, $\mathcal{L}_{MC}$, provides the weight factor with which each event of the sample is to be multiplied. In case of the DIS samples, the weight factors are calculated based on the actual Q^2 value (MC true information) of a given event, taking into account the overlapping in Q^2 of the different samples.

NC and CC DIS:
Neutral and charged current DIS events have been generated using DJANGOH 1.1 [104, 105] together with the CTEQ5D [106] parameterisations of the parton distribution functions (PDFs). To simulate the hadronic final state, the matrix-element and parton-shower (MEPS) model of LEPTO 6.5.1 [107] has been used for the QCD cascade, followed by JETSET 7.4 [108–110] for the hadronisation. In addition, to estimate systematic uncertainties due to the choice of the hadronisation model, the colour-dipole model implemented in ARIADNE [111] has been used as an alternative to MEPS.
With both the NC and CC cross sections depending on the charge sign of the incoming lepton, distinct samples are to be employed for e^-p and e^+p running. Listed below are the DIS samples matching the different periods of ZEUS operation, generated with the alternative approaches of MEPS and ARIADNE, respectively. The 98/99 samples of both models contain identical numbers of events.

[3] The same sort of samples are used in dedicated analyses of the respective processes, e.g. NC/CC DIS, but are then regarded as "signal" rather than as "background" MC.

1998/1999 e^-p, MEPS or ARIADNE		
NC DIS	events	σ[pb]
$Q^2 > 100\,\mathrm{GeV}^2$	380000	8157.9
$Q^2 > 400\,\mathrm{GeV}^2$	60000	1196.1
$Q^2 > 1250\,\mathrm{GeV}^2$	25000	216.98
$Q^2 > 2500\,\mathrm{GeV}^2$	12000	71.77
$Q^2 > 5000\,\mathrm{GeV}^2$	12000	21.654
$Q^2 > 10000\,\mathrm{GeV}^2$	12000	5.3628
$Q^2 > 20000\,\mathrm{GeV}^2$	12000	0.84728
$Q^2 > 30000\,\mathrm{GeV}^2$	6000	0.18532
$Q^2 > 40000\,\mathrm{GeV}^2$	6000	0.042649
$Q^2 > 50000\,\mathrm{GeV}^2$	6000	0.0091897

1998/1999 e^-p, MEPS or ARIADNE		
CC DIS	events	σ[pb]
$Q^2 > 10\,\mathrm{GeV}^2$	25000	78.943
$Q^2 > 100\,\mathrm{GeV}^2$	25000	72.778
$Q^2 > 5000\,\mathrm{GeV}^2$	15000	14.445
$Q^2 > 10000\,\mathrm{GeV}^2$	10000	5.3854
$Q^2 > 20000\,\mathrm{GeV}^2$	10000	1.1339

1999/2000 e^+p			
NC DIS	MEPS evts.	ARIADNE evts.	σ[pb]
$Q^2 > 100\,\mathrm{GeV}^2$	680000	940000	8122
$Q^2 > 400\,\mathrm{GeV}^2$	60000	120000	1167.7
$Q^2 > 1250\,\mathrm{GeV}^2$	25000	50000	197.54
$Q^2 > 2500\,\mathrm{GeV}^2$	12000	24000	58.915
$Q^2 > 5000\,\mathrm{GeV}^2$	12000	24000	14.846
$Q^2 > 10000\,\mathrm{GeV}^2$	12000	24000	2.7936
$Q^2 > 20000\,\mathrm{GeV}^2$	12000	24000	0.30999
$Q^2 > 30000\,\mathrm{GeV}^2$	6000	12000	0.054443
$Q^2 > 40000\,\mathrm{GeV}^2$	6000	12000	0.010874
$Q^2 > 50000\,\mathrm{GeV}^2$	6000	12000	0.0021185

1998/2000 e^+p			
CC DIS	MEPS evts.	ARIADNE evts.	σ[pb]
$Q^2 > 10\,\mathrm{GeV}^2$	25000	25000	45.2021
$Q^2 > 100\,\mathrm{GeV}^2$	25000	25000	39.7737
$Q^2 > 5000\,\mathrm{GeV}^2$	15000	15000	3.1998
$Q^2 > 10000\,\mathrm{GeV}^2$	10000	5000	0.6828
$Q^2 > 20000\,\mathrm{GeV}^2$	10000	5000	0.0619

Photoproduction:
Direct and resolved photoproduction (PHP) backgrounds have been simulated with the HERWIG 5.9 [112] generator using CTEQ4D [113] for the PDFs and GRV-G (LO) [114] for the photon structure function. The PHP samples listed below contain e^-p events but are appropriate to be used for both the 98/99 e^-p and the 99/00 e^+p data. They have been produced with generator-level cuts of $> 20\,\text{GeV}$ on the total transverse energy and of $> 6\,\text{GeV}$ on the individual transverse momenta of the generated hadrons.

PHP, HERWIG	events	$\sigma[\,\text{pb}]$
direct	380000	15623.8
resolved	1650000	82411.4

QED-Compton scattering:
Elastic and quasi-elastic QED-Compton scattering events have been generated with COMPTON 2.0 [115]. The samples contain e^-p events but are suited to be used for the e^+p data as well. As listed below, there exist samples with different ranges of the invariant mass of the $e\gamma$ system. To avoid an overlap with inelastic QED-Compton scattering being part of the DJANGOH simulation, a cut of $M_{\text{had}} < 5.0\,\text{GeV}$ has been applied to the samples listed below.

QED-Compton	events	$\sigma[\,\text{pb}]$
$M_{e\gamma} \in (20, 50)\,\text{GeV}$	20000	34.664
$M_{e\gamma} \in (50, 100)\,\text{GeV}$	10000	3.777
$M_{e\gamma} > 100\,\text{GeV}$	10000	0.391

5.2.2 Excited-lepton signals

Monte Carlo samples of excited-electron and -neutrino production with subsequent decays into the six final states considered have been generated. For each of the six decay channels, ten different samples have been produced, representing excited-lepton masses of 100 GeV[4] to 300 GeV (in steps of 25 GeV) and of 310 GeV. Each sample contains 2000 events.

The event generator HEXF 4.0 [116] has been used, which is based on the phenomenological model of Hagiwara et al. (Sect. 2.2.2). This program includes initial-state radiation from the beam electron using the Weizsäcker-Williams approximation [117]. The MEPS model of LEPTO 6.1 [107] is implemented for the simulation of the QCD cascade, and JETSET 7.4 [108–110] for the hadronisation and the decays of unstable particles. The

[4] Except for $\nu^* \to \nu q\bar{q}$ and $e^* \to eq\bar{q}$, where the lowest mass generated is 110 GeV.

generated excited-lepton events have been fed into the same detector simulation and have undergone the same chain of reconstruction software as the simulated background events.

For excited electrons, a distinction is made between elastic, quasi-elastic and inelastic e^* production. In the first case, the proton is described by electric and magnetic form factors; in the second case, a phenomenological parameterisation by Brasse et al. [118] is used for the proton structure functions; in the inelastic case, the MRSA [119] parameterisation of the PDFs is employed, being accessible by an interface to the PDFLIB [120].

For excited neutrinos, since ν^* production proceeds via W exchange, only the inelastic case is implemented.

Apart from generating excited-lepton events, HEXF can be used to calculate e^* and ν^* production cross-sections for a given value of f/Λ. The cross sections are calculated within the framework of the narrow-width approximation (NWA). This approximation, i.e. the assumption that the excited leptons have zero decay width, is legitimate for small enough values of f/Λ. For $f/\Lambda = 1/1\,\text{TeV}$, which is the value used for generating the cross sections shown in Sect. 2.2.2, the NWA is well applicable, as demonstrated in [44].

5.3 The data samples

The experimental data employed for this analysis have been collected with the ZEUS detector in the years 1998–2000. The 98/99 e^-p and the 99/00 e^+p samples correspond to integrated luminosities of $16.7\,\text{pb}^{-1}$ and $66.1\,\text{pb}^{-1}$, respectively. The systematic errors on these luminosities are stated as 1.8 % and 2.25 %.

The data-taking came to an end in autumn 2000, when a one-year shutdown for the luminosity-upgrade of HERA was started. Prior to 1998, HERA operated with a lower proton energy (820 GeV), so that the samples analysed here comprise the complete ZEUS data recorded at 318 GeV centre-of-mass energy. Furthermore, these recent samples represent the largest available sets of e^-p as well as of e^+p data, since the ZEUS data collected prior to 1998 correspond to integrated luminosities of only $0.8\,\text{pb}^{-1}$ (e^-p) and $47.7\,\text{pb}^{-1}$ (e^+p), respectively.

As e^-p reactions offer much higher sensitivity for the ν^* search than e^+p reactions (Sect. 2.2.2), excited neutrinos have been sought using the 98/99 sample only. In contrast to that, since e^* production is independent of the charge sign of the incoming lepton, excited electrons have been searched for in both data sets.

From the higher centre-of-mass energy since 1998 the possibility follows to extend the mass region accessible to excited-lepton searches to higher values (the kinematic limit now being 318 GeV, in contrast to 300 GeV as prior to 1998). In addition, compared to previous ZEUS analyses, more stringent exclusion limits on excited-lepton production can be derived due to the increased statistics available.

5.4 Preselection

The preselection consists of two main steps. The first is common to all six channels and comprises the requirement of DST bits and a set of cuts and cleaning algorithms to reduce non-*ep* backgrounds. As a second step, a set of distinct cuts for each channel is applied, selecting types of final states that share the characteristics of the respective e^* or ν^* final state.

5.4.1 DST bits and background suppression

To start with, the DST bit preselection is applied. The conjunction of bits required is DST 37 $\wedge$ (DST 33 $\vee$ DST 34 $\vee$ DST 35 $\vee$ DST 36). This combination satisfies the needs of all decay channels under study,[5] selecting events with potentially interesting final states. The meanings of the individual DST bits are as follows (complete descriptions given in Appendix B):

- DST 37: requires vertex with $-60\,\text{cm} < Z_{\text{vtx}} < 120\,\text{cm}$, either reconstructed offline or on TLT level;
- DST 33: "neutral current", electron candidate with minimum energy of 8 GeV;
- DST 34: "charged current", missing transverse momentum (excluding the FCAL first inner ring) greater than 6 GeV;
- DST 35 and DST 36: "high E_T", different requirements on minimum transverse energy.

In addition to these requirements, cuts are applied to suppress backgrounds from non-*ep* processes, such as beam-gas and beam-wall reactions as well as cosmics and halo muons (Sect. 3.3):

- bunch crossing:
  it is required that a given event be assigned to a regular *ep* bunch crossing;
- good vertex:
  each event must have a tracking vertex with a longitudinal position of $|Z_{\text{vtx}}| < 50\,\text{cm}$ and a transverse position of $\sqrt{X_{\text{vtx}}^2 + Y_{\text{vtx}}^2} < 2.0\,\text{cm}$.

Furthermore, the following hardware malfunction needs to be dealt with, otherwise being likely to fake high-energy electrons:

[5] In fact, this requirement being common to all channels is for reasons of effectiveness: the preselection described here is applied when transforming the original event information, which is stored at the DESY site, into conveniently small units ("ntuples") with a data format that is appropriate to the processing on a local PC. With a common preselection, all data and background MC samples need to be processed and stored only once.

- spark suppression:
  in the BCAL there may randomly occur so-called sparks, which are discharges between single PM tubes and their bases. Sparks can fake large energy deposits in the respective cells, which may then be identified as high-energy electrons or photons. However, typically only one of the two independent PMs per cell experiences this effect, so that spark events can be identified and rejected by the large imbalance between both PM signals.

5.4.2 Channel-dependent cuts

The preselection criteria mentioned up to here are common to all decay channels under study. In contrast to that, the second step of the preselection comprises a distinct set of cuts for each channel, the purpose of which is to create decent samples of events with similar characteristics as the respective e^* or ν^* signals. The data and background events surviving these cuts are intended to exhibit satisfactory agreement in both numbers and distributions of relevant variables. Thereby, one can be confident to obtain reasonable background estimates as well when applying the final, tighter selection criteria. At the same time, the preselection cuts are intended to represent no serious obstacle for the signal MC events, i.e. not to reduce the efficiency too much.

The preselection cuts employed for the different decay channels are described in detail in Sects. 5.6.2 to 5.6.7.

Among these cuts are two requirements which feature the same sets of definitions in all decay channels where they are used:

- calorimeter timing:
  the CAL timing information is a useful tool to reject events containing particles not having originated from the nominal interaction region, such as beam-gas reactions. However, the CAL timing is not simulated reliably, so that in the MC samples it can serve neither as a check for the experimental data nor as a quantity to cut on. For that reason, CAL timing requirements are applied only in the decay channels featuring a neutrino in the final state ($\nu^* \to \nu\gamma$, $\nu^* \to \nu q\bar{q}$, $e^* \to \nu q\bar{q}'$). In those cases, which rely on missing transverse momentum rather than on a final-state electron, beam-gas reactions are more likely to fake the respective final states. The following timing cuts are applied: $|t_{\mathrm{FCAL}}|, |t_{\mathrm{BCAL}}|, |t_{\mathrm{RCAL}}|, |t_{\mathrm{FCAL}} - t_{\mathrm{RCAL}}|, |t_{\mathrm{CAL}}| < 6\,\mathrm{ns}$, where the time measurements of the different subcalorimeters are performed with respect to the bunch crossing, and t_{CAL} denotes the global CAL time;
- electromagnetic cluster:
  for all decay channels, either the presence or the explicit absence of an electron (or photon) candidate is required.
  For $\nu^* \to \nu\gamma$, $\nu^* \to eq\bar{q}'$ and $e^* \to eq\bar{q}$, one electromagnetic cluster found by EM

(Sect. 4.2.3) is required,[6] for $e^* \to e\gamma$ two such clusters. Both electron and photon candidates must satisfy the following cuts:

1.) EM probability $> 10^{-3}$;

2.) transverse energy: $E_T^{el,\gamma} > 10\,\text{GeV}$;

3.) isolation: $E_{\text{iso}} < 5\,\text{GeV}$.

To be distinctly accepted as an electron, an electromagnetic cluster must fulfil the additional requirements listed below:

- for $\theta_{el} \geq 0.3\,\text{rad}$: existence of a matching track with DCA $< 10\,\text{cm}$ and $p_{\text{trk}} > 5\,\text{GeV}$;
- for $\theta_{el} < 0.3\,\text{rad}$: EM probability $> 10^{-2}$;

however, to be accepted as a photon:

- no matching track with DCA $< 10\,\text{cm}$.

In contrast to that, for $\nu^* \to \nu q\bar{q}$ and $e^* \to \nu q\bar{q}'$, events are rejected if they contain (at least) one electromagnetic cluster found by EM which satisfies the criteria listed under 1.) and 2.). In succeeding sections, this is referred to as "electron veto".

5.5 Event selection

5.5.1 Fixed Cuts

Being one of the two alternative approaches employed for this analysis, fixed[7] cuts are applied to obtain the final sets of candidate and background events. Similar to the last stage of the preselection, there is a special set of cuts for each of the six channels under study. Essentially, the same variables as in the respective preselection are now used to cut on, but more restrictively than before.

The choice of cuts has been motivated by the attempt to drastically reduce the numbers of background events, while at the same time preserving a high signal efficiency. In some of the channels, the signatures of the low-mass and the high-mass samples, respectively, would lead to considerably different choices of cut values for some of the variables. For instance, the peak value of the E_T^{el} distribution in the $\nu^* \to eq\bar{q}'$ decay varies greatly depending on the ν^* mass (Sect. 5.6.6). Here a tight cut on E_T^{el} would be particularly effective in reducing the NC DIS background and would hardly affect the higher ν^* masses. It would, however, mean to decrease the signal efficiency at low masses.

[6] If there is more than one candidate, the one with the highest EM probability is chosen.

[7] The label "fixed" is used to distinguish these cuts from the variable, non-fixed criteria of the second selection method.

In such cases, effective background suppression and high efficiencies in the high-mass region have been given priority over retaining the low-mass efficiencies.[8] The main interest focusses on the higher masses, particularly on those close to the kinematic limit. For the lower mass range has been investigated extensively in the past, leaving dim prospects to discover an excited lepton below about 150 GeV. To put it straight: if there is such a particle to be discovered within the reach of HERA, its mass is likely to be in the upper range.

To some degree, the concrete choice of cut values remains somewhat arbitrary and a matter of taste. Thus, one might demand a more systematic procedure to optimise the selection criteria. For that reason, as an alternative approach, the second selection method, which is presented in detail in the next section, has been developped.

The immediate outcome of applying the selection cuts are mass spectra of candidate events and expected backgrounds. Further treatment of these results is described in Sect. 5.6.9.

5.5.2 Probability method

The second selection approach is referred to as "probability method". Its basic idea is to replace the fixed cuts by a probability-based procedure which projects a multi-dimensional parameter space on a single variable. This method is intended to be more flexible and more sensitive than the conventional approach. Furthermore, its working principle facilitates the optimisation of the selection criteria in a systematic way.

For convenience and to simplify comparison, the same variables as for the conventional method are made use of in each channel. Yet no fixed cuts are imposed on the single variables, but a combined probability is derived which is then subjected to a cut. The whole procedure consists of two main steps: the first, as a necessary prerequisite, is to generate a set of reference histograms containing probability distributions for the variables considered; the second step represents the actual event selection, where for a given event an overall probability is calculated and finally imposed a cut upon.

To start with, each variable employed in a given channel is transformed into a probability distribution. For the respective quantity the distributions of all ten signal MC mass samples are superimposed into a single histogram. This approach, which might seem somewhat unusual, is discussed at length further on in this section.

After having generated the superimposed histograms of the relevant quantities, transformations into probability distributions are performed. That is achieved by integrating the

[8] To a certain degree, a similar situation has already been present in the respective channels when working out the preselection cuts. At the lowest masses considered (100 GeV, 110 GeV) this may lead to substantially reduced signal efficiencies.

variable distributions appropriately. Depending on the nature of the respective variable in the fixed-cut scenario, three cases are distinguished:

1.) Variables for which the signal events typically feature small values, equivalent to an upper bound used for the fixed cuts. As an example, the θ_{el} distribution for the $e^* \to e\gamma$ decay is shown in Fig. 5.1. The cut used in the conventional approach is $\theta_{el} < 2.0\,\text{rad}$. Here the integration is performed according to:

$$P(x) = \frac{\int_x^\infty f(x')dx'}{\int_0^\infty f(x')dx'}\,, \tag{5.1}$$

where, in the given example, $P(x)$ represents the probability for an excited electron to yield a θ_{el} value of greater than x. The integral in the denominator of (5.1) simply represents the total number of events in the histogram considered.

2.) There exist as well quantities for which the signal events exhibit particularly large values. That corresponds to a lower bound employed for the fixed cuts, e.g. $E_T^{el} > 30\,\text{GeV}$ in the $e^* \to e\gamma$ decay. To obtain the corresponding probability distribution (Fig. 5.1), the integration is now carried out as follows:

$$P(x) = \frac{\int_0^x f(x')dx'}{\int_0^\infty f(x')dx'}\,, \tag{5.2}$$

where in this case $P(x)$ represents the probability for an excited electron to yield an E_T^{el} value of less than x.

3.) The third case refers to variables on which both an upper and a lower constraint are imposed in the fixed-cuts approach. This typically applies to the longitudinal energy-momentum variable, δ, e.g. $35\,\text{GeV} < \delta < 65\,\text{GeV}$ used for $e^* \to e\gamma$. To obtain the probability distribution, at first the respective distribution $f(x')$ is transformed into a new distribution $g(y')$ by calculating the absolute difference between any value x' and the maximum, $\hat{x}$, of the former distribution: $y' = |\hat{x} - x'|$. An example is displayed in Fig. 5.2. The resulting distribution is then integrated as in (5.1):

$$P(y) = \frac{\int_y^\infty g(y')dy'}{\int_0^\infty g(y')dy'}\,, \tag{5.3}$$

yielding, for the above example, the probability $P(y)$ for the quantity $|\hat{\delta} - \delta|$ to be larger than y. This procedure is applicable only to variables which feature essentially symmetrical distributions around their maxima. Indeed, this holds for the cases where it is applied in this analysis.

Once the probability distributions have been generated, the second step, namely the actual event selection, is straightforward. For a given event, for each of the N relevant variables

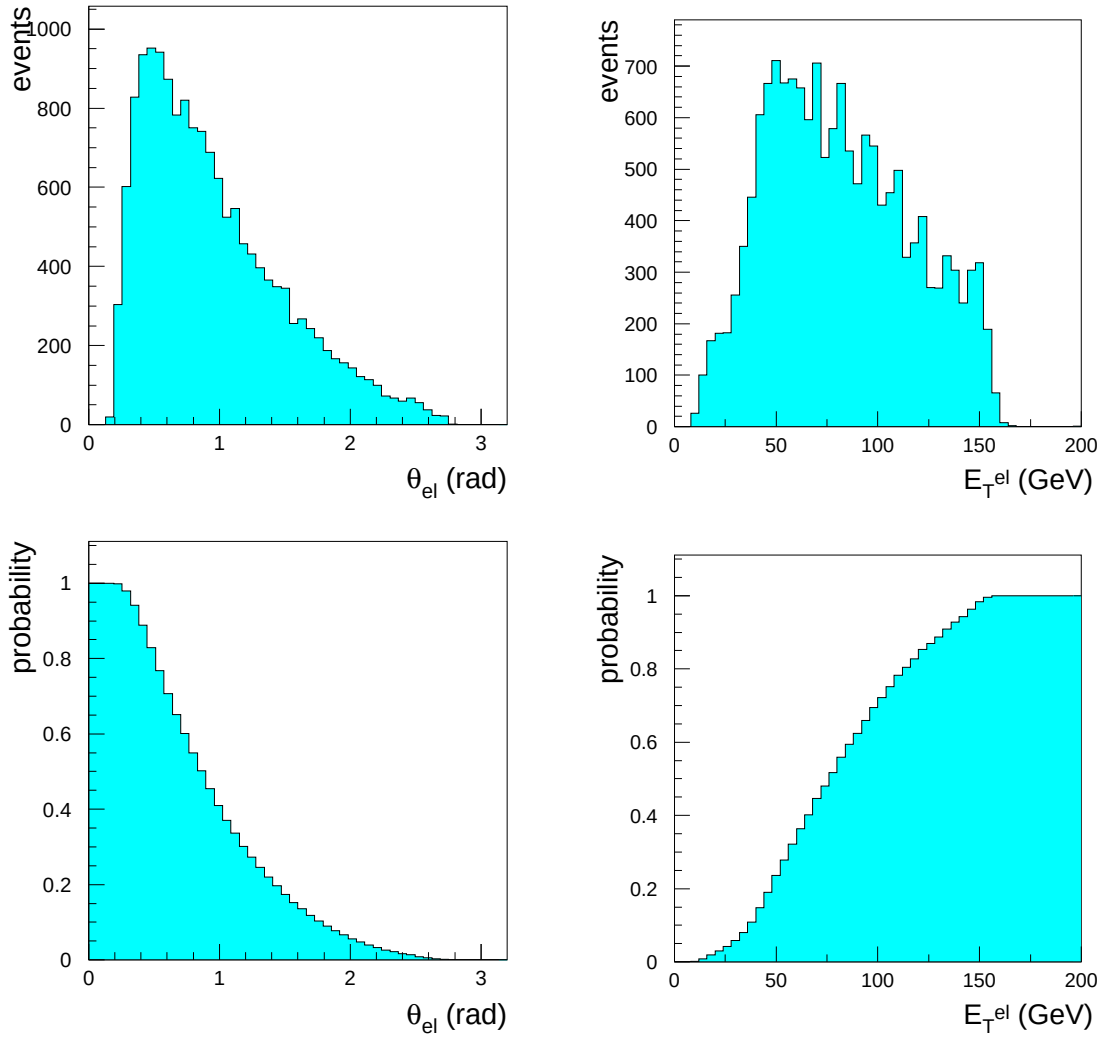

Figure 5.1: *Examples illustrating the generation of the probability distributions. Upper row: Superimposed $e^* \to e\gamma$ distributions of θ_{el} and E_T^{el}. The former is an example of a variable for which an upper cut is used in the conventional selection approach; the latter represents a variable on which a lower cut is imposed conventionally. Lower row: The corresponding probability distributions obtained by integration.*

the corresponding probability, P_i, is read off the respective reference histogram.[9] The single numbers are then multiplied to yield the total probability, P_{tot}:

$$P_{\mathrm{tot}} = \prod_{i=1}^{N} P_i \ . \tag{5.4}$$

[9] Due to aesthetical reasons, one might prefer to use a smooth parameterisation rather than a histogram. However, no actual gain in functionality would result from that. The histogram binning chosen does not bias the results of the procedure, which, as a systematic check, has been verified by varying the bin width.

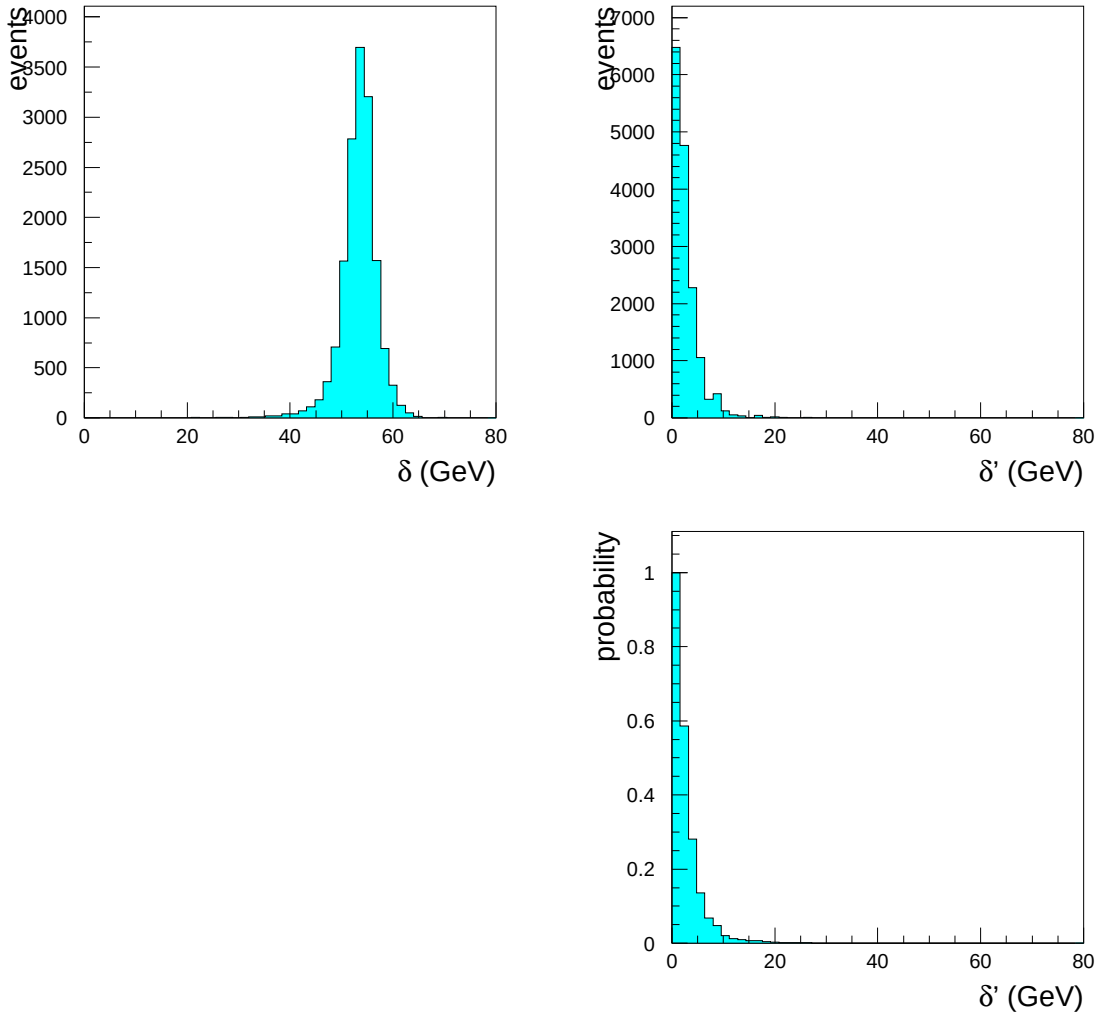

Figure 5.2: *Upper left: Superimposed $e^* \to e\gamma$ distributions of the longitudinal energy-momentum variable, δ. upper right: The transformed distribution, δ'. Lower right: The corresponding probability distribution following from integration.*

Furthermore, P_{tot} is normalised with respect to the number of variables included:[10]

$$P'_{\text{tot}} = \sqrt[N]{P_{\text{tot}}} \ . \tag{5.5}$$

The normalised probability, P'_{tot}, constitutes the single variable upon which, finally, a cut is imposed.

Yet one aspect remains to be clarified, namely how to choose the specific value for the cut on P'_{tot}. For that purpose, a systematic approach is followed: as the optimal cut on P'_{tot} the one that yields the most stringent average expected limits is considered. The

[10] This last step adds no substantial content; however it helps to handle the respective numbers in a concrete case, since it causes the P'_{tot} values of different channels to attain comparable sizes although different numbers of variables are involved.

latter are obtained by summing up, for all possible numbers of events observed in a given mass window, the respective cross-section limit weighted with the corresponding Poisson probability:

$$\langle \sigma \times \mathrm{BR} \rangle_{ul} = \sum_{n=0}^{\infty} P(n, b)(\sigma \times \mathrm{BR})_{ul} \,, \tag{5.6}$$

where $P(n, b)$ denotes the Poisson probability to observe n events when b events are expected, and where $(\sigma \times \mathrm{BR})_{ul}$ is the upper limit obtained for n candidates and b background events in a given mass window. The calculation of these limits is described in detail in Sect. 6.1. Deriving the expected limits involves no experimental data, as the information used stems from simulation only.

In a given channel, the event selection is performed repeatedly for a number of different cuts on P'_{tot}. In each case the expected limits are then calculated from the resulting distributions of background events. Finally, the different expected-limit curves are compared, and a decision is taken in favour of the P'_{tot} cut yielding the most stringent limits.[11]

The cut on P'_{tot} thus chosen is then employed to obtain the final search results. Compared to the fixed cuts, a somewhat better overall performance is achieved by the probability method. The results obtained with that approach have therefore been chosen as a basis to derive the exclusion limits presented in Sect. 6. Detailed results as well as comparisons between both selection methods are given, separately for each decay channel, in the following sections.

As mentioned before, the superposition of different mass samples into a single histogram might appear a bit odd at first sight. However, combining the different masses this way is a valid approach, as will be argued in the following. When comparing the distributions of a given variable among e^* or ν^* samples of different masses, it is obvious that no sudden jumps occur in the shapes of these distributions. On the contrary, just as one would expect, smooth transitions between the different samples are observed. Thus, superimposing different masses can be understood as creating histograms of physical quantities for a given process (e^* or ν^* decay) with a variable parameter (the mass).

One might propose that employing a single mass sample for the reference distributions would suffice as well. This has been tested and rejected, since the efficiencies are then maximised only around the chosen mass, while falling off elsewhere.

The straight superposition (with equal weights) represents a particularly simple way of employing all the signal masses. Alternatively, one could think of separate probability distributions for each mass sample, leading to mass-dependent selection criteria. In the event selection presented up to here, mass-dependent cuts have not been made use of

[11] In practice one cannot expect one cut value to yield the most stringent limits over the complete mass range considered. Thus the decision implies some preference in which mass region the sensitivity be optimised.

(the only exception being $M_{\mathrm{tot}}/M_{\mathrm{rec}}$). This has been done on purpose, since the mass reconstruction is not free of shifts and resolution effects. Furthermore, in the case of the probability method, a procedure operating mass-dependently would suffer from being considerably more complicated than the simple superposition approach.

Finally, it can be said that the procedure applied has proven to yield competitive results, thereby being justified a posteriori on heuristic grounds.

5.6 Analyses of the decay channels

5.6.1 Overview

In the following sections, the concrete selection criteria applied as well as their outcome are presented for the e^* and ν^* channels under study. For each decay channel the final-state topology is discussed. The preselection cuts are stated and comparison plots of the experimental data and the simulated backgrounds are shown. As for the final event selection, both the fixed cuts and the probability method are presented. In case of the latter approach, expected limits are derived and used to decide about the favourable cut on P'_{tot}. The resulting event numbers as well as the efficiencies, resolutions and mass shifts are listed separately for each channel. In Sects. 5.6.8 and 5.6.9, a graphical overview of the key results for all six channels is given: the selection efficiencies and the results of the mass reconstruction are shown, as well as examples of the reconstructed signal masses; moreover, the invariant-mass spectra of the candidate and background events are displayed. Finally, the contents of the mass spectra undergo a statistical test to reveal possible indications of a signal.

There exist different options of categorising the excited-lepton decay channels. The most obvious is the distinction between e^* and ν^* decays. Another possible set of categories is provided by the gauge boson involved (γ, W or Z). A third aspect of distinction is represented by the experimental signatures.

As for the signatures, the six decay channels studied can be divided into two classes: NC-like and CC-like decays. The former feature an electron in the final state, whereas the latter are characterised by a final-state neutrino, leading to missing transverse momentum.

The NC-like channels are $e^* \to eq\bar{q}$, $\nu^* \to eq\bar{q}'$ and $e^* \to e\gamma$. The two channels featuring a hadronically decaying gauge-boson have similar event topologies, and thus similar selection criteria are used. The background to these two channels arises predominantly from NC DIS events. For $e^* \to e\gamma$, with a high-energy photon being present in addition to the final-state electron, the situation is somewhat different. Here an additional major background is constituted by QED-Compton events. The $e^* \to e\gamma$ final state exhibits a

particularly clean experimental signature, so that high efficiency and strong suppression of backgrounds can be achieved simultaneously.

The CC-like channels are $e^* \to \nu q\bar{q}'$, $\nu^* \to \nu q\bar{q}$ and $\nu^* \to \nu\gamma$. Again, the two decays involving hadrons in the final state are characterised by similar experimental signatures. In this case, the major source of background is given by CC DIS events. A somewhat special role is again played by the photonic decay mode, $\nu^* \to \nu\gamma$, where a high-energy photon coinciding with a large amount of $\not{p}_T$ constitutes a quite unusual signature.

The succeeding sections are organised as follows: The individual analyses of the six decay channels are presented in Sects. 5.6.2 to 5.6.7. For clearness and to facilitate comparison, graphical representations of the efficiencies and mass resolutions for all channels are given in Sect. 5.6.8. The same holds for the resulting mass spectra which are shown and discussed in Sect. 5.6.9. Finally, conclusions are presented in Sect. 5.6.10.

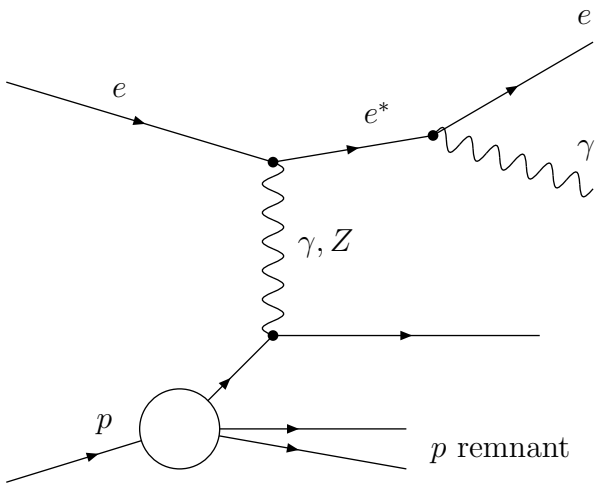

Figure 5.3: *Feynman diagram for excited-electron production in inelastic ep scattering, with the subsequent decay $e^* \to e\gamma$.*

5.6.2 $e^* \to e\gamma$

Excited-electron production proceeds via t-channel γ or Z exchange. About half of the excited electrons are expected to be produced elastically, with the proton disappearing undetected in the forward beampipe (Sect. 2.2.2). The photonic decay mode, $e^* \to e\gamma$, exhibits a very prominent signature: two isolated, high-energy electromagnetic clusters, one of which has, if inside the CTD acceptance, a matching track. Typically, no further detector activity is observed, except for possible energy deposits by the proton remnant around the forward beampipe. In Fig. 5.3 the corresponding Feynman diagram is displayed for the case that the e^* is produced inelastically. Some key distributions of characteristic quantities obtained from the signal MCs are shown in Fig. 5.4.

The same experimental signature can be generated by QED-Compton and neutral-current DIS events. As for the latter, the final-state photon is likely to stem from a π^0 decay. Yet these background events typically feature smaller transverse momenta of the electron and photon than is the case for the e^* decays. In addition, the e^* events can be distinguished by their decay products' being boosted in the forward direction.

The preselection requires one electron plus one photon (and no further electromagnetic clusters) to be found applying the criteria given in Sect. 5.4.2. Further preselection cuts, which are used for generating the control plots (Fig. 5.5), are listed in Table 5.1. That table contains in addition the signal efficiencies after the preselection cuts as well as the

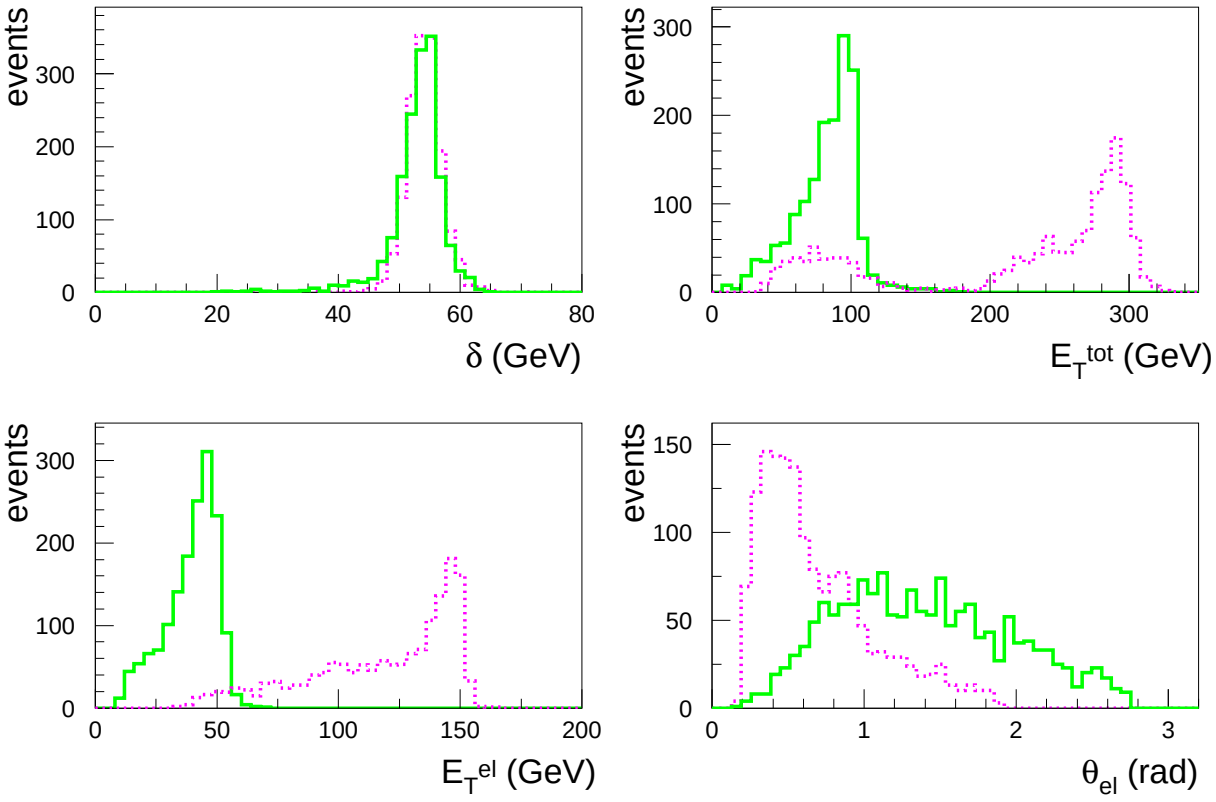

Figure 5.4: *Example distributions of characteristic quantities for the simulated signals. Each distribution is shown for two different masses, namely* 100 *GeV (solid line) and* 300 *GeV (dotted line). The* E_T^{γ} *and* θ_{γ} *distributions, which are not shown here, are similar to the* E_T^{el} *and* θ_{el} *distributions, respectively.*

numbers of data and background events.[12] As can be seen from Fig. 5.5, the data are well described by the background MC.

As for the actual event selection, the requirements applied in the framework of the fixed-cut method are stated in Table 5.2. For the alternative selection approach, the same variables are employed in terms of probability distributions. To determine the final P'_{tot} cut value, the probability method has been applied to the background and signal MC samples using different cuts on P'_{tot}. The expected limits obtained are plotted in Fig. 5.6, where the corresponding curve resulting from the fixed-cut approach is shown as well. Generally speaking, a tighter cut on P'_{tot} means more stringent limits in the high-mass region and less stringent limits in the low-mass region. The choice of the cut value is a compromise guided by the aim to improve the search sensitivity in the high-mass region,

[12] Here as well as in the corresponding tables in the following sections, the statistical uncertainty is stated for the total number of background events, N, in the respective case. This uncertainty deviates from the naively expected $\pm\sqrt{N}$, because the MC samples are normalised to the data luminosity, and, moreover, N in fact emerges from the composition of several distinct MC samples, which represent either different types of ep reactions or different Q^2 ranges of a given process.

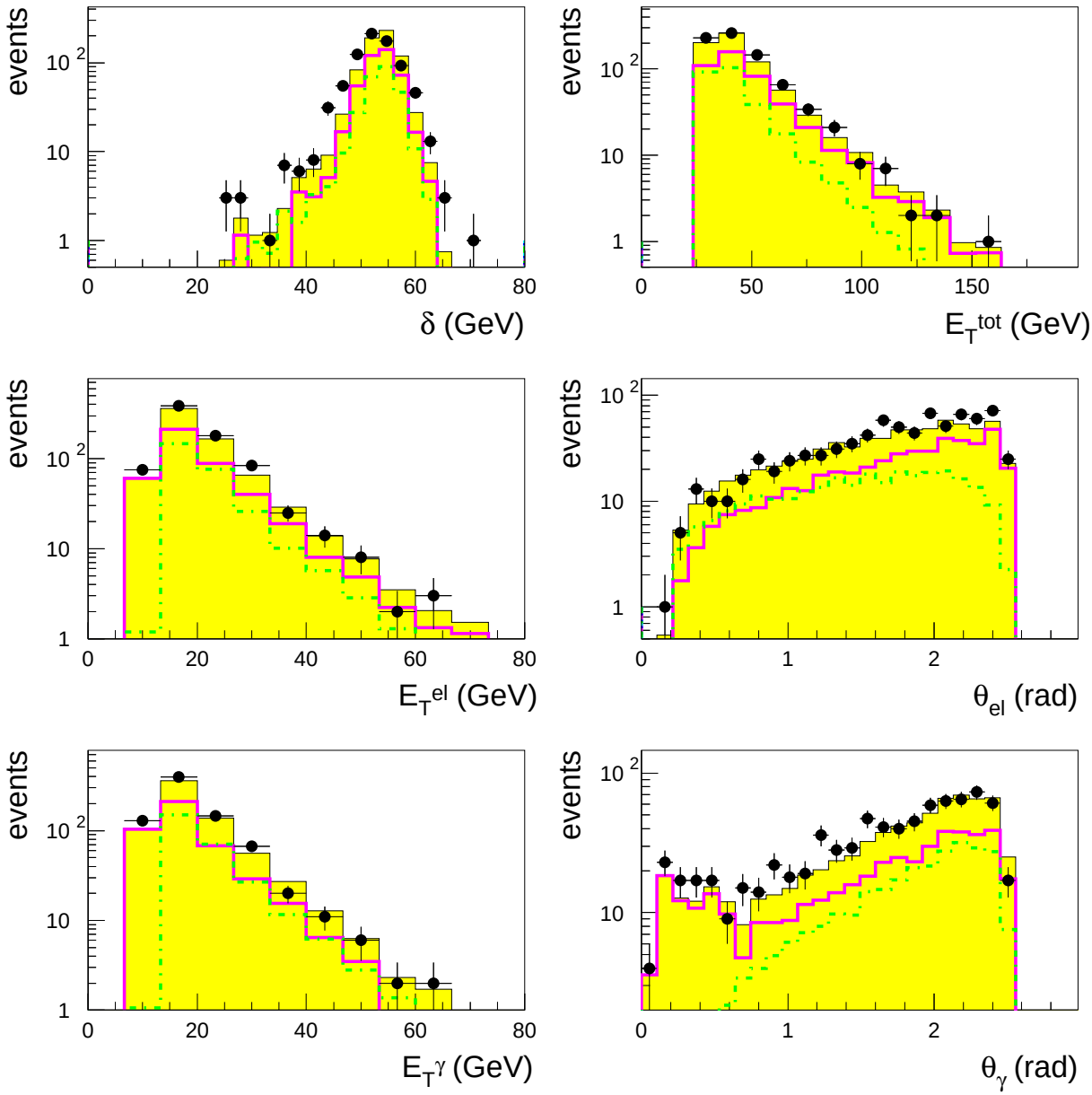

Figure 5.5: *Control plots comparing the experimental data (dots) and the expected background (filled histogram) after the preselection cuts. The individual contributions from NC DIS (solid line) and QED-Compton scattering (dash-dotted line) are displayed as well.*

$e^* \to e\gamma$ preselection cuts	
E_T^{el}	$> 10\,\text{GeV}$
E_T^{γ}	$> 10\,\text{GeV}$
θ_{el}	$< 2.5\,\text{rad}$
θ_{γ}	$< 2.5\,\text{rad}$
δ	$\in (20, 75)\,\text{GeV}$
E_T^{tot}	$> 30\,\text{GeV}$

event numbers	
observed:	**779**
98/99:	163
99/00:	616
expected:	**711 ± 14**
NC DIS:	440
QED-C.:	271

M_{e^*} [GeV]	eff. [%]	M_{e^*} [GeV]	eff. [%]
100	75.2	225	78.1
125	75.3	250	77.4
150	74.6	275	76.7
175	74.1	300	75.3
200	74.8	310	74.8

Table 5.1: *Preselection cuts, resulting event numbers and efficiencies. For the total number of background events, the statistical error is stated. The masses of the different signal MC samples are denoted by M_{e^*}. For each sample the efficiency is calculated as the ratio of the number of generated events (2000) and the number of events after the preselection. In all cases the statistical errors of the efficiencies are approximately ±1 %.*

without paying too high a price at lower masses. Thus, a cut value of $P'_{\text{tot}} > 0.20$ has been chosen to obtain the final results with the probability method.

The signal efficiencies and final event numbers obtained with either selection approach are listed in Table 5.2. The mass resolutions and mass shifts are stated for the probability method only, since the corresponding results obtained with the fixed cuts are quite similar.

In addition, the efficiency and resolution plots are shown in Sect. 5.6.8. The resolutions and mass shifts have been determined from the signal samples after applying the probability-based selection. For the resolution, the RMS value of the respective mass distribution is employed; the shift is calculated as the difference between the mean of the measured distribution and the nominal mass value. Examples of the reconstructed-mass distributions of the simulated signal events are given in Sect. 5.6.8. The mass spectra containing the candidate and background events for either approach are shown in Sect. 5.6.9, together with the respective probability curves obtained from the statistical tests of the spectra.

No excess of events is observed.

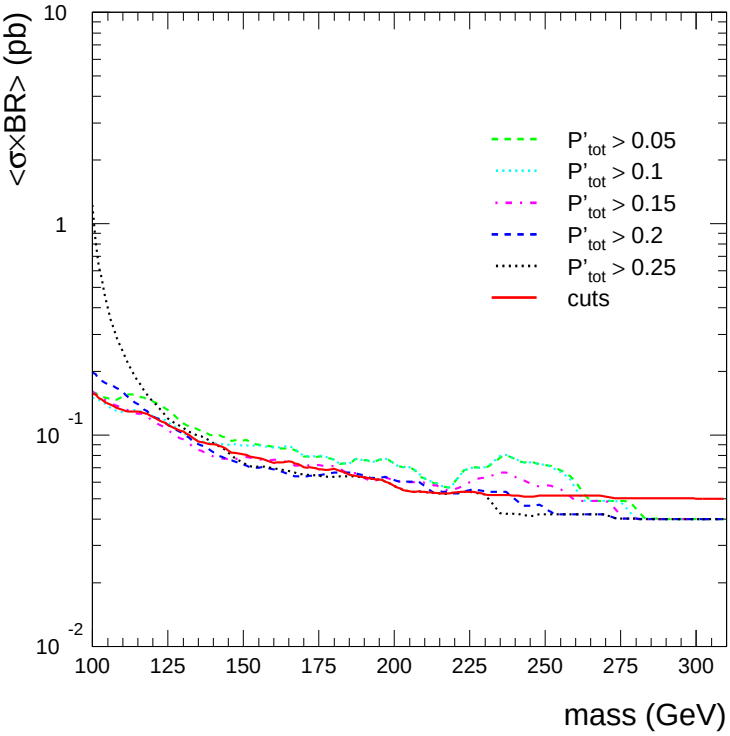

Figure 5.6: *Expected limits on $\sigma \times \mathrm{BR}$ for $e^* \to e\gamma$, obtained with the fixed-cut approach (solid line) and with the probability method using different cuts on the total probability, P'_{tot}. The lower bounds on P'_{tot} which correspond to the different line types are given in the key.*

fixed cuts (A)	
E_T^{el}	$> 30\,\mathrm{GeV}$
E_T^{γ}	$> 30\,\mathrm{GeV}$
θ_{el}	$< 2.0\,\mathrm{rad}$
θ_{γ}	$< 2.0\,\mathrm{rad}$
δ	$\in (35, 65)\,\mathrm{GeV}$
E_T^{tot}	$> 30\,\mathrm{GeV}$
$\theta_{el} + \theta_{\gamma}$	$< 2.5\,\mathrm{rad}$

final event numbers		
	A	B
observed:	**26** $(11 + 15)$	**11** $(4 + 7)$
expected:	$\mathbf{33.5 \pm 1.5}$	$\mathbf{13.6 \pm 1.0}$
NC DIS:	15.9	8.3
QED-C.:	17.6	5.3

$\boldsymbol{e^* \to e\gamma}$

M_{e^*} [GeV]	efficiency [%]		resol.	shift
	A	B	[GeV]	[GeV]
100	60.9	30.5	3.2	3.0
125	67.5	59.4	4.2	1.7
150	71.1	67.4	4.4	1.3
175	70.9	70.1	5.0	0.6
200	68.1	70.5	5.2	0.6
225	69.6	74.8	6.1	0.9
250	69.6	74.5	6.1	−0.1
275	70.2	74.9	6.6	1.2
300	70.6	74.7	7.4	1.3
310	70.3	74.0	8.2	1.2

Table 5.2: *The final event numbers resulting from the fixed cuts (A) and the probability method (B), respectively. Furthermore, the selection efficiencies for both approaches are listed, as well as the mass resolutions and mass shifts, which have been obtained with the probability method. The numbers of events observed in the 98/99 and 99/00 running periods, respectively, are given separately in brackets.*

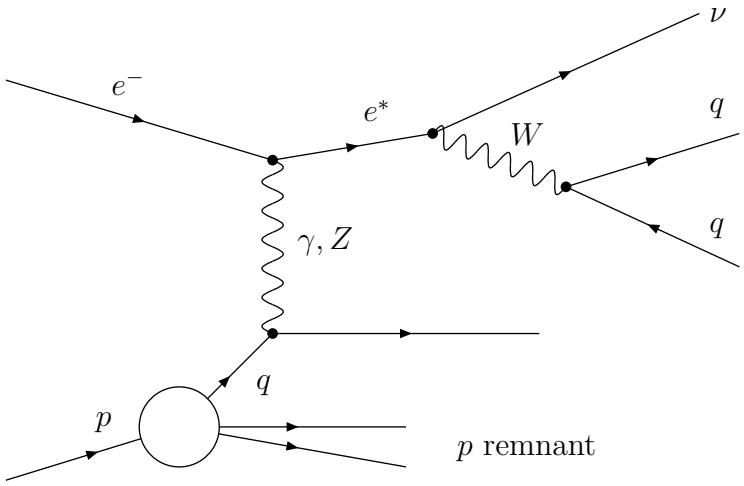

Figure 5.7: *Feynman diagram for (inelastic) e^* production with the subsequent decay $e^* \to \nu W \to \nu q\bar{q}'$.*

5.6.3 $e^* \to \nu W \to \nu q\bar{q}'$

With the W boson decaying predominantly to hadrons (BR = 68 %), the most likely final state in the $e^* \to \nu W$ decay mode is $\nu q\bar{q}'$. The topology of this final state is characterised by a large amount of missing transverse momentum due to the neutrino escaping undetected as well as by two hadronic jets from the W decay. If the excited electron is produced inelastically, a third jet from the struck parton may be observed. Owing to the W decay, the hadronic final state exhibits large transverse energy and a large invariant mass. The latter is expected to peak around the value of the W mass. The distributions of the key quantities in the signal MC samples are shown in Fig. 5.8.

The dominant background process to this channel is given by multi-jet CC DIS. At the preselection level, the PHP background is substantially reduced by a tight cut on $\not{P}_T$ (Table 5.3), which at the same time reduces the efficiency for the lowest-mass signals ($M_{e^*} = 100\,\text{GeV}$). The amount of $\not{P}_T$ increases substantially with the e^* mass, so that the other signal samples are hardly affected by this cut. In addition, the preselection comprises the set of cuts listed in Table 5.3 as well as an electron veto and constraints on the CAL timing (Sect. 5.4.2). The cut on the minimal fraction of vertex tracks, $\#^{\text{vtx}}_{\text{trk}}/\#^{\text{tot}}_{\text{trk}} > 0.2$, is useful to suppress events with overlaying beam-gas reactions, which typically feature large numbers of non-vertex tracks; these processes may otherwise fake large deposits of transverse energy. For similar reasons, the spark rejection (Sect. 5.4.1) has turned out particularly useful for the final state under study.

At the preselection level, there is good overall agreement between the data and the background simulation (Fig. 5.9). The cuts applied at this stage are tight already, so that only a relatively small number of events is left to the further selection procedure.

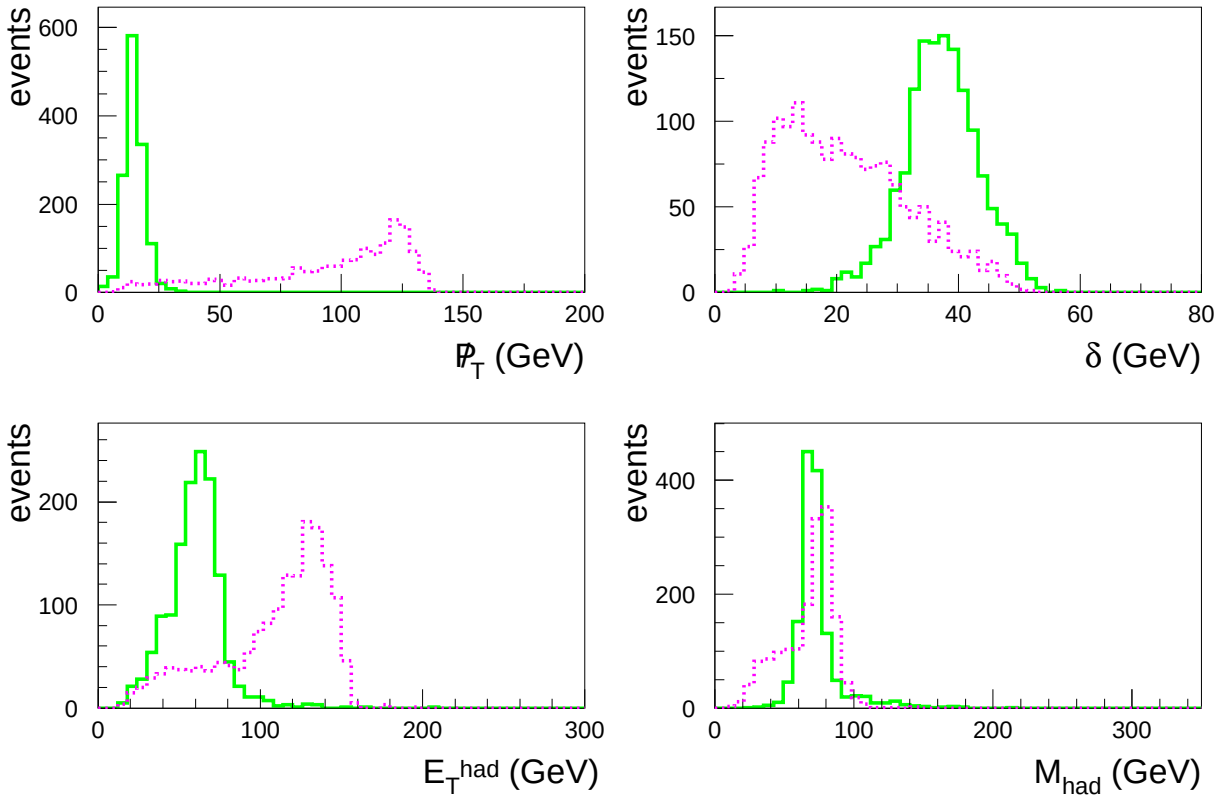

Figure 5.8: *Signal distributions of the $e^* \to \nu q\bar{q}'$ samples with masses of 100 GeV (solid contour) and 300 GeV (dotted contour). As expected, the M_{had} peak is found close to the W mass; the shift to somewhat lower values is likely to be caused by energy leakage and by energy loss in dead material.*

$e^* \to \nu W \to \nu q\bar{q}'$ preselection cuts	
$\not{P}_T$	$> 20\,\mathrm{GeV}$
δ	$\in (10, 50)\,\mathrm{GeV}$
E_T^{had}	$> 50\,\mathrm{GeV}$
M_{had}	$> 40\,\mathrm{GeV}$
$M_{\mathrm{had}}/E_T^{\mathrm{had}}$	$\in (0.4, 1.6)$
$\#_{\mathrm{trk}}^{\mathrm{vtx}}/\#_{\mathrm{trk}}^{\mathrm{tot}}$	> 0.2

event numbers	
observed:	**223**
98/99:	67
99/00:	156
expected:	**228 ± 14**
NC DIS:	5.7
CC DIS:	148.1
PHP	74.1

M_{e^*} [GeV]	eff. [%]	M_{e^*} [GeV]	eff. [%]
100	5.7	225	68.0
125	54.4	250	66.4
150	68.8	275	63.0
175	72.9	300	59.5
200	71.2	310	58.0

Table 5.3: *Cuts, resulting event numbers and efficiencies after the preselection. The statistical errors of the efficiencies are about ±1 %. As for the number of observed events, the individual contributions from the e^-p (98/99) and e^+p (99/00) data samples are listed as well. Control plots of the data and MC events surviving the preselection cuts are shown in Fig. 5.9.*

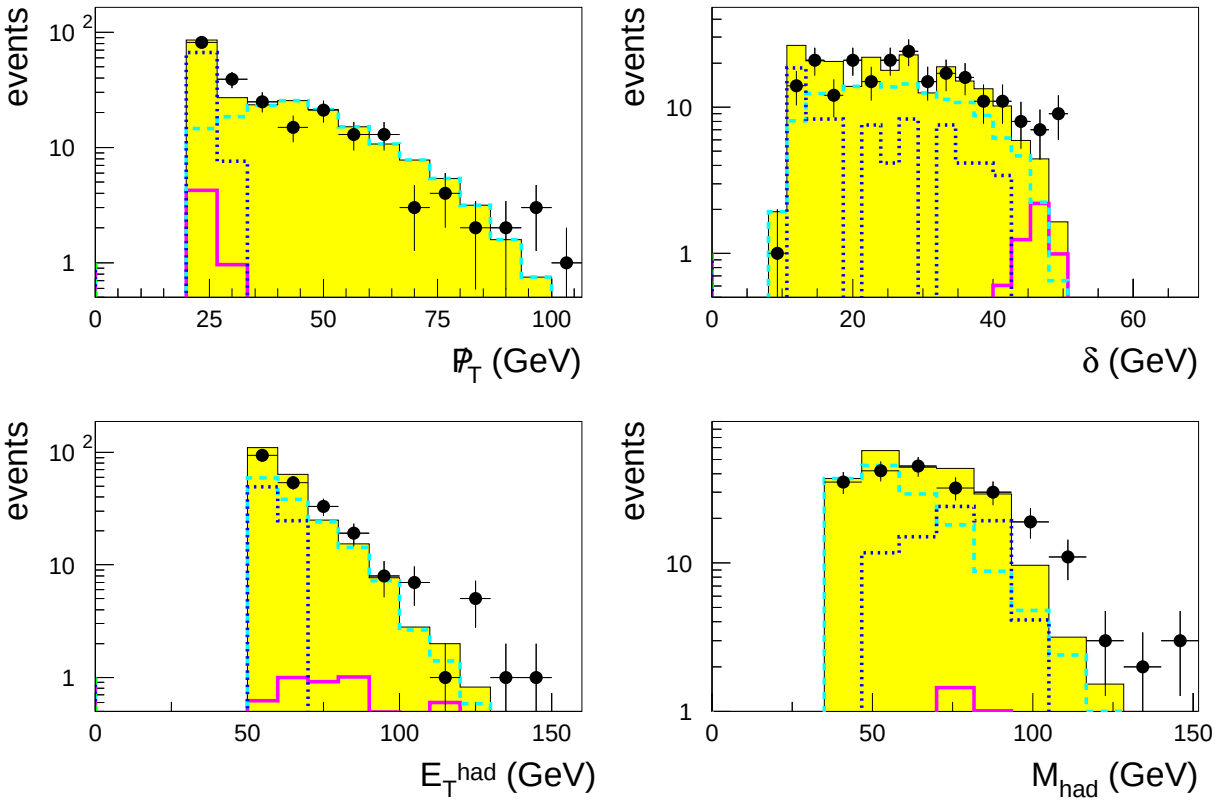

Figure 5.9: *Control plots to check the normalisation between the experimental data and the corresponding Monte Carlo simulations. The dots with error bars represent the data. The total expected background (filled histogram) receives contributions from CC DIS (dashed line), photoproduction (dotted) and some few NC DIS events (solid line). The $\not\!\!P_T$, E_T^{had} and M_{had} distributions' being sliced off at the lower ends is due to the respective preselection cuts.*

In case of the final event selection by fixed cuts, the same variables as for the preselection are used, however imposing somewhat stronger requirements. It turns out that the probability method does not yield a gain in terms of more stringent expected limits (Fig. 5.10). Nonetheless, the probability approach is adopted to obtain the final results in this decay channel, since it provides superior overall performance when considering all six channels. The probability cut chosen is $P'_{\mathrm{tot}} > 0.35$.

The results of the event selection are stated in Table 5.4. Both methods yield comparable event numbers. Efficiency and resolution plots are shown in Sect. 5.6.8, as well as sample mass distributions. Among all decay channels studied, the coarsest resolutions and the largest mass shifts are observed for the final states containing a neutrino plus quarks. That is due to the momentum components of the neutrino not being measured directly but inferred from $\not\!\!P_T$ and from the longitudinal energy-momentum variable, δ (Sect. 4.3).

No excess of candidate events over the expected background is observed.

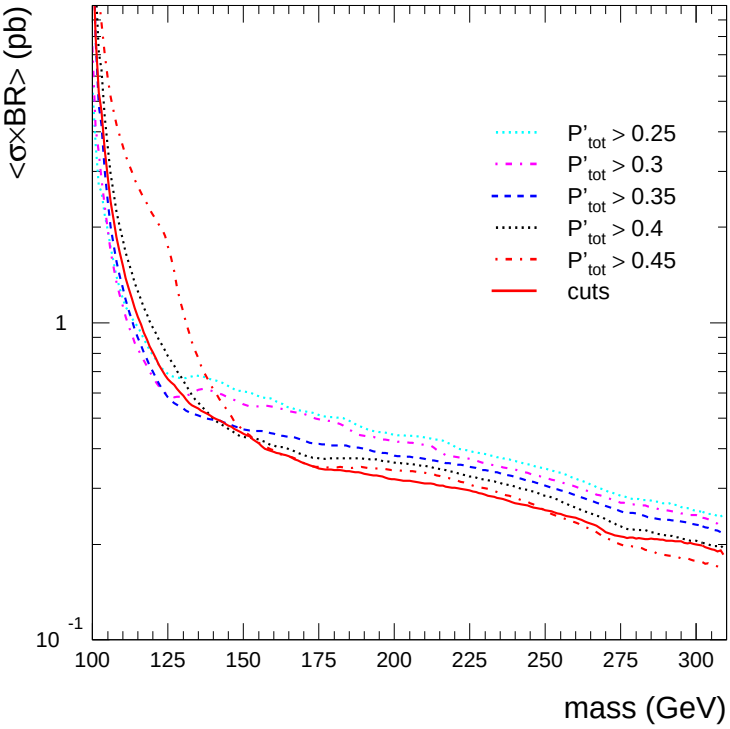

Figure 5.10: *Expected limits on $\sigma \times$ BR for $e^* \to \nu q\bar{q}'$. The solid curve represents the selection by fixed cuts, whereas the other curves represent the probability method. The different cuts on P'_{tot} are indicated by the line types. Here $P'_{\text{tot}} > 0.35$ is chosen to obtain the final results with the probability method.*

fixed cuts (A)	
$\not{P}_T$	$> 25\,\text{GeV}$
δ	$\in (10, 50)\,\text{GeV}$
E_T^{had}	$> 60\,\text{GeV}$
M_{had}	$> 50\,\text{GeV}$
$M_{\text{had}}/E_T^{\text{had}}$	$\in (0.5, 1.5)$

final event numbers		
	A	B
observed:	**69** $(27 + 42)$	**75** $(33 + 42)$
expected:	$\mathbf{65.4 \pm 4.9}$	$\mathbf{72.7 \pm 1.1}$
NC DIS:	1.9	0.5
CC DIS:	55.2	72.2
PHP	8.3	0.0

$\boldsymbol{e^* \to \nu W \to \nu q\bar{q}'}$

M_{e^*} [GeV]	efficiency [%]		resol. [GeV]	shift [GeV]
	A	B		
100	1.1	0.4	6.9	19.4
125	33.8	25.8	7.3	2.4
150	54.7	49.5	9.3	−2.4
175	65.4	61.0	10.5	−6.8
200	65.8	63.5	12.3	−11.3
225	63.8	63.2	14.5	−17.4
250	62.5	62.6	16.5	−22.6
275	58.5	60.5	18.8	−27.6
300	52.6	57.2	23.3	−34.8
310	52.1	55.9	24.5	−37.5

Table 5.4: *Final outcome of the $e^* \to \nu q\bar{q}'$ search, comprising the fixed cuts and the resulting event numbers for both selection methods, as well as the efficiencies, resolutions and mass shifts obtained from the signal MC samples. The cut approach is denoted by A, whereas the probability method is labelled by B. The numbers of events observed in the 98/99 and 99/00 running periods, respectively, are stated in brackets.*

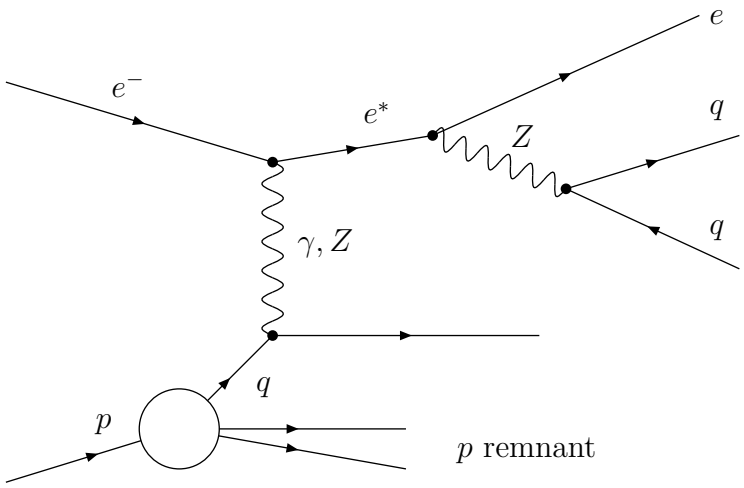

Figure 5.11: *Feynman diagram for $e^* \to eZ \to eq\bar{q}$. Depicted here is the case where the excited electron is produced inelastically.*

5.6.4 $e^* \to eZ \to eq\bar{q}$

Owing to the large branching ratio of hadronic Z decays (70 %), the $eq\bar{q}$ final state is the most probable to occur in $e^* \to eZ$ decays. The topology of this final state features a forward-going electron with high transverse energy as well as large values of E_T^{had} and M_{had}. The hadronic-mass distribution is expected to exhibit a peak around the Z mass. The most significant difference among the signal samples with different masses is observed for the variable E_T^{el}. As depicted in Fig. 5.12, E_T^{el} in the lowest-mass sample is basically smaller than 25 GeV, whereas for $M_{e^*} = 300$ GeV values of up to 150 GeV are attained.

In the $e^* \to eq\bar{q}$ channel, the background arises almost exclusively from NC DIS events. The preselection requires an electron to be identified (Sect. 5.4.2). Moreover, a set of cuts is applied involving the above-mentioned quantities, as well as the longitudinal energy-momentum variable, δ. Those requirements are relatively loose, so that a large number of events is still present at the preselection level (Table 5.5). The numerical agreement between the experimental data and the expected background is acceptable. Except for the data overshooting the MC at high values of δ, the shapes of the observed distributions are well reproduced by the simulation (Fig. 5.13).

The preselection variables are employed for the final event selection as well. In addition, the variables $M_{\mathrm{had}}/E_T^{\mathrm{had}}$ and $M_{\mathrm{tot}}/M_{\mathrm{rec}}$ are used. The signal distributions of the latter quantity exhibit a marked peak (Fig. 5.12), rendering it useful for rejecting backgrounds. Similarly, the variable $M_{\mathrm{had}}/E_T^{\mathrm{had}}$ helps to distinguish between the signal topology and NC events, since the respective signal values tend to cluster around $M_{\mathrm{had}}/E_T^{\mathrm{had}} \approx 1$.

As for the cut approach, the selection requirements are considerably stricter than the preselection cuts. This leads to drastically decreased event numbers compared to the preselection stage. The final event numbers obtained with the probability method are

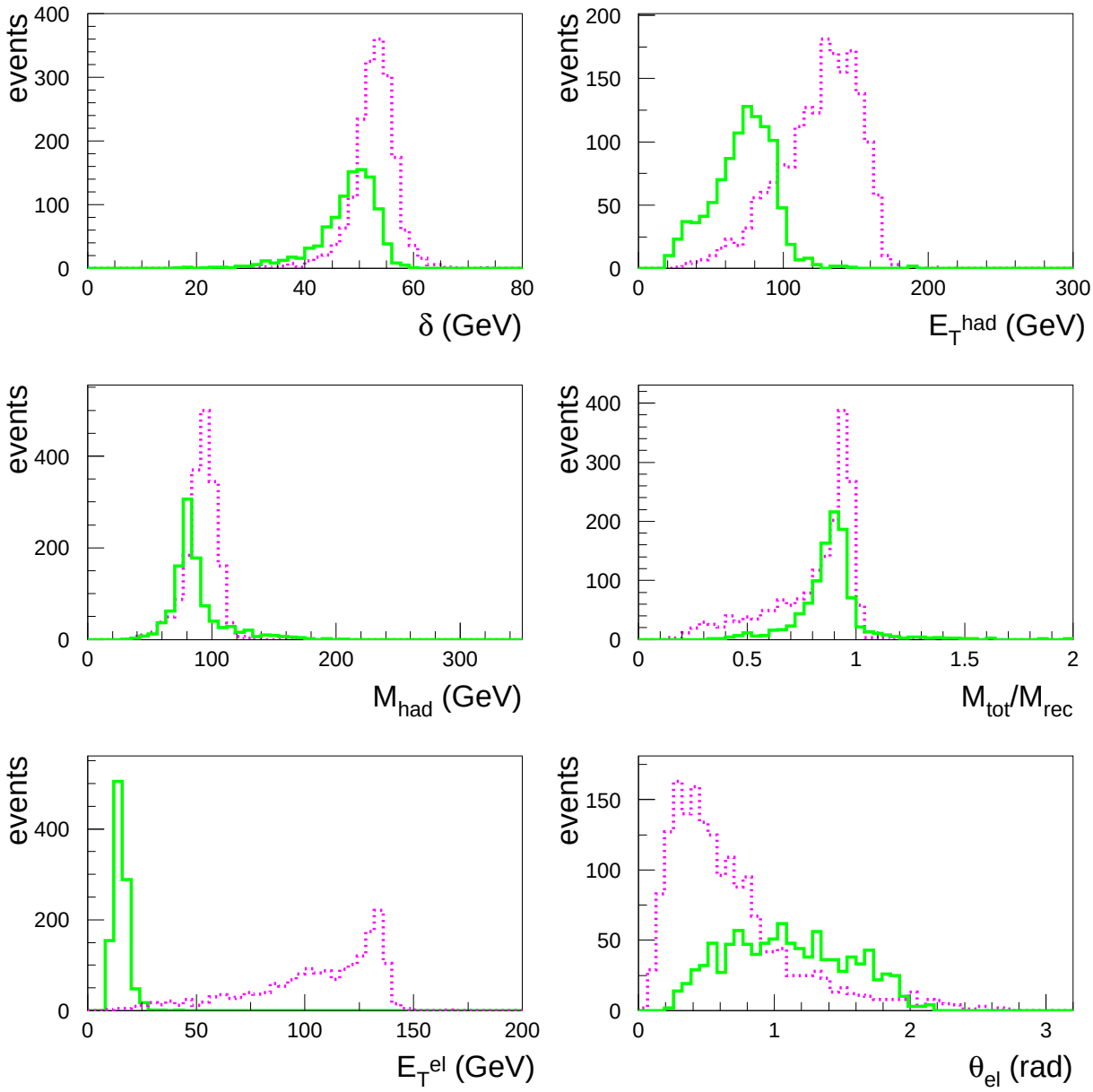

Figure 5.12: *Signal distributions of the key variables in* $e^* \rightarrow eq\bar{q}$. *The solid-line histograms represent the* $M_{e^*} = 110\ GeV$ *sample, whereas the dotted distributions display a mass of* $300\ GeV$.

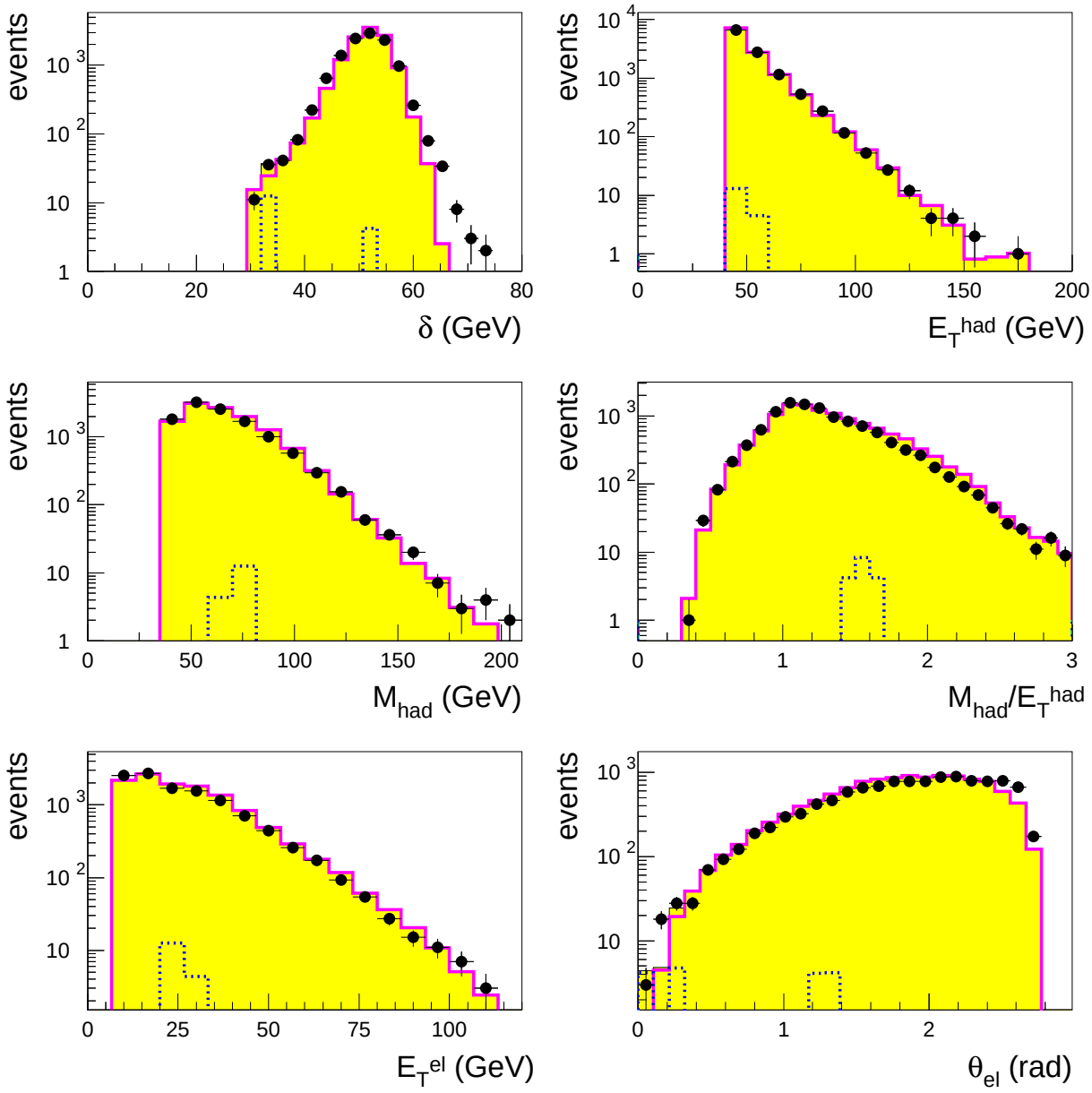

Figure 5.13: *Comparison plots between the data (dots) and the background simulation (filled histogram) at the preselection level. Neutral-current DIS events (solid contour) constitute almost the entire background; additionally, there is a small contribution from PHP events (dotted contour).*

$e^* \to eZ \to eq\bar{q}$ preselection cuts	
E_T^{el}	$> 10\,\text{GeV}$
θ_{el}	$< 3.0\,\text{rad}$
δ	$\in (30, 75)\,\text{GeV}$
E_T^{had}	$> 40\,\text{GeV}$
M_{had}	$> 40\,\text{GeV}$

event numbers	
observed:	**11467**
98/99:	2425
99/00:	9042
expected:	**12034 ± 67**
NC DIS:	12016
PHP res.	16.5

M_{e^*} [GeV]	eff. [%]	M_{e^*} [GeV]	eff. [%]
110	44.1	225	84.8
125	62.3	250	86.2
150	74.2	275	86.6
175	80.3	300	88.4
200	83.2	310	86.7

Table 5.5: *Preselection cuts, resulting event numbers and efficiencies. The low-mass efficiencies suffer somewhat from the E_T^{el} cut.*

even smaller by about a factor of 2.5 (Table 5.6). In this channel the probability approach yields substantially stronger expected limits than the fixed cuts (Fig. 5.14). To obtain the final results, a probability cut of $P'_{\text{tot}} > 0.50$ has been adopted. The efficiencies and mass resolutions are depicted in Sect. 5.6.8. The mass shifts obtained are pleasantly small.

With neither of the two selection approaches, any excess is observed in the data events. The respective mass spectra are shown in Sect. 5.6.9. It is interesting to note that the mass spectrum of the cut selection contains a cluster of three candidate events with masses of about 295 GeV, where the expectation has almost dropped to zero. Consequently, the statistical test reveals the most prominent probability peak among all spectra tested. However, the alternative search approach selects only one of those three events.

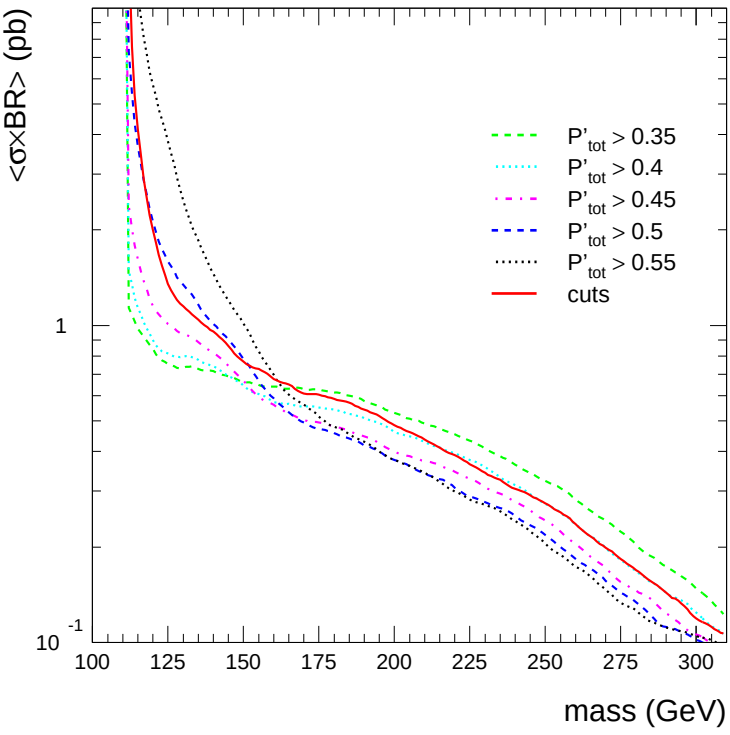

Figure 5.14: *Expected limits on $\sigma \times$ BR for the fixed cuts (solid curve) and for the probability approach with different cuts on P'_{tot}. The curve corresponding to $P'_{\text{tot}} > 0.50$ is considered the most promising choice.*

fixed cuts (A)	
E_T^{el}	$> 25\,\text{GeV}$
θ_{el}	$< 1.6\,\text{rad}$
δ	$\in (45, 60)\,\text{GeV}$
E_T^{had}	$> 80\,\text{GeV}$
M_{had}	$> 75\,\text{GeV}$
$M_{\text{had}}/E_T^{\text{had}}$	$\in (0.5, 1.5)$
$M_{\text{tot}}/M_{\text{rec}}$	> 0.5

final event numbers		
	A	B
observed:	**116** $(26 + 90)$	**43** $(14 + 29)$
expected:	$\mathbf{124.8 \pm 3.4}$	$\mathbf{51.2 \pm 1.7}$
NC DIS:	124.7	51.2

$\boldsymbol{e^* \to eZ \to eq\bar{q}}$

M_{e^*} [GeV]	efficiency [%] A	efficiency [%] B	resol. [GeV]	shift [GeV]
110	0.2	0.6	6.8	3.8
125	10.8	6.7	4.6	0.2
150	31.5	19.4	6.3	−0.3
175	40.8	30.8	6.4	−0.4
200	51.5	44.8	8.0	−0.3
225	58.8	52.5	8.9	−0.8
250	62.1	56.2	11.2	−0.9
275	66.1	59.0	12.4	−1.1
300	68.2	62.1	14.3	−1.7
310	67.1	60.8	14.0	−1.9

Table 5.6: *Results of the $e^* \to eq\bar{q}$ search. For the probability approach (B), again the same variables as listed for the cut selection (A) have been used. Graphical representations of the efficiencies, resolutions and mass spectra can be found in Sects. 5.6.8 and 5.6.9, respectively. The numbers of events observed during the 98/99 and 99/00 data taking are listed separately in brackets.*

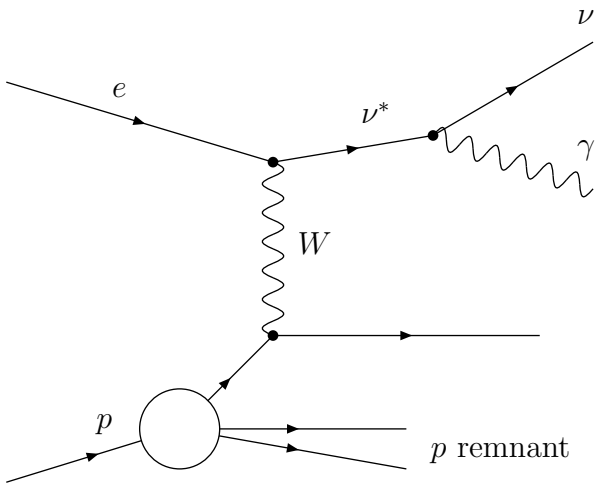

Figure 5.15: *Feynman diagram for excited-neutrino production with subsequent photonic decay, $\nu^* \to \nu\gamma$.*

5.6.5 $\nu^* \to \nu\gamma$

A photon coupling to a neutrino (Fig. 5.15) seems odd at first sight. However, if the excited neutrino contains electrically charged constituents, the photonic decay becomes imaginable. The signature of the $\nu\gamma$ final state consists in one isolated electromagnetic cluster without matching track and, additionally, a large amount of missing transverse momentum (Fig. 5.16). Owing to the W exchange, ν^* production proceeds inelastically. The hadronic jet from the struck parton, however, is strongly boosted forward, so that the hadronic activity observed can be small nonetheless. That holds particularly for the higher ν^* masses studied.

The preselection puts up CAL timing constraints and requires a photon to be found (Sect. 5.4.2). The latter criterion includes an explicit track veto inside the CTD accep-

$\nu^* \to \nu\gamma$ preselection cuts	
$\not{P}_T$	$> 12\,\text{GeV}$
δ	$< 65\,\text{GeV}$
E_T^γ	$> 12\,\text{GeV}$

event numbers	
observed:	**82**
98:	20
99:	62
expected:	**80.0 ± 6.1**
NC DIS:	44.0
CC DIS:	4.8
PHP:	31.1

M_{ν^*} [GeV]	eff. [%]	M_{ν^*} [GeV]	eff. [%]
100	53.3	225	53.9
125	54.2	250	52.6
150	55.4	275	50.8
175	58.5	300	43.2
200	54.8	310	40.6

Table 5.7: *Preselection cuts, resulting numbers of data and MC events and signal efficiencies. For the number of observed events, the contributions from the 98 and 99 e^-p running are listed separately.*

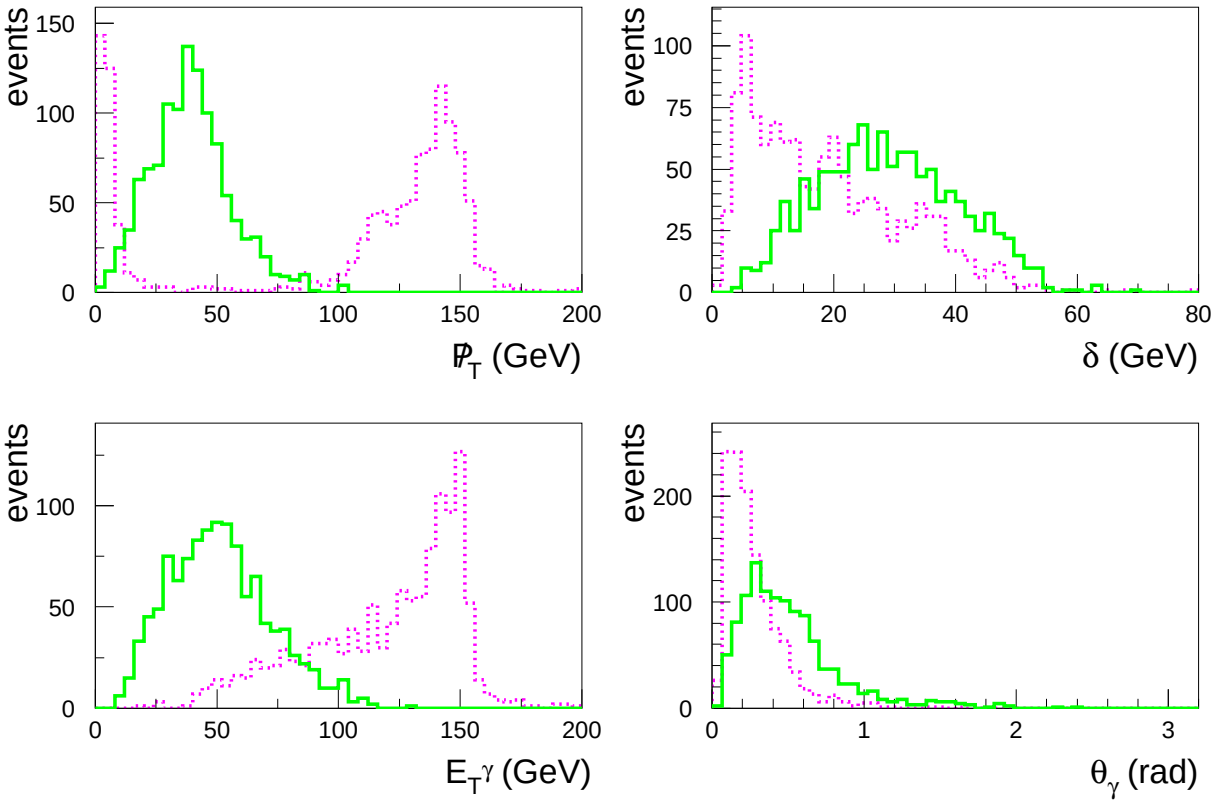

Figure 5.16: *Distributions of some key quantities in the $\nu^* \to \nu\gamma$ signal MC; the masses of the samples displayed are 100 GeV (solid line) and 300 GeV (dotted line), respectively. The fraction of high-mass events with apparently low $\not\!\!P_T$ contains a photon which hits the FCAL first inner ring; without any hadronic activity present, the value of $\not\!\!P_T$ turns out to be almost zero, since it excludes the first inner ring (Sect. 4.2.2).*

tance. In addition, a set of relatively loose cuts on $\not\!\!P_T$, δ and E_T^γ is applied, as summarised in Table 5.7. Yet the signature required (photon plus $\not\!\!P_T$) is rare, so that after the preselection only 82 data events are left, which agrees well with the expectation. An obvious background process is constituted by CC DIS events, either containing an isolated π^0 decay or radiative ones. The largest fraction of the background at this stage, though, arises from NC and PHP reactions. Considerable amounts of $\not\!\!P_T$ in these types of events are likely to be caused by energy leakage out of the CAL or by resolution effects.

As depicted in Fig. 5.17, the NC background can be effectively reduced by a further constraint on the polar angle of the final-state photon, which emerges predominantly in the rear direction. Those are likely to be electrons with non-identified tracks or ISR photons. The PHP background, on the other hand, is likely to contain photons from π^0 decays. Those are, according to Fig. 5.17, concentrated in the very forward region. Here the data-MC agreement is not satisfactory, which is however a known feature of the

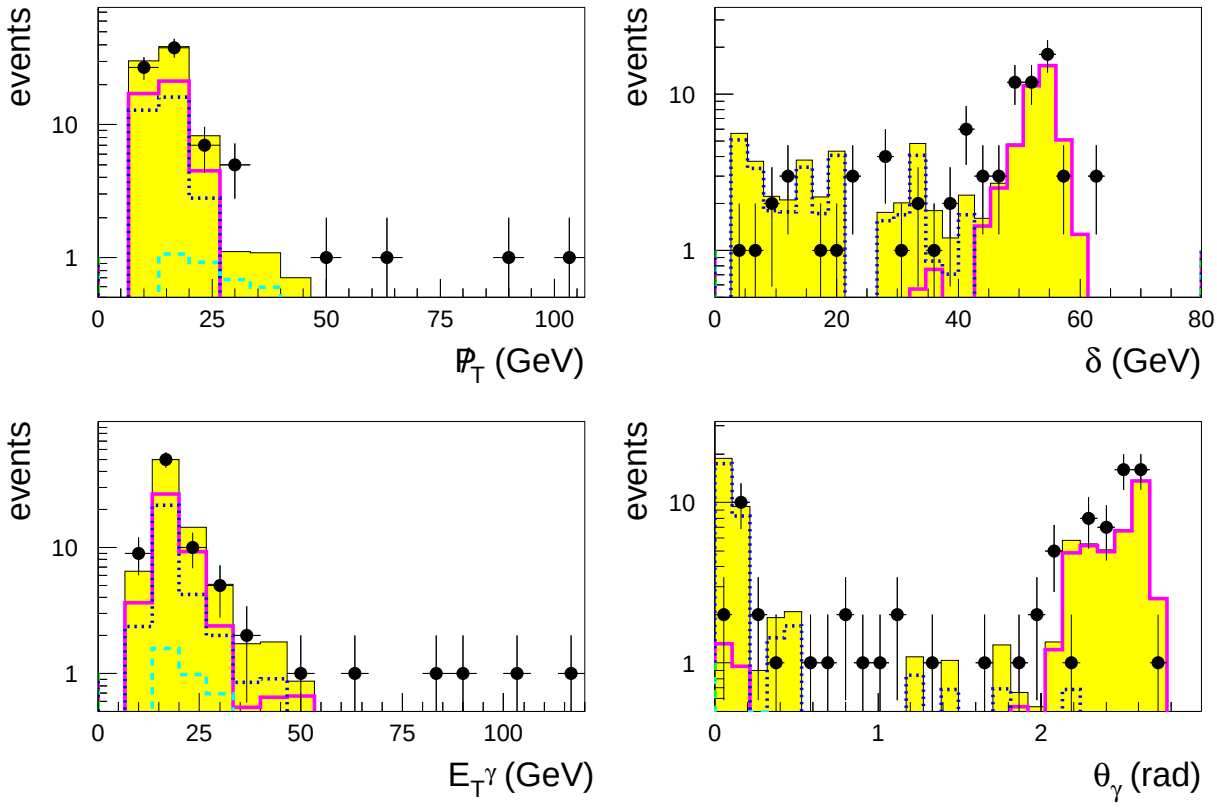

Figure 5.17: *Control plots to check the data-MC normalisation at the preselection level. The dots with error bars represent the experimental data; the filled histogram is the total expected background, which contains contributions from NC DIS (solid contour), photoproduction (dotted contour) and CC DIS (dashed contour).*

ZEUS detector simulation. Both the NC and PHP backgrounds are sensitive to stricter constraints on $\not{P}_T$, since they typically feature values below 25 GeV.

As for the final event selection, the numbers of events surviving are the smallest of all channels analysed (Table 5.8). This holds for both selection approaches. The two candidate events from the 1998 data taking are identically selected by both approaches. The probability method yields no substantial gain in terms of stronger expected limits in this channel, as displayed in Fig. 5.18. The outcome of the search is summarised in Table 5.8. The efficiencies and mass resolutions as well as examples of the mass reconstruction are depicted in Sect. 5.6.8. The mass spectra and the accompanying statistical tests are plotted in Sect. 5.6.9.

No excess of events is observed in the data.

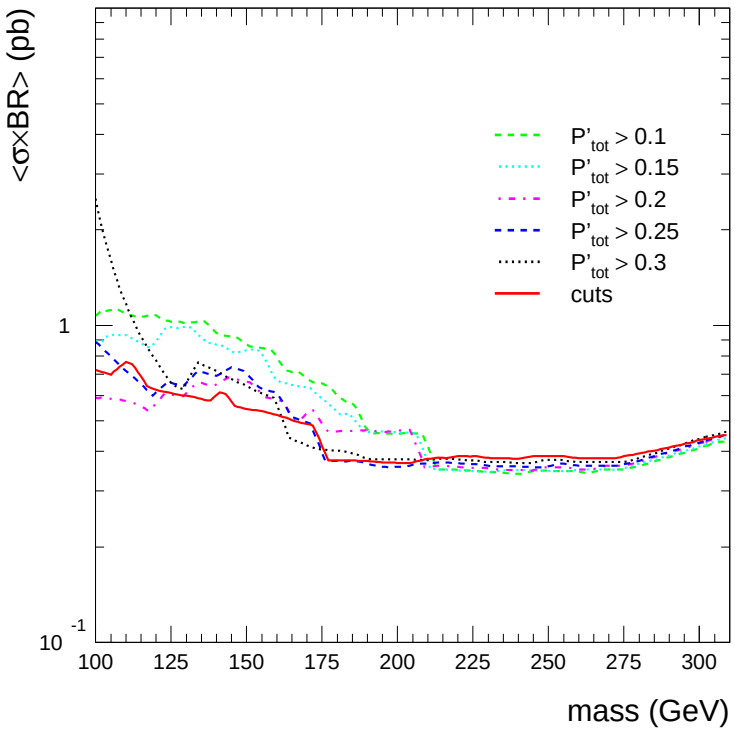

Figure 5.18: *Expected limits on $\sigma \times$ BR for both selection approaches: The solid curve represents the fixed cuts, whereas the other curves incorporate the expected limits obtained with the probability approach when using different cuts on P'_{tot}. The curve corresponding to $P'_{\mathrm{tot}} > 0.25$ has been used for the further analysis. Above 210 GeV the curves hardly differ because in either case there is essentially no background expected at such high masses.*

fixed cuts (A)	
$\not\!\!P_T$	$> 20\,\mathrm{GeV}$
δ	$< 45\,\mathrm{GeV}$
E_T^γ	$> 20\,\mathrm{GeV}$
θ_γ	$< 0.8\,\mathrm{rad}$

final event numbers		
	A	B
observed:	**3** $(2+1)$	**3** $(2+1)$
expected:	$\mathbf{4.1 \pm 1.5}$	$\mathbf{3.3 \pm 1.4}$
NC DIS:	0.3	0.1
CC DIS:	1.3	0.8
PHP:	2.5	2.4

$\boldsymbol{\nu^* \longrightarrow \nu\gamma}$

M_{ν^*} [GeV]	efficiency [%] A	efficiency [%] B	resol. [GeV]	shift [GeV]
100	37.4	23.5	7.7	6.5
125	44.0	38.9	7.4	4.5
150	48.6	45.5	7.1	3.2
175	52.3	51.9	7.6	2.5
200	50.1	50.9	8.5	1.1
225	47.4	50.7	9.8	0.5
250	46.6	49.5	12.2	−2.0
275	45.6	48.3	11.5	−1.7
300	40.6	41.2	12.1	−0.6
310	38.5	38.5	13.6	−2.0

Table 5.8: *Numerical results of the $\nu^* \longrightarrow \nu\gamma$ search using the cut selection (A) and the probability method (B), respectively. The search has been performed in the 98/99 e^-p data. The separate numbers of events observed in either of the two years are stated in brackets.*

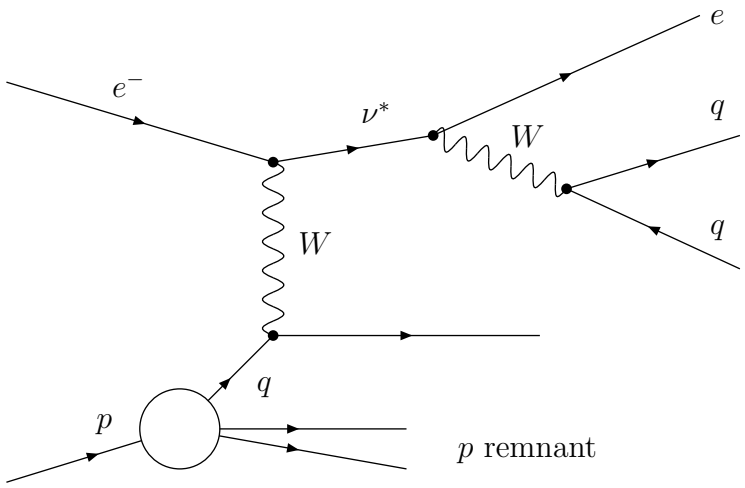

Figure 5.19: *Feynman diagram for excited-neutrino production with the subsequent decay $\nu^* \to eW \to eq\bar{q}'$.*

5.6.6 $\nu^* \to eW \to eq\bar{q}'$

The basic features of the "electron plus quarks" final state in ν^* decays are identical to those of the respective final state in e^* decays (Sect. 5.6.4). Some difference is introduced by the gauge-boson decay giving rise to the hadronic content. What distinguishes the two cases more significantly, however, are the gauge bosons involved in the production rather than in the decay of the excited leptons. In contrast to e^* production, excited neutrinos are produced by W exchange which proceeds inelastically. For that reason, in the ν^* case additional hadronic activity is likely to be present in the final state under study. As a result, the invariant hadronic mass, M_{had}, is expected to deviate stronger from the mass value of the gauge boson involved. As can be seen from Fig. 5.20, this affects predominantly the low-mass samples; in case of higher ν^* masses, the parton jet exhibits a stronger forward boost and is thus less likely to deposit energy in the detector. Any additional hadronic activity affects as well the mass reconstruction. Consequently, the resolution obtained for $\nu^* \to eq\bar{q}'$ is worse than for $e^* \to eq\bar{q}$ (Sect. 5.6.8).

$\boldsymbol{\nu^* \to eW \to eq\bar{q}'}$ preselection cuts	
E_T^{el}	$> 10\,\mathrm{GeV}$
θ_{el}	$< 3.0\,\mathrm{rad}$
δ	$\in (25, 75)\,\mathrm{GeV}$
E_T^{had}	$> 50\,\mathrm{GeV}$
M_{had}	$> 50\,\mathrm{GeV}$

event numbers	
observed:	**916**
98:	263
99:	653
expected:	$\mathbf{963 \pm 11}$
NC DIS:	962
PHP res.	1

M_{ν^*} [GeV]	eff. [%]	M_{ν^*} [GeV]	eff. [%]
100	35.2	225	72.8
125	58.2	250	74.1
150	61.0	275	77.2
175	66.1	300	79.5
200	69.6	310	83.6

Table 5.9: *Preselection overview comprising cuts, event numbers and signal efficiencies.*

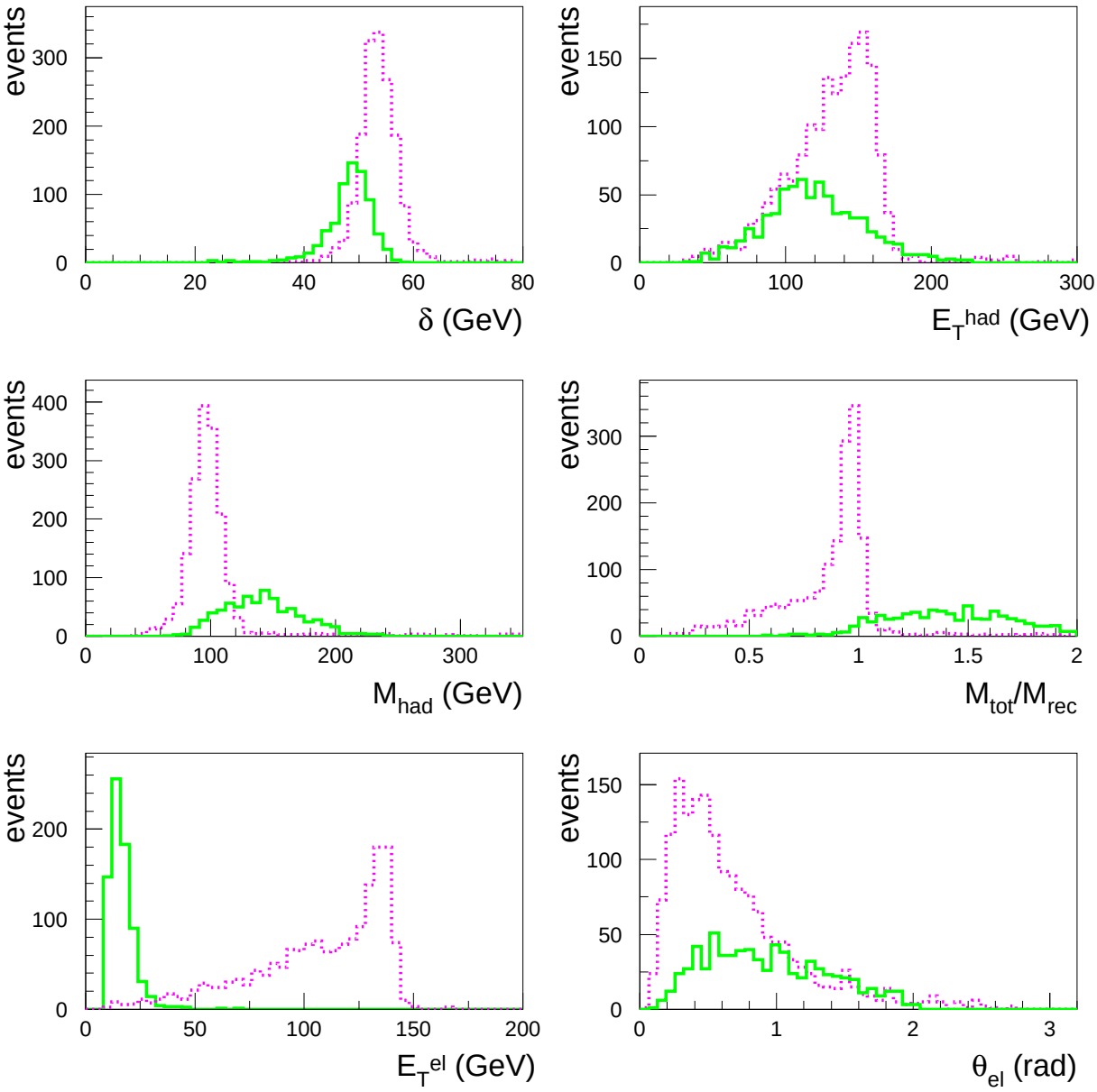

Figure 5.20: *Key distributions of the $\nu^* \to eq\bar{q}'$ signal MC samples. Shown here are the samples with masses of 100 GeV (solid line) and 300 GeV (dotted line), respectively.*

The preselection (Table 5.9) is similar to the one employed for $e^* \to eq\bar{q}$. For the channel studied here, the requirements imposed on the hadronic variables are somewhat tighter, though. Together with the smaller amount of data analysed, this leads to absolute event numbers which are lower by more than a factor of ten. Good numerical and qualitative agreement between the data and the background simulation is observed at the preselection level (Fig. 5.21).

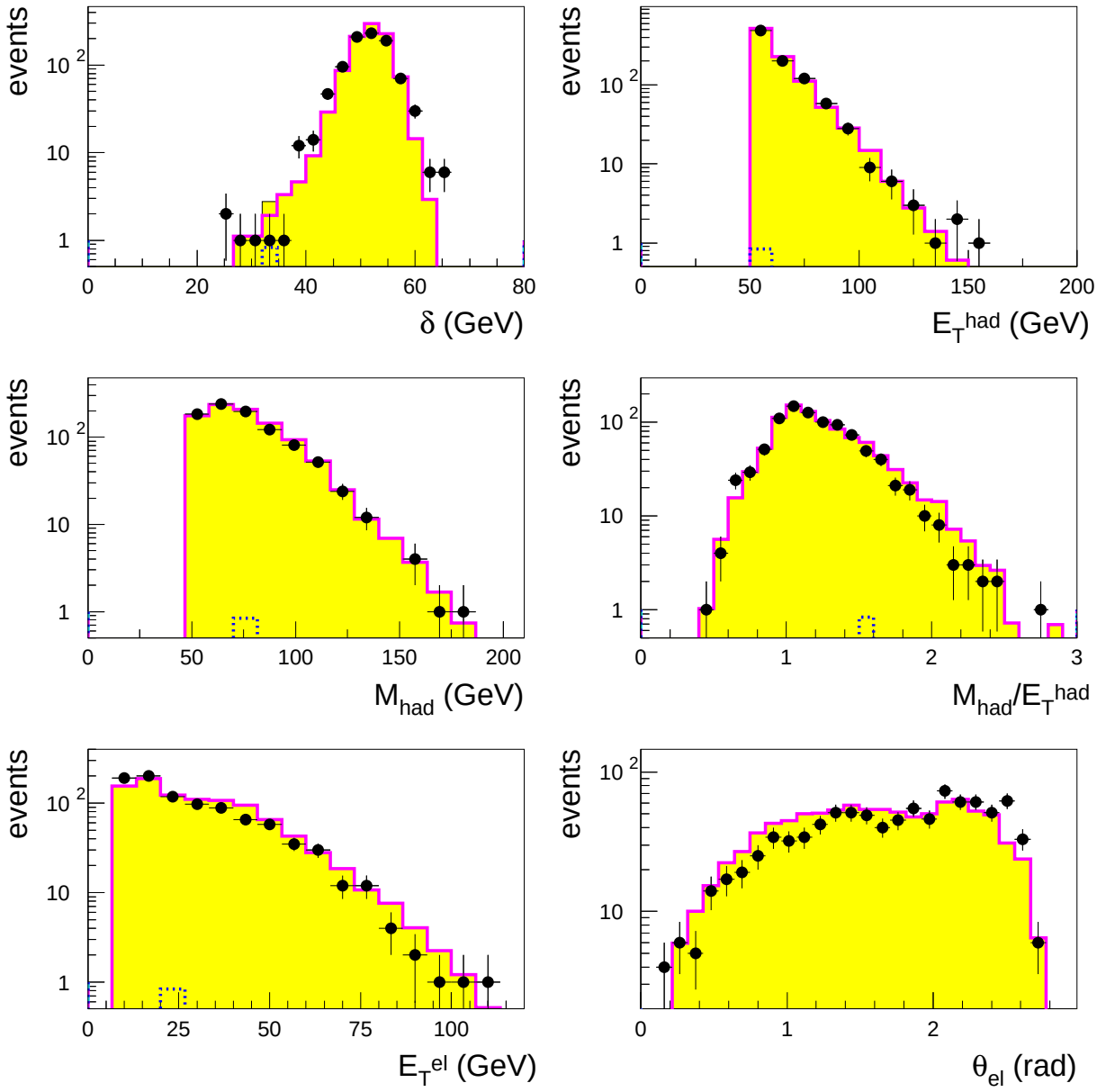

Figure 5.21: *Data-MC comparison plots at the preselection stage. The total background (filled histogram) arises almost exclusively from NC DIS events (solid contour). A small contribution from photoproduction is present (dotted contour).*

The outcome of the search using the two alternative event-selection approaches is summarised in Table 5.10. As in the $e^* \to eq\bar{q}$ case, $M_{\mathrm{had}}/E_T^{\mathrm{had}}$ and $M_{\mathrm{tot}}/M_{\mathrm{rec}}$ have been made use of in addition to the preselection variables. From Fig. 5.22 it can be seen that the probability approach yields stronger expected limits over the complete mass range studied. As for the numbers of candidate and background events obtained with either selection approach, a similar statement holds as in the $e^* \to eq\bar{q}$ case.

No indication of any excess of events is observed. The signal efficiencies and resolutions are depicted in Sect. 5.6.8. The mass spectra and the accompanying statistical tests are displayed in Sect. 5.6.9.

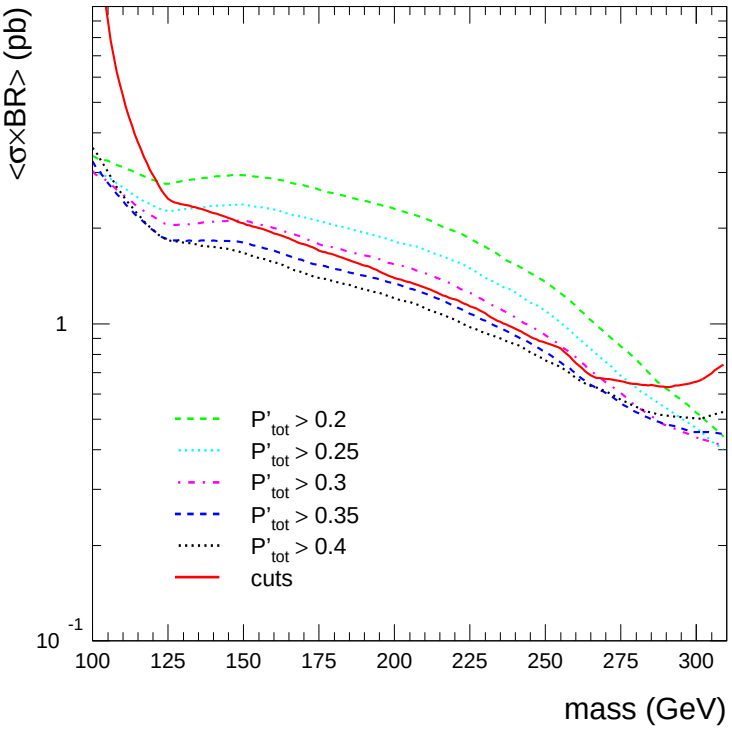

Figure 5.22: *Expected limits obtained with the fixed-cut approach (solid curve) and, alternatively, with the probability method; in the latter case, the line types indicate different cuts on the total probability. The value chosen is* $P'_{\text{tot}} > 0.40$.

fixed cuts (A)	
E_T^{el}	$> 25\,\text{GeV}$
θ_{el}	$< 2.0\,\text{rad}$
δ	$\in (35, 60)\,\text{GeV}$
E_T^{had}	$> 70\,\text{GeV}$
M_{had}	$> 85\,\text{GeV}$
$M_{\text{had}}/E_T^{\text{had}}$	$\in (0.5, 1.5)$
$M_{\text{tot}}/M_{\text{rec}}$	> 0.9

final event numbers		
	A	B
observed:	**17** $(3+14)$	**8** $(1+7)$
expected:	$\mathbf{25.2 \pm 1.1}$	$\mathbf{12.0 \pm 0.6}$
NC DIS:	25.2	12.0

$\boldsymbol{\nu^* \rightarrow eW \rightarrow eq\bar{q}'}$

M_{ν^*} [GeV]	efficiency [%] A	efficiency [%] B	resol. [GeV]	shift [GeV]
100	2.1	12.9	10.4	7.3
125	35.7	33.6	16.1	6.2
150	47.2	39.6	18.7	1.3
175	52.5	46.3	20.5	−0.3
200	54.8	50.8	20.9	−0.8
225	53.5	53.0	21.3	−3.0
250	51.8	53.7	19.6	−2.9
275	45.1	53.0	17.5	−3.6
300	40.0	53.0	15.2	−3.5
310	34.3	49.2	14.5	−3.2

Table 5.10: *Overview of the* $\nu^* \rightarrow eq\bar{q}'$ *search results, comprising the event selections based on fixed cuts (A) and on probabilities (B). The separate contributions of events observed in 98 and 99, respectively, are listed in brackets.*

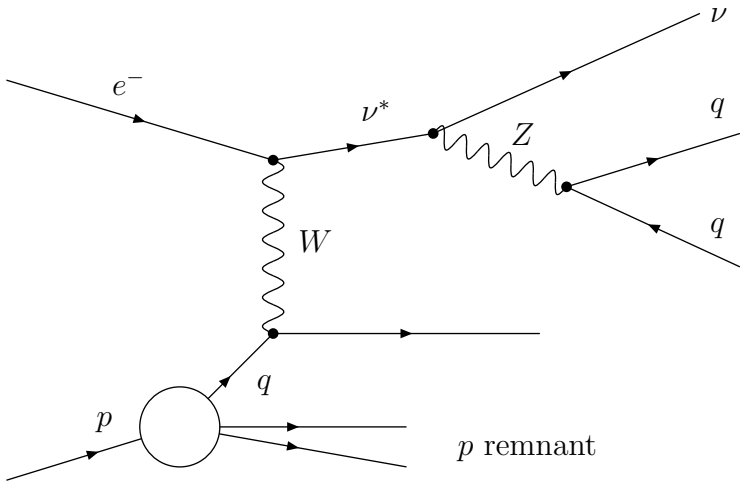

Figure 5.23: *Feynman diagram for $\nu^* \to \nu Z \to \nu q\bar{q}$.*

5.6.7 $\nu^* \to \nu Z \to \nu q\bar{q}$

What has been said about the comparison between $\nu^* \to eq\bar{q}'$ and $e^* \to eq\bar{q}$, is basically valid for the "neutrino plus quarks" final state in either e^* or ν^* decays as well. Again, the major differences are caused by the inelasticity of the ν^* events.

The preselection features CAL time constraints and a dedicated electron veto. As for the preselection cuts, the approach followed is somewhat different to the corresponding e^* case. A tighter cut on $\not{P}_T$ is applied here, whereas the $E_T^{\rm had}$ and $M_{\rm had}$ requirements are substantially softer. As a result, the photoproduction background is largely suppressed, so that CC DIS dominates more clearly than in the $e^* \to \nu q\bar{q}'$ case (Fig. 5.25). At this stage, the background simulation shows convincing agreement with the experimental data.

$\nu^* \to \nu Z \to \nu q\bar{q}$ preselection cuts	
$\not{P}_T$	$> 25\,\text{GeV}$
δ	$\in (10, 65)\,\text{GeV}$
$E_T^{\rm had}$	$> 20\,\text{GeV}$
$M_{\rm had}$	$> 20\,\text{GeV}$
$\#_{\rm trk}^{\rm vtx}/\#_{\rm trk}^{\rm tot}$	> 0.2

event numbers	
observed:	**318**
98:	85
99:	233
expected:	**313.6 ± 3.3**
NC DIS:	9.5
CC DIS:	298.5
PHP	5.7

M_{ν^*} [GeV]	eff. [%]	M_{ν^*} [GeV]	eff. [%]
110	8.3	225	70.9
125	31.4	250	70.9
150	62.2	275	71.5
175	70.0	300	66.3
200	74.2	310	63.6

Table 5.11: *Overview of the $\nu^* \to \nu q\bar{q}$ preselection. The signal efficiencies at the lowest masses are reduced mainly because of the $\not{P}_T$ cut.*

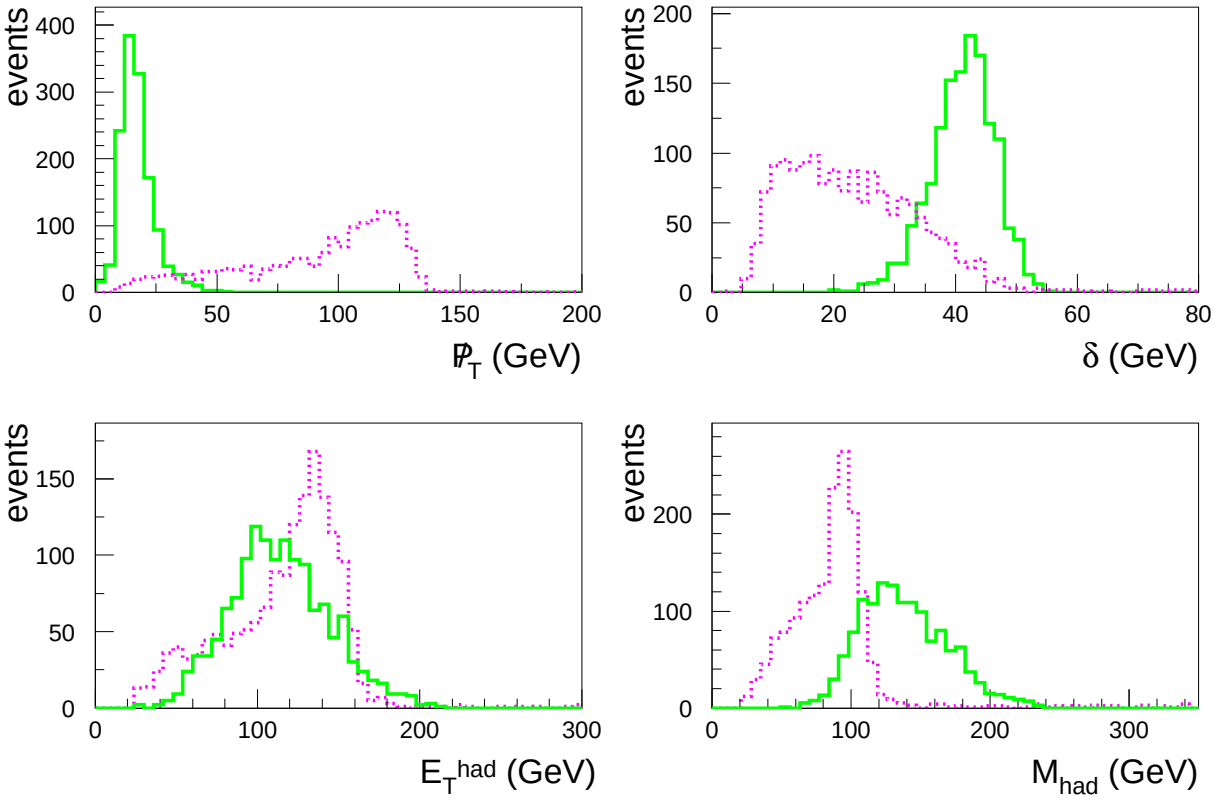

Figure 5.24: *Distributions of some key variables in the $\nu^* \to \nu q\bar{q}$ MC samples. The masses displayed are* 110 *GeV (solid line) and* 300 *GeV (dotted line).*

As can be seen from Fig. 5.26, the probability method yields stronger expected limits than the cut selection. The probability cut chosen to obtain the final results is $P'_{\text{tot}} > 0.40$.

With neither of the two alternative selection approaches an excess of events is observed in the experimental data. As for the mass reconstruction, the resolutions and shifts are comparable to those in the corresponding e^* channel. Graphical representations of the efficiencies, reconstructed masses and resolutions are given in Sect. 5.6.8. The mass spectra of the candidates and backgrounds are shown in Sect. 5.6.9.

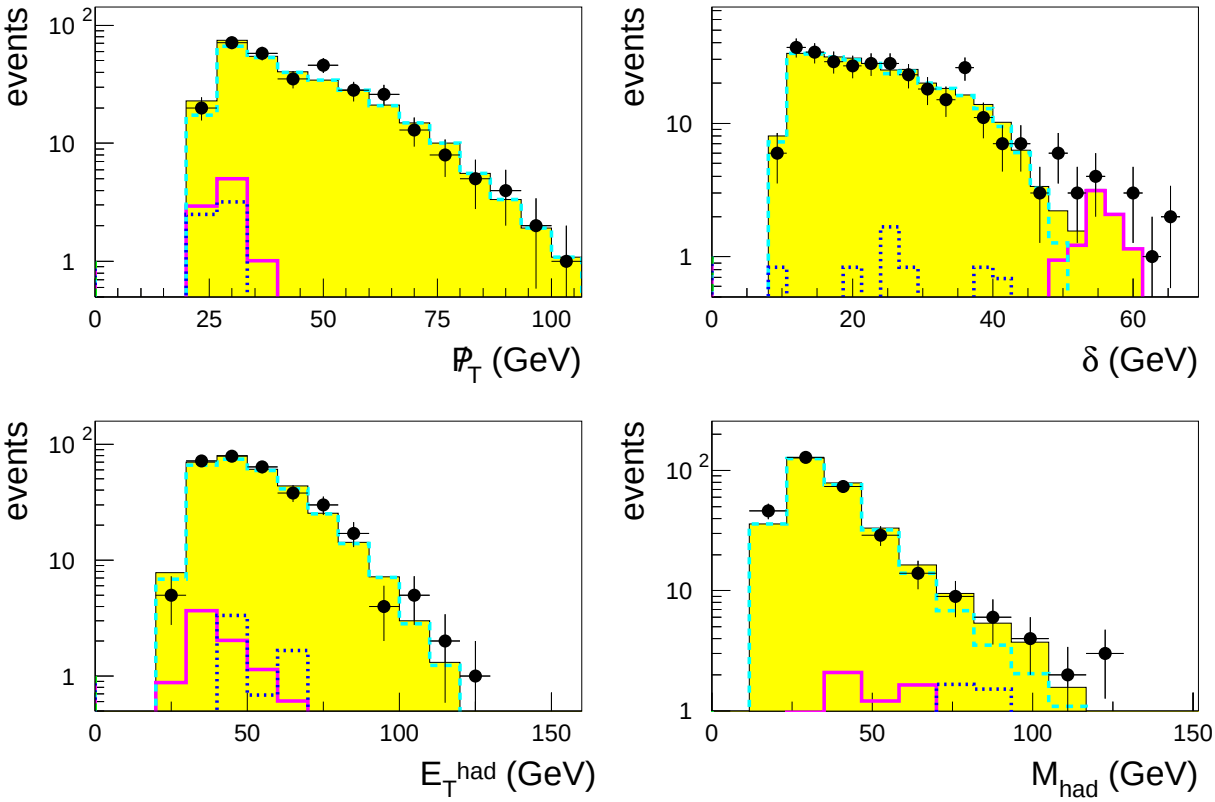

Figure 5.25: *Control plots for the $\nu^* \to \nu q\bar{q}$ preselection to check the agreement between the data (dots) and the background MC (filled histogram). The single background contributions are displayed as well: CC DIS (dashed contour), NC DIS (solid contour), PHP (dotted contour).*

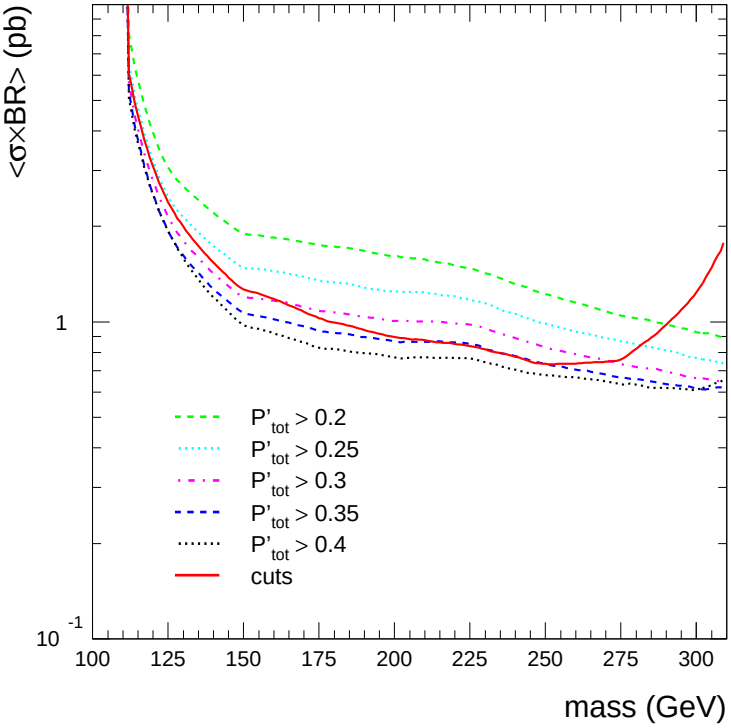

Figure 5.26: *Expected limits for $\nu^* \to \nu q\bar{q}$. The solid line represents the fixed-cut selection, whereas the other curves show the expected limits obtained with the probability approach using different cuts on the total probability. The cut value chosen for the further analysis is $P'_{\text{tot}} > 0.40$.*

fixed cuts (A)	
$\not{P}_T$	$> 25\,\text{GeV}$
δ	$\in (10, 50)\,\text{GeV}$
E_T^{had}	$> 50\,\text{GeV}$
M_{had}	$> 70\,\text{GeV}$
$M_{\text{had}}/E_T^{\text{had}}$	$\in (0.7, 1.4)$

final event numbers		
	A	B
observed:	**13** $(5+8)$	**5** $(2+3)$
expected:	$\mathbf{12.7 \pm 0.4}$	$\mathbf{4.93 \pm 0.24}$
NC DIS:	0.4	0.17
CC DIS:	12.3	4.75

$\boldsymbol{\nu^* \to \nu Z \to \nu q\bar{q}}$

M_{ν^*} [GeV]	efficiency [%] A	efficiency [%] B	resol. [GeV]	shift [GeV]
110	7.5	5.6	9.8	21.4
125	26.3	20.8	9.7	9.1
150	56.6	49.2	13.5	−3.1
175	65.3	58.5	15.3	−10.5
200	69.0	62.1	16.7	−17.6
225	62.8	56.2	18.0	−23.2
250	59.4	55.0	18.2	−26.5
275	51.2	51.8	20.4	−30.8
300	28.9	45.4	21.3	−32.4
310	19.5	40.1	21.7	−33.3

Table 5.12: *Results of the $\nu^* \to \nu q\bar{q}$ search. The numbers obtained with the cut selection are labelled by A, whereas B denotes the probability approach. Resolutions and mass shifts are stated for method B only. Given in brackets are the separate numbers of events observed in 98 and 99, respectively.*

5.6.8 Efficiencies and resolutions

In this section, graphical representations of the efficiencies and of the mass resolutions are shown for all six decay channels analysed. The curves plotted here correspond to the numbers listed in the preceding sections (overview tables of search results). Moreover, this section contains sample distributions of the reconstructed masses.

For a given signal MC sample, the efficiency is defined as the number of selected events divided by the total number of events generated. The latter is 2000 in all cases studied. In the preceding sections, efficiencies are stated both at the preselection level and after the final selection procedure. This section contains a graphical compilation of the signal efficiencies obtained after the event selection. The respective curves are displayed in Fig. 5.27, for the cut selection as well as for the probability approach.

The statistical uncertainty on the efficiency is given by $\sigma_\varepsilon = \pm\sqrt{\varepsilon(1-\varepsilon)/N}$, where ε and N denote the efficiency and the total number of events, respectively. For all efficiency values stated in the preceding sections, the absolute uncertainty is close to $\pm 1\,\%$. For the sake of clearness the individual errors have not been listed explicitly.

The signal efficiency is not only a figure of merit but attains relevance when calculating the exclusion limits. As described in Sect. 6.1, the upper limit on the e^* or ν^* cross section is inversely proportional to ε. The uncertainty on the efficiency has therefore been included as one of the systematic checks, which are discussed in Sect. 6.4.

The reconstructed-mass distributions are exemplified in Fig. 5.28. The respective plot contains for each channel the MC samples with nominal masses of 125 GeV, 200 GeV and 300 GeV. To estimate the corresponding mass resolutions, an obvious approach would consist in Gaussian fits. However, in several cases the distributions are found to exhibit rather non-Gaussian shapes. It has therefore been decided to employ the RMS value as a measure of the mass resolution instead. A similar argument holds for the mass shift, which has been determined by taking the difference of the respective histogram mean and the nominal mass value. These two quantities, mass resolution and shift, gain relevance for the calculation of the upper limits, as discussed in Sect. 6.1.

The resolution curves are plotted in Fig. 5.29. These numbers have been obtained from the signal MC samples after applying the probability-based event selection. Approximately identical values are achieved when applying the fixed-cut selection instead. The latter numbers are therefore not displayed separately.

Proceeding in steps of 1 GeV, the limit setting requires efficiency and resolution numbers for mass values that lie between the ten mass points available (Sect. 6.1). For that purpose, it has been preferred to interpolate linearly between the measured points, rather than use fitted parameterisations. For the latter do not provide improved accuracy but often entail nasty fine-tuning. The systematic uncertainty which is possibly induced by the efficiency interpolation is considered in the course of the systematic checks (Sect. 6.4). Concerning the mass resolution, the window size used in the limit setting is chosen wide enough as to account for possible uncertainties.

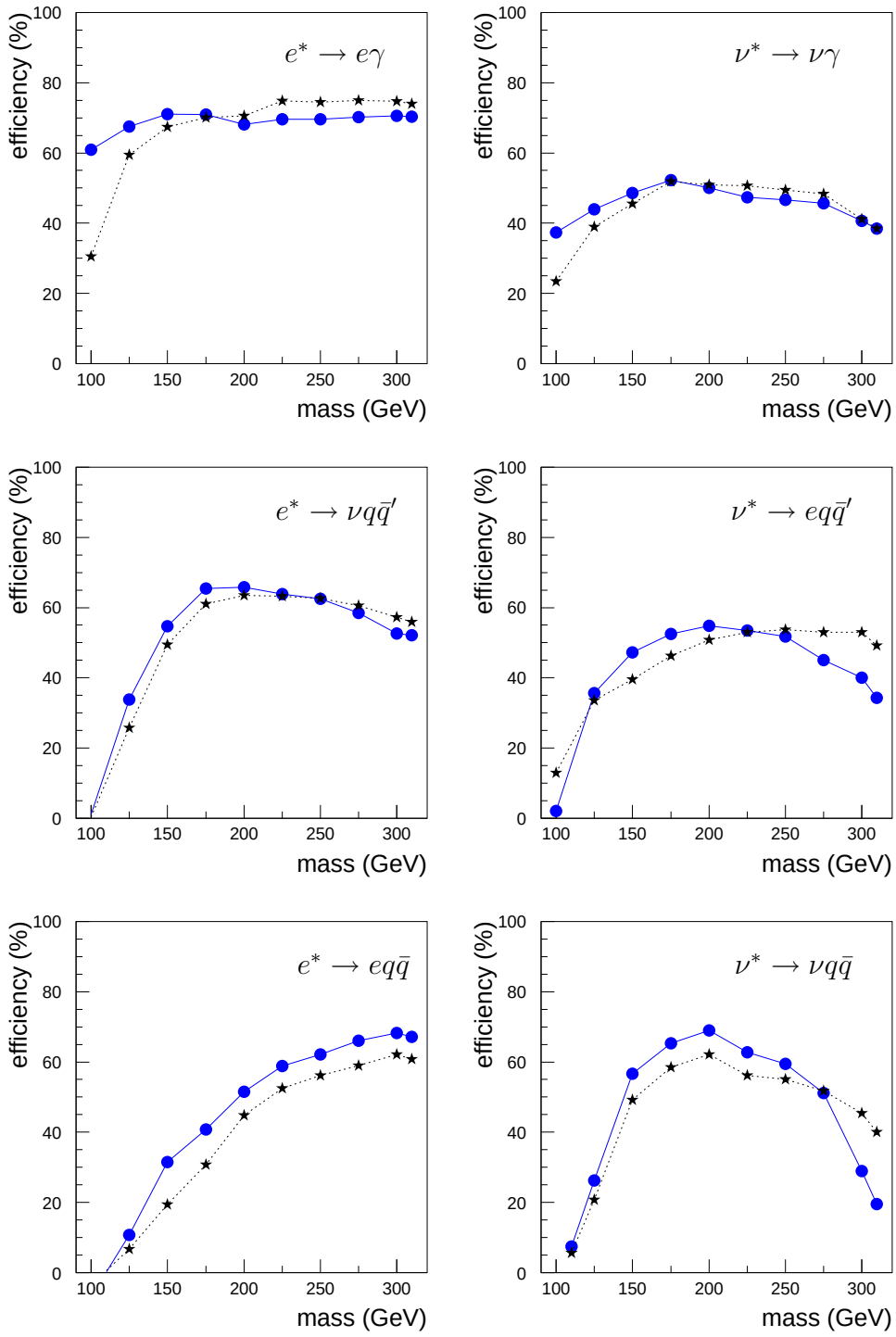

Figure 5.27: *Signal efficiencies after the final event selection for the six decay channels analysed. Plotted are the efficiencies obtained with fixed cuts (points and solid line) and, alternatively, with the probability method (stars and dotted line). In either case, the marker size exceeds the size of the error bars.*

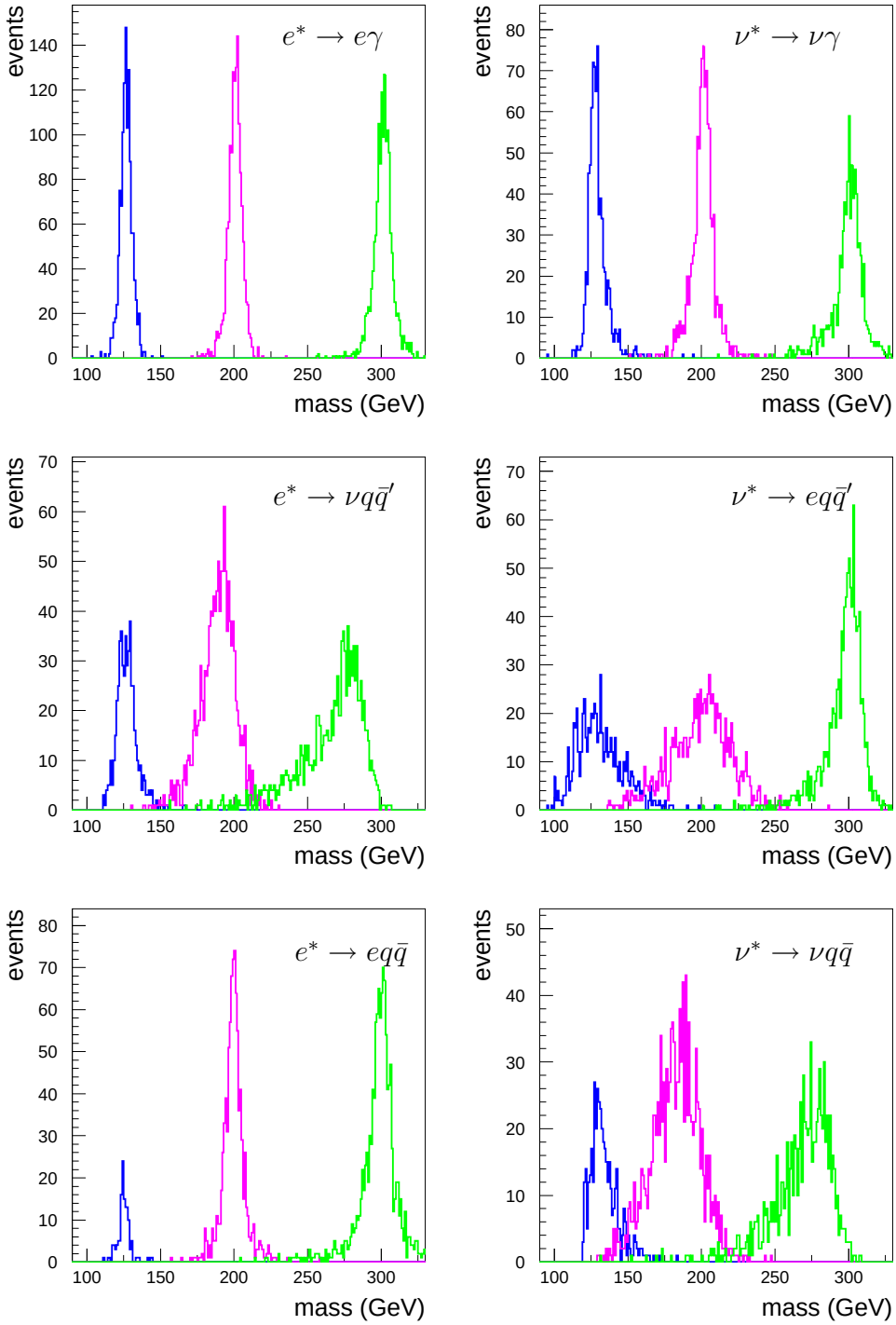

Figure 5.28: *Examples of the reconstructed-mass distributions. For each of the decay channels, the signal MC samples with nominal masses of* 125 *GeV*, 200 *GeV and* 300 *GeV are displayed. The masses have been reconstructed according to the formulae discussed in Sect. 4.3. Prior to generating these plots, the samples have been subjected to the event selection, so that the histograms may contain different numbers of entries.*

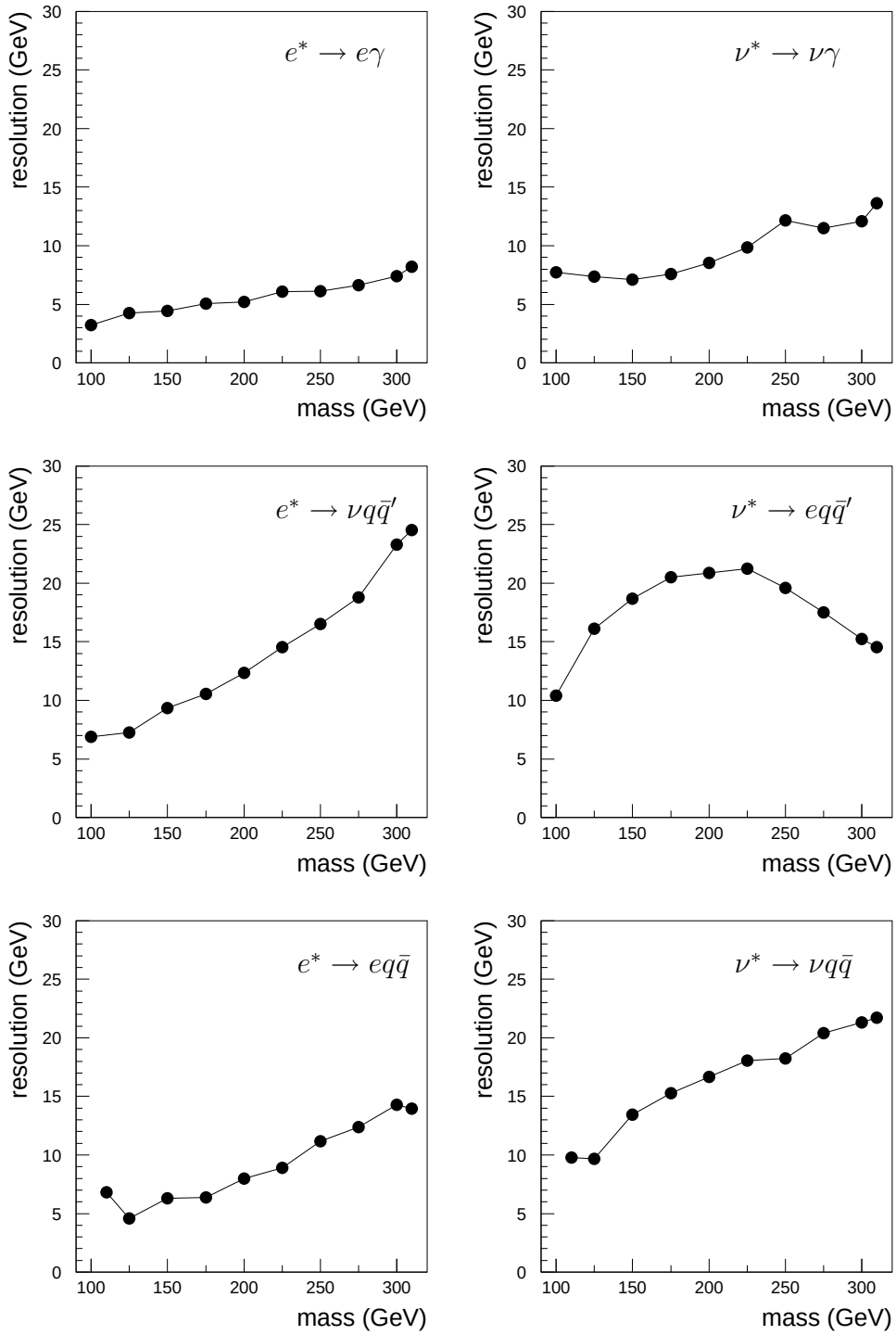

Figure 5.29: *Mass resolutions in the different decay channels. The RMS values of the reconstructed-mass distributions, examples of which are shown in Fig. 5.28, have been adopted as a measure of the resolutions. Plotted are the numbers according to the probability-based selection approach.*

5.6.9 Mass spectra

The invariant-mass spectra obtained with either of the two alternative selection methods are displayed in Fig. 5.30 for the e^* channels and in Fig. 5.31 for the ν^* channels.

Ideally, an excited-lepton signal would manifest itself as a clearly identifiable resonance peak in the mass spectrum, leading as well to a significant excess in the number of observed over the number of expected events. Obviously, that is not the case in either of the decay channels analysed. Yet it is desirable to provide more solid grounds for the statement of there being no evidence for any excited lepton. For that purpose, the mass spectra of the candidate and background events have been subjected to a statistical test.

The test applied involves a shifting mass-window scanning the relevant mass range in steps of 1 GeV. At each step the numbers of N candidate and b background events within the mass window are inquired. Then the Poisson probability to observe *at least* N events when b are expected is calculated, which means to compute the sum $1 - \sum_{n=0}^{N-1} P(n, b)$.

As for the width of the mass window, checks have been made with both fixed and variable widths, the latter depending on the respective mass resolution. The differences in the statistical conclusions due to the specific choices of mass windows have turned out to be insignificant. For the plots displaying the test results in Figs. 5.32 and 5.33 a fixed width of 10 GeV has been chosen.

In the above-mentioned plots the probability curves obtained are shown, with smaller values indicating that the respective event numbers are less likely to be observed. A hypothetical signal would manifest itself as peaking down to particularly small probabilities. For the claiming of a discovery to be taken seriously, it is conventional to require a signal to be observed at the 5σ-level. As the 5σ tails correspond to $\approx 10^{-4}\,\%$ of the area of a Gaussian peak, one may argue that 10^{-6} represents the level of probability that is expected to be obtained in case of a signal.

5.6.10 Conclusions

In all cases studied the numbers of observed and expected events are found to be in good agreement, bearing no indication of an excess anywhere in the mass spectra. There is indeed no evidence found for excited electrons or neutrinos in any of the decay channels which have been analysed.

Yet these findings do not allow to conclude that the sought-after signal does not exist. For it could in fact be there but too weak to be discovered under the experimental conditions given. The non-observation of a signal only allows to set an upper limit on the signal strength, i.e. on the production cross-section times the branching ratio of the excited lepton considered. Thus, exclusion limits at 95% confidence level on e^* and ν^* production have been derived. A description of the procedure employed and the limit curves obtained are presented in the next chapter.

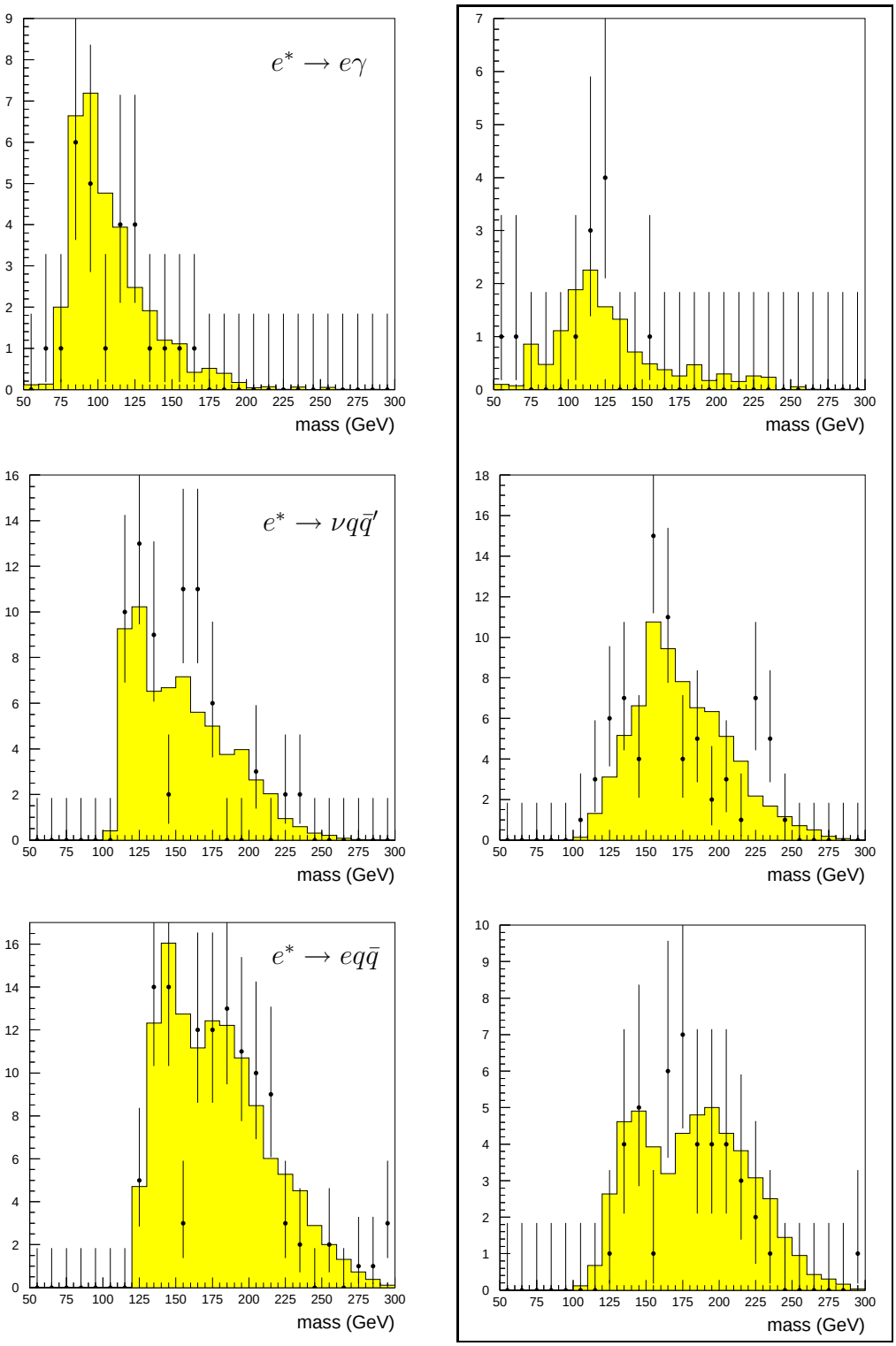

Figure 5.30: *Invariant-mass spectra of the observed candidates (points with error bars) and the expected background (filled histogram) for the excited-electron channels. The left column contains the outcome of the fixed-cut search; the right, framed column contains the corresponding spectra for the probability method.*

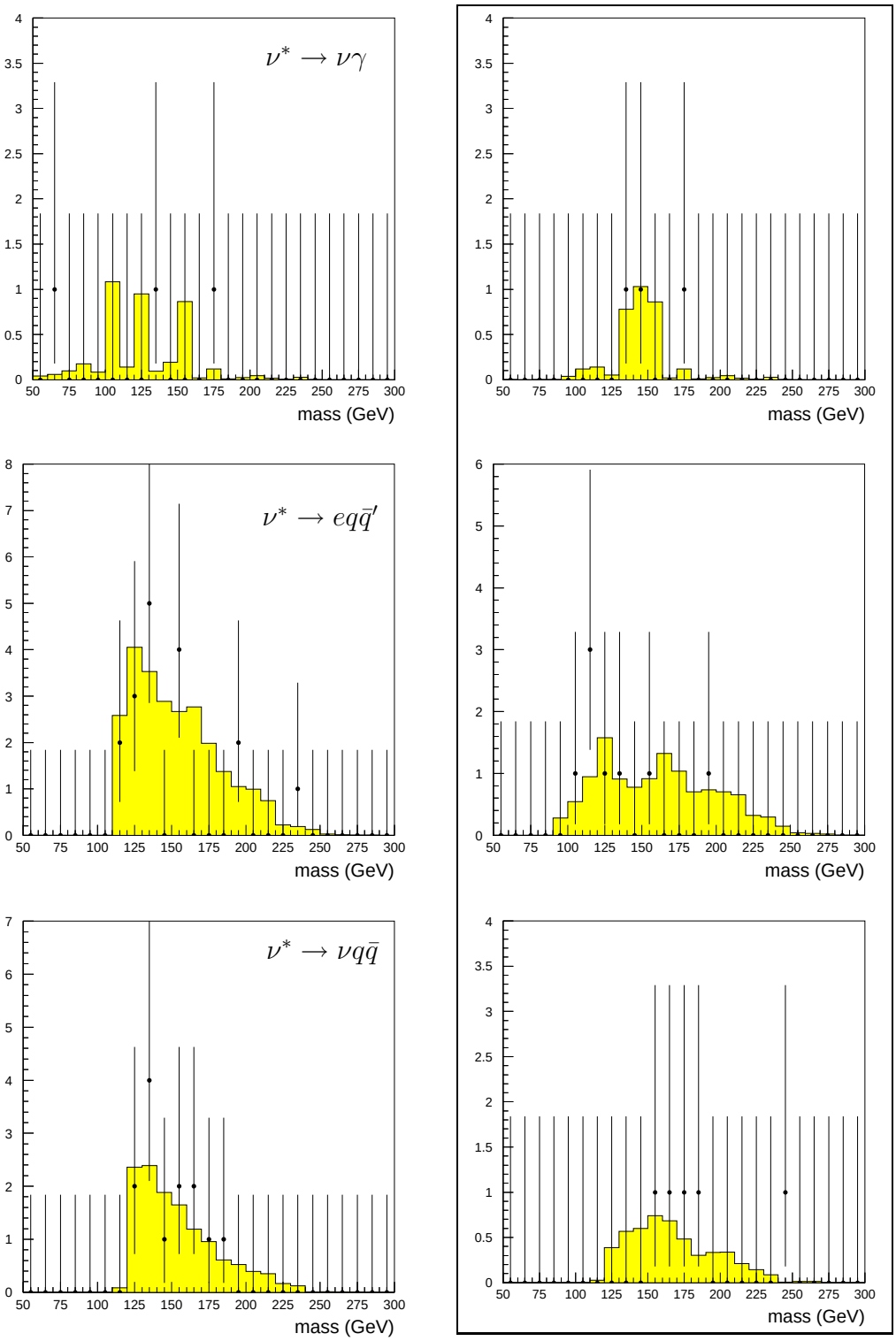

Figure 5.31: *Invariant-mass distributions of the events observed in the experimental data (points with error bars) and the expected background (filled histogram) for the excited-neutrino channels. The results obtained with the cut selection are presented in the left column, whereas the right column contains the corresponding mass spectra for the probability-based selection approach.*

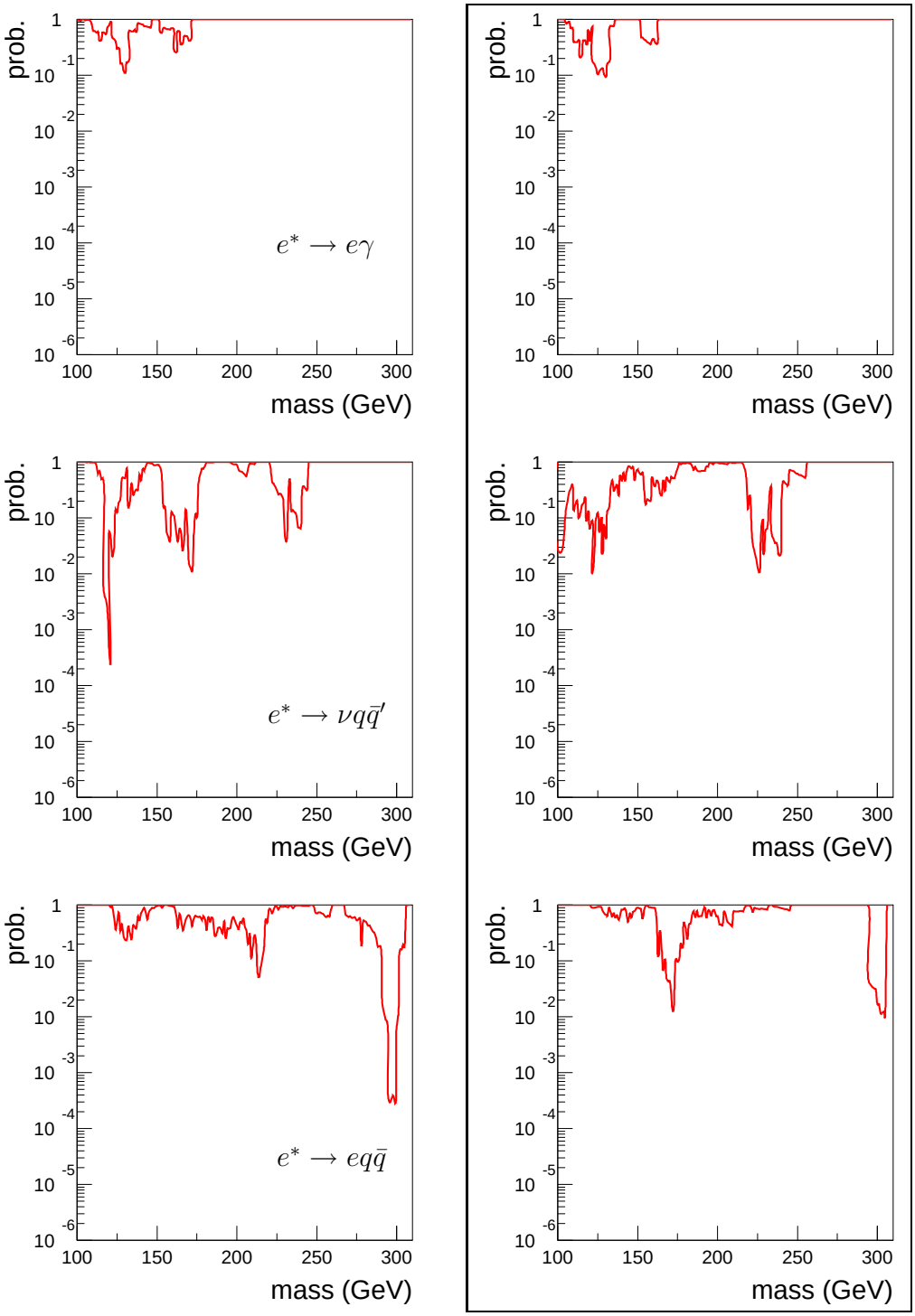

Figure 5.32: *Probability curves resulting from the statistical tests of the e^* invariant-mass spectra. The probabilities shown are connected with the distributions in Fig. 5.30. Left column: fixed cuts; right column: probability method.*

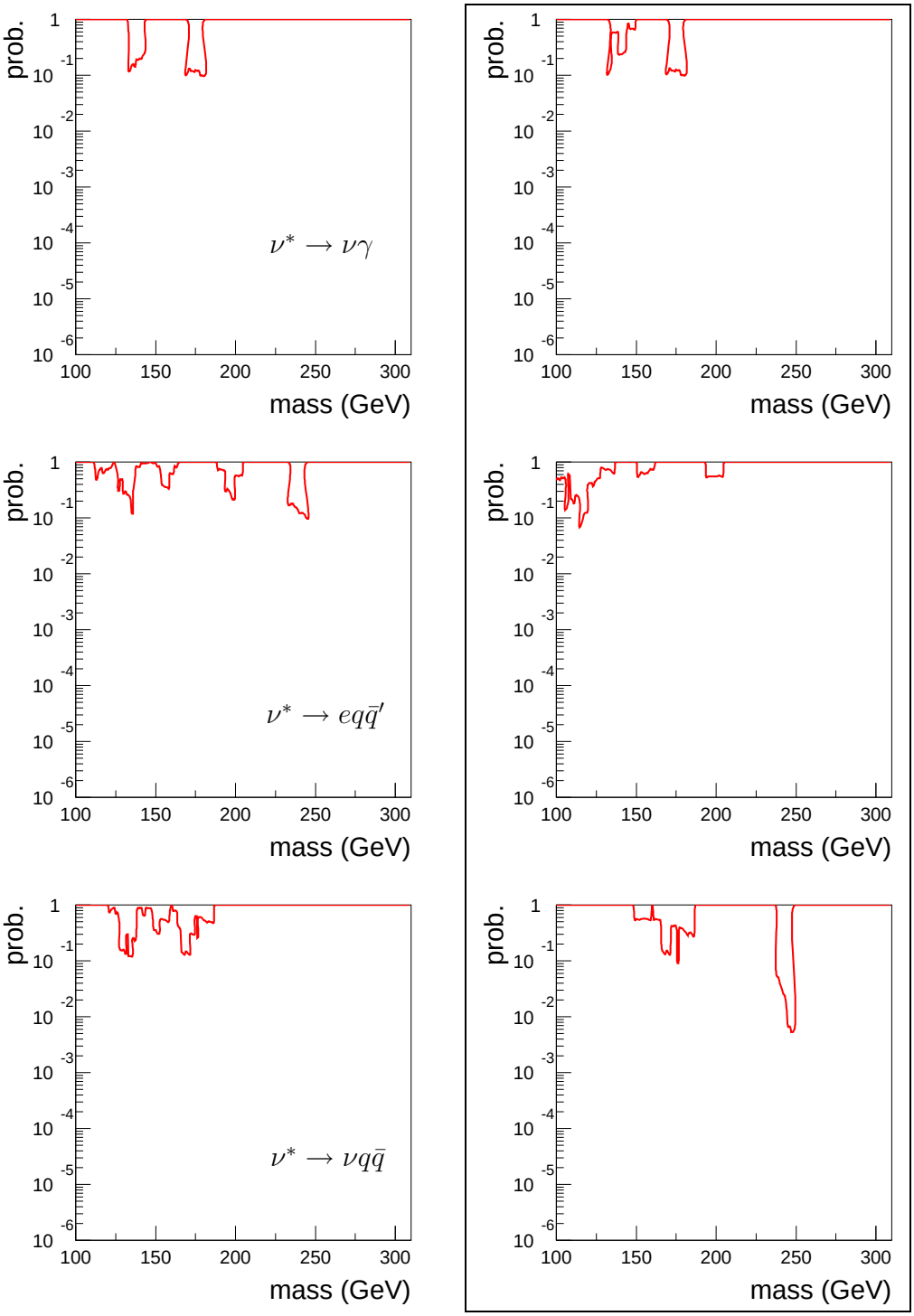

Figure 5.33: *Probability curves obtained with the statistical tests of the ν^* mass spectra. The plots are connected with the invariant-mass distributions in Fig. 5.31. Left column: cut selection; right column: probability method.*

Chapter 6

Results

6.1 The limit-setting procedure

In the absence of an excited-lepton signal in any of the decay channels analysed, upper limits can be set, for e^* and ν^*, on the production cross-section times the branching ratio, $\sigma \times \mathrm{BR}$. The only model-dependent information entering the calculation of these limits is the selection efficiency obtained from the signal MC. In addition, it is conventional to derive limits on the coupling over the compositeness scale, f/Λ, directly from the $\sigma \times \mathrm{BR}$ limits. This requires the production cross-section and the excited-lepton branching ratios as additional model-dependent input. While the $\sigma \times \mathrm{BR}$ limits are specific to *ep* collisions, the f/Λ limits can be compared to corresponding results from other particle colliders, for instance the LEP experiments.

The limit-setting procedure takes into account the selected data and background events within a sliding mass window. The window is moved in steps of 1 GeV. Its width is chosen as to fully cover the reconstructed-mass distribution obtained from the signal MC. For this purpose, the total width is set to four times the mass resolution (RMS) at the respective mass point considered. A linear interpolation is used to obtain resolutions for mass values with no signal MC available. In addition, any shift of the reconstructed mass-spectrum with regard to the nominal mass is taken into account by shifting the mass window accordingly.

The limit setting starts with the choice of a confidence level, which is conventionally taken as 95 %. For a single decay channel, the upper limit on the number of signal events in the mass window, N_{ul}, is then given by:

$$0.95 = \frac{\int_0^{N_{ul}} P(n,s,b)ds}{\int_0^{\infty} P(n,s,b)ds}\,, \tag{6.1}$$

where $P(n, s, b)$ is the Poisson probability to observe n events when s signal and b background events are expected:

$$P(n, s, b) = \frac{1}{n!} \mathrm{e}^{-(s+b)} (s + b)^n \,. \tag{6.2}$$

The solution to (6.1) is found numerically. The approach employed here is equivalent to the one formely proposed by the PDG for setting upper limits on Poisson processes with background [121, 122]. It is known to yield conservative limits.

In the frequentist framework of probability, the number N_{ul} can be interpreted as follows: If the experiment was repeated an infinite number of times, a hypothetic excited-lepton signal would lead to a number of events observed which was smaller than N_{ul} in 95 % of all cases.

Having determined N_{ul}, the upper limit on $\sigma \times \mathrm{BR}$ follows from

$$(\sigma \times \mathrm{BR})_{ul} = \frac{N_{ul}}{\mathcal{L} \cdot \varepsilon \cdot \mathrm{BR}_{\gamma,Z,W}} \,, \tag{6.3}$$

using the integrated luminosity, $\mathcal{L}$, the selection efficiency, ε, and the branching ratio, $\mathrm{BR}_{\gamma,Z,W}$, of the gauge-boson decay involved ($\mathrm{BR}_\gamma = 1.0$ for the photonic decays of e^* and ν^*, $\mathrm{BR}_W = 0.68$ and $\mathrm{BR}_Z = 0.70$ for W and Z decaying hadronically).

Apart from using the signal efficiency, no further assumption about the nature of e^* and ν^* production and decays are made for determining $(\sigma \times \mathrm{BR})_{ul}$. In contrast to that, the calculation of an upper limit on f/Λ requires to presuppose a specific model. The conventional choice is the model of Hagiwara et al. (Sect. 2.2.2), so that the f/Λ limits from different experiments are rendered compatible. Yet even when using the same phenomenological model, the way towards $(f/\Lambda)_{ul}$ is not unequivocal. For there are different options how to handle the excited-lepton decay width. The most straightforward approach consists in using the narrow-width approximation (NWA), with which the e^* and ν^* cross sections have been calculated (Sect. 2.2.2). Those are adopted as reference cross sections, σ_{MC}, so that the upper limit on f/Λ is obtained from

$$(f/\Lambda)_{ul} = \sqrt{\frac{(\sigma \times \mathrm{BR})_{ul}}{\sigma_{MC} \times \mathrm{BR}_{MC}}} (f/\Lambda)_{MC} \,, \tag{6.4}$$

where BR_{MC} denotes the e^* or ν^* branching ratio according to the Hagiwara model, and the value of $(f/\Lambda)_{MC}$ is the one which has been assumed when calculating σ_{MC}, namely $1/\,\mathrm{TeV}$.

The procedure described up to here applies to single decay channels. It is conventional to derive limits on f/Λ as well from a combination of different channels. For this purpose, in (6.1) the Poisson likelihood is replaced by the product of the likelihoods of the (three) channels taken into account for either e^* or ν^*. Furthermore, the luminosity information

as well as the efficiency, the gauge-boson branching ratio and the excited-lepton branching ratio are included in the calculation of the integrals:

$$0.95 = \frac{\int_0^{\sigma_{ul}} \prod_{i=1}^{3} P_i(n_i, s', b_i) ds'}{\int_0^{\infty} \prod_{i=1}^{3} P_i(n_i, s', b_i) ds'} \,, \tag{6.5}$$

where the integration parameter is now $s' = s(\mathcal{L} \cdot \varepsilon \cdot \mathrm{BR}_{\gamma,Z,W} \cdot \mathrm{BR}_{MC})$, so that solving the equation provides directly a combined upper limit on the cross section, σ_{ul}. The latter is then employed to obtain the combined limit on f/Λ:

$$(f/\Lambda)_{ul}^{\mathrm{com}} = \sqrt{\frac{\sigma_{ul}}{\sigma_{MC}}} (f/\Lambda)_{MC} \,. \tag{6.6}$$

As can be seen, the procedure consists in calculating $(f/\Lambda)_{ul}^{\mathrm{com}}$ from a combined cross-section limit rather than deriving it from the single-channel limits on f/Λ. The resulting combined limits are not necessarily more stringent than each of the single limits. The curves obtained are displayed in the following sections.

Some attention is to be paid to the fact that, beyond a certain mass value, the decay width derived from the respective f/Λ limit is no longer consistent with the NWA which has been assumed to obtain this limit. Thus, the $(f/\Lambda)_{ul}$ curves extend no further than to masses at which the e^* or ν^* width derived from the respective limit value gains a size comparable to the experimental mass resolution.

The upper limits on $\sigma \times$ BR obtained for e^* and ν^*, respectively, are depicted in Sect. 6.2. The limits on f/Λ are shown in Sect. 6.3. Finally, Sect. 6.4 presents the outcome of the systematic checks. The latter have been performed in order to study the impact of systematic uncertainties on the limit values.

6.2 Upper limits on $\sigma \times$ BR

According to the procedure described in the preceding section, upper limits on the production cross-section times the branching ratio, $\sigma \times$ BR, have been calculated for each of the e^* and ν^* decay channels analysed. The input used by the limit-setting procedure for the respective channel comprises the distributions of observed and expected events as well as the signal efficiency. Moreover, the resolution and shift are employed to define the respective mass window at each step. The limit setting proceeds in steps of 1 GeV, whereas efficiency, resolution and shift values have been determined only for the ten masses of the signal samples available. Therefore, linear interpolations of these quantities are used for the mass points that lie in between.

Considering the overall performance of the two alternative selection approaches, the probability method has been demonstrated to yield superior sensitivity compared to the cut

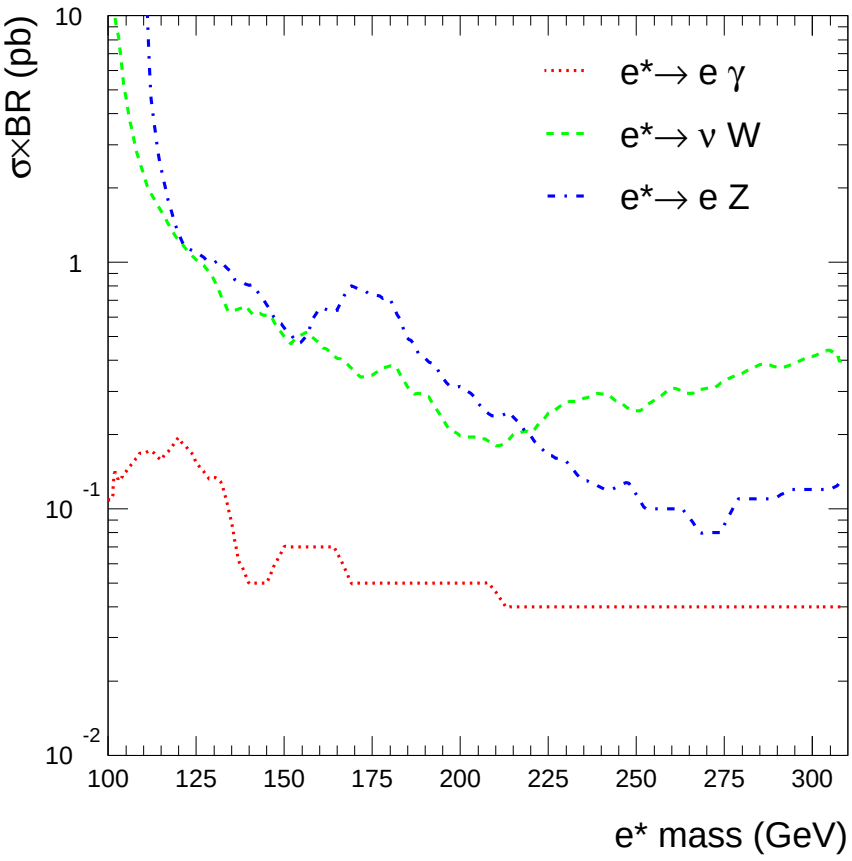

Figure 6.1: *Upper limits at* 95 % *confidence level on the excited-electron production cross-section times the branching ratio,* $\sigma \times \mathrm{BR}$*, as a function of the* e^* *mass. The curves displayed have been obtained with the decay channels* $e^* \to e\gamma$*,* $e^* \to \nu W \to \nu q\bar{q}'$ *and* $e^* \to eZ \to eq\bar{q}$*, using the probability-based selection procedure. The areas above the curves are excluded.*

selection. The search results of the probability method have therefore been used in all cases to derive the $\sigma \times \mathrm{BR}$ limits. The curves obtained for the three e^* decay channels are plotted in Fig. 6.1; the ν^* limit curves are shown in Fig. 6.2. In both cases, the mass range covered corresponds to the signal MC samples available, i.e. 100 GeV–310 GeV. As for excited electrons, by far the most stringent limits result from the photonic decay channel, which features the highest signal-to-background ratio due to its particular experimental signature. Somewhat less pronounced, this holds as well for the $\nu^* \to \nu\gamma$ decay in the excited-neutrino case.

The $\sigma \times \mathrm{BR}$ limits are specific to ep scattering, so that a comparison can only be made with the respective results published by H1 and ZEUS. The most recent publications of the H1 collaboration in this field are based on $37\,\mathrm{pb}^{-1}$ of e^+p and $15\,\mathrm{pb}^{-1}$ of e^-p data, respectively [66, 67]. With the former data set, $\sigma \times \mathrm{BR}$ limits have been obtained, which, for e^*, are not stronger than 10^{-1} pb; for ν^*, the respective limits are comparable to those

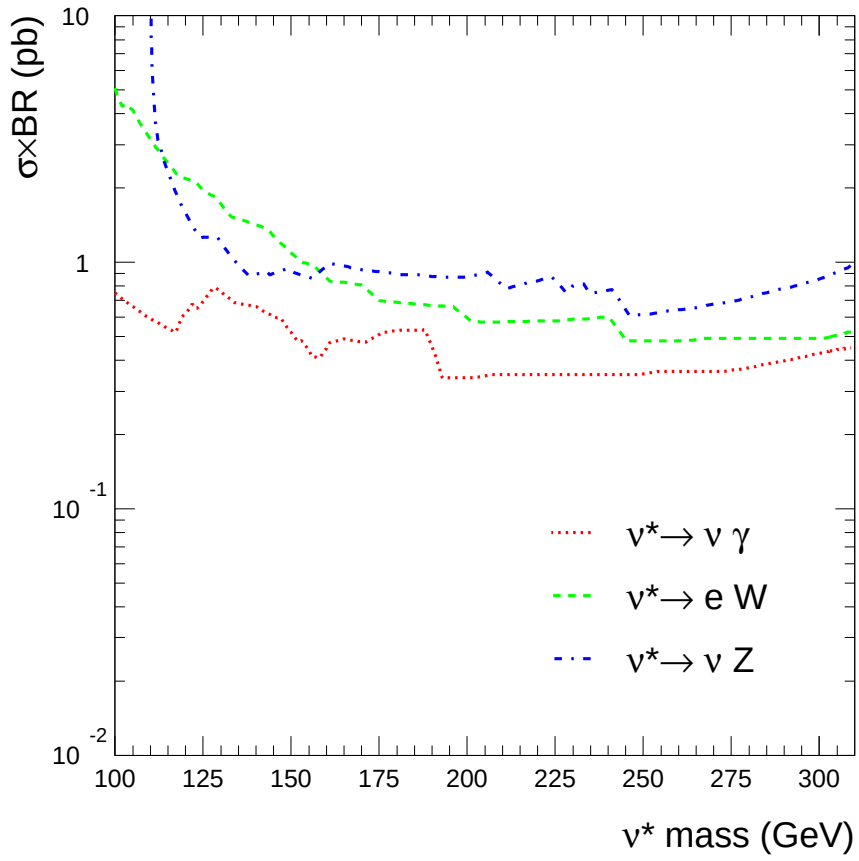

Figure 6.2: *Upper limits at 95 % confidence level on the excited-neutrino production cross-section times the branching ratio as a function of the ν^* mass. These limits are based on analyses of the decay channels $\nu^* \to \nu\gamma$, $\nu^* \to eW \to eq\bar{q}'$ and $\nu^* \to \nu Z \to \nu q\bar{q}$, carried out with the probability method. The areas above the curves are excluded.*

presented in Fig. 6.2. However, these H1 results cover the mass range up to 270 GeV only. For the search in e^-p data, no $\sigma \times$ BR limits are reported.

The ZEUS collaboration has recently published the results of an e^* search in 47.7 pb^{-1} of e^+p data and of a ν^* search in 16.7 pb^{-1} of e^-p data [72]. Both of them yield, for either e^* or ν^*, considerably more stringent $\sigma \times$ BR limits than provided by previous ZEUS papers [69–71]. The recently published e^* limits are weaker by about a factor of two than those displayed in Fig. 6.1, reflecting the smaller amount of luminosity used. The ν^* limits, however, have been obtained with the same data set as those in Fig. 6.2 and turn out to be comparably stringent. The ν^* search presented in this thesis has in fact served as a cross-check analysis for the results of the recent ZEUS publication. The decay channels analysed in the recent paper have precedingly been covered by several conference contributions [123–125]. An e^* search which covers the same experimental data as the analysis presented here has been reported lately by ZEUS [126]. This conference paper, however, comprises only the $e^* \to e\gamma$ channel.

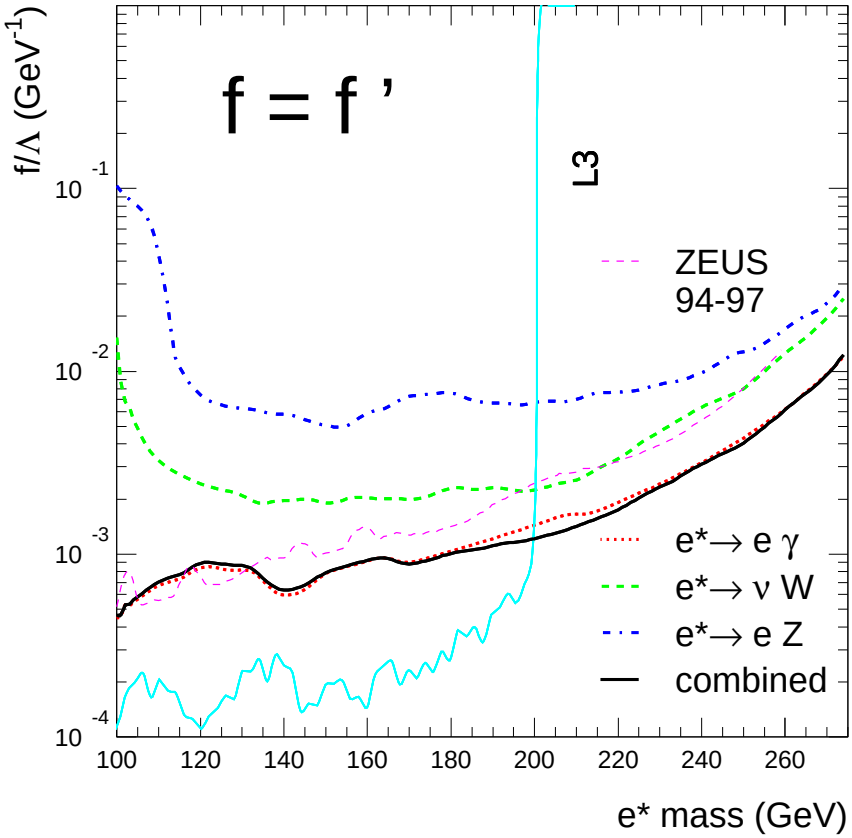

Figure 6.3: *Upper limits at 95 % confidence level on the coupling f/Λ as a function of the excited-electron mass, assuming $f = f'$. The curves for the single channels have been derived from the $\sigma \times \mathrm{BR}$ limits which are displayed in Fig. 6.1. In addition, the solid black curve represents the limits obtained from combining the three decay channels. For comparison, the corresponding limits contained in the recent ZEUS publication [72] are plotted. Those are based on 47.7 pb^{-1} of e^+p data recorded during 1994–97. Moreover, the (direct) e^* coupling limits from L3 [62] are shown. The areas above the curves are excluded.*

6.3 Upper limits on f/Λ

From the $\sigma \times \mathrm{BR}$ limits presented in the preceding section, upper limits on the coupling over the compositeness scale, f/Λ, have been derived. According to the procedure discussed in Sect. 6.1, this requires additional model-specific input. For that purpose, the e^* and ν^* cross sections and branching ratios stated in Sect. 2.2.2 have been adopted. Moreover, $f/\Lambda_{MC} = 1/\,\mathrm{TeV}$ has been used as the reference coupling for calculating the cross sections as well as for deriving the limits.

Concerning the choice of the coupling constants, for e^* it is conventional to consider only the case $f = f'$, which allows for decays to all three gauge bosons. The limits obtained thereby are shown in Fig. 6.3. If, in contrast, the relation $f = -f'$ was assumed, the decay $e^* \to e\gamma$ would be suppressed. For ν^* the situation is reversed: The latter choice

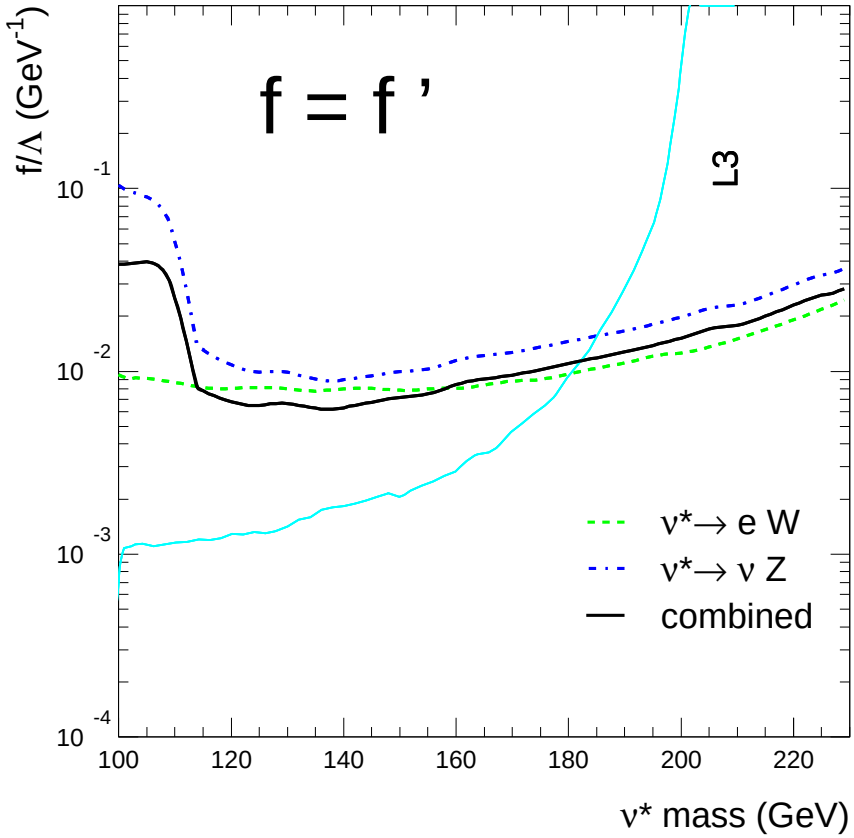

Figure 6.4: *Upper limits at 95 % confidence level on the coupling f/Λ as a function of the excited-neutrino mass, assuming $f = f'$. The single-channel limits have been derived from the respective $\sigma \times$ BR limits in Fig. 6.2. Combining both channels yields the solid black curve. The $\nu^* \rightarrow \nu\gamma$ channel is not present in the plot, since the photonic ν^* decay is suppressed for this particular choice of the constants f and f'. The corresponding L3 limits are displayed for comparison. The areas above the curves are excluded.*

would allow for photonic decays, whereas $f = f'$ would not. Here it is customary to derive f/Λ limits separately for both $f = f'$ and $f = -f'$, which means to assume different ν^* branching ratios (Sect. 2.2.2). The resulting limits are presented in Figs. 6.4 and 6.5, respectively.

The coupling limits can be compared among experiments featuring different initial-state particles, provided that the same theoretical model is assumed. Fortunately, the phenomenological Hagiwara model, which is described in Sect. 2.2.2, incorporates a common theoretical basis for excited-fermion searches performed at different collider experiments.

At present, competing f/Λ limits are provided by the LEP experiments. Those “direct” limits are obtained from searches for singly produced excited leptons, so that the experimental sensitivity is limited by the centre-of-mass energy. The most recent publication

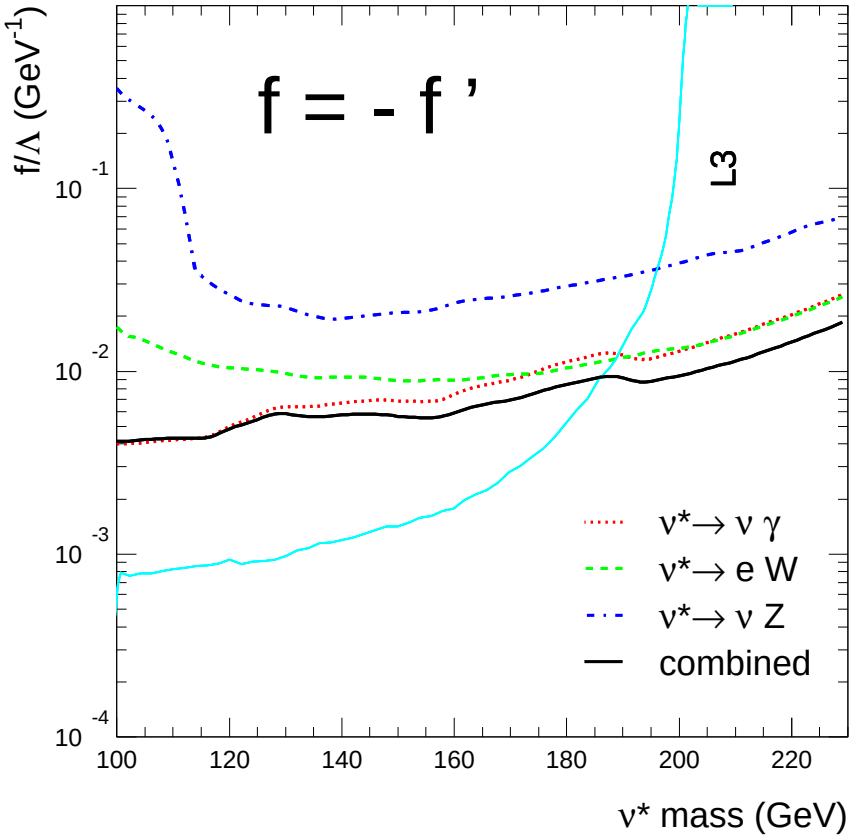

Figure 6.5: *Upper limits at 95 % confidence level on the coupling f/Λ as a function of the excited-neutrino mass, assuming $f = -f'$. For this choice of f and f', the photonic ν^* decay is allowed. The single-channel limits have been derived from the respective $\sigma \times$ BR limits in Fig. 6.2, and the solid black curve represents the combined limits. The L3 limits for $f = -f'$ are shown as well. The areas above the curves are excluded.*

stems from L3 [62]. The direct limits presented therein have been adopted for comparison purposes (Figs. 6.3, 6.4 and 6.5).

There exist as well "indirect" e^* limits from the LEP experiments, which are achieved by analysing the $\gamma\gamma$ final state. The latter is sensitive to t-channel exchange of excited electrons, so that these limits can extend to masses beyond the centre-of-mass energy. The most recent indirect e^* limits from the LEP experiments [63] cover the mass range up to 300 GeV. The exclusion strength achieved is comparable to the combined e^* limits presented here. Moreover, by searching for pair-produced excited leptons, the LEP experiments can set stringent lower limits on the e^* and ν^* masses. Thus, excited-lepton masses below approximately 100 GeV have been ruled out at 95 % confidence level [62].

In principle, the comparison with existing H1 and ZEUS limits discussed in the preceding section applies to the f/Λ limits as well. The cross-section limits are inversely proportional

to the respective integrated luminosity, $\mathcal{L}$, whereas the coupling limits scale with $1/\sqrt{\mathcal{L}}$. The yield due to increased luminosity is thus less prominent for the f/Λ limits.

The ν^* search in e^-p data recently published by H1 [67] yields f/Λ limits which are comparable to those presented in Figs. 6.4 and 6.5 when regarding masses up to 200 GeV. For higher masses, H1 discards the use of the narrow-width approximation. A closer examination of the different approaches is still under way. As for the e^* limits, the "combined" curve from the recent ZEUS publication is plotted for comparison in Fig. 6.3. The respective ν^* curves, which are not shown explicitly, are comparable to those presented here.

As discussed in Sect. 6.1, the mass range of the coupling limits is restricted by the use of the narrow-width approximation. A pragmatic criterion consists in displaying these limits no further than up to the mass at which the total decay width following from the respective combined limit (Sect. 2.2.2) becomes approximately as large as the mass resolution. Assuming a resolution of 20 GeV, the e^* (ν^*) limits shown here have therefore not been extended beyond 275 GeV (230 GeV). For higher masses, the resulting widths would increase rapidly.

6.4 Systematic studies

The exclusion limits stated in the preceding sections are affected by several sources of systematic uncertainties. On the one hand, experimental uncertainties are associated with the luminosity measurement and the efficiency interpolation, as well as with the electron finding, the CAL energy scale and the vertex simulation. On the other hand, theoretical uncertainties are introduced by the simulations of the background and of excited-lepton production and decay.

It is not appropriate to state errors on upper limits representing a given confidence level. Including the different sources of uncertainties in the derivation of the limits, on the other hand, is a problematic task. For that reason, the impact of the systematic uncertainties on the results obtained will be made transparent as follows.

For each source of uncertainty considered, the event selection has been repeated, with the respective parameter under study being varied within an appropriate range. Then the $\sigma \times \mathrm{BR}$ limit setting has been carried out using the respective results obtained. Thus, the systematic checks yield variations of the upper limits to be compared with the nominal limit curves.

The different contributions to the systematic uncertainty that have been taken into account as well as the impact of the single checks are discussed below. In Table 6.1 the respective numbers of candidates and background events obtained are listed for each of the six channels. In Fig. 6.6 the respective upper limits on $\sigma \times \mathrm{BR}$ are displayed. The

relative deviations of these limits from the nominal ones are depicted in Fig. 6.7. For the systematic checks, the probability-based selection method has been used throughout.

- Electron finder (A):
  to estimate the uncertainty associated with the EM electron finder, the neural-net based program SINISTRA 95 has been used alternatively (Sect. 4.2.3);
- hadronisation model (B):
  the uncertainty introduced by the specific hadronisation model (MEPS) employed for the background MC (Sect. 5.2.1) is difficult to assess. Alternatively to MEPS, the second customary model, ARIADNE, has been used as a systematic check;
- CAL energy scale (C, D):
  depending on the calorimeter part considered, the absolute energy scale is uncertain up to the level of $\pm 3\,\%$ (Sect. 3.2.3). For the respective checks performed, all CAL energies have been scaled within these boundaries;
- vertex distribution (E, F):
  the simulated vertex distribution is known to exhibit deviations from the corresponding experimental distribution [97]. The impact on the upper limits thus caused has been estimated by changing the vertex requirement from $|Z_{\mathrm{vtx}}| < 50\,\mathrm{cm}$ to $|Z_{\mathrm{vtx}}| < 65\,\mathrm{cm}$ and $|Z_{\mathrm{vtx}}| < 35\,\mathrm{cm}$, respectively;
- background simulation (G, H):
  the overal uncertainty on the background contains contributions from the statistical uncertainties of the MC samples as well as from theoretical uncertainties of the simulated processes (e.g. the hadronisation model, as discussed above separately). Moreover, when it comes to rare processes and small event numbers, apparently non-central features of the MC generators are more likely to have noteworthy impact on the numbers of background events obtained. That is the case, e.g., for photon radiation off the W propagator in CC events not being simulated by DJANGOH [127, 128]. Such radiative CC events, however, could give rise to considerable amounts of background in the $\nu^* \to \nu\gamma$ channel, as claimed by H1 [66].
  In the course of the systematic checks, the background numbers have been varied by $\pm 50\,\%$, which represents a worst-case scenario rather than a fair estimate of the actual background uncertainty;
- luminosity:
  the systematic uncertainty of the luminosity measurement is $1.8\,\%$ ($2.25\,\%$) for the 98/99 $e^- p$ (99/00 $e^+ p$) data (Sect. 3.2.4). As the upper limits on $\sigma \times \mathrm{BR}$ are inversely proportional to the integrated luminosity (Sect. 6.1), varying the luminosity by the quoted numbers yields correspondingly large changes of the limits;
- efficiency interpolation:
  concerning its correlation to $(\sigma \times \mathrm{BR})_{ul}$, the same argument as for the luminosity holds

for the selection efficiency, too (Sect. 6.1). At the mass points available, the absolute statistical uncertainty of the efficiency amounts to approximately $\pm 1\,\%$ (Sect. 5.6.8). For the mass values in between, the efficiencies are obtained by linear interpolation, leading to an uncertainty of comparable size;

- excited-lepton simulation:
  further sources of systematic uncertainty on the selection efficiency are constituted by theoretical uncertainties associated with excited-lepton production and decay. In earlier studies [70, 71], radiative corrections and the use of different PDFs to model the proton in the signal MCs (Sect. 5.2.2) were found to give rise to an uncertainty on the efficiency of the order of $8\,\%$. Moreover, the dependence of the efficiency on the spin states assumed for the excited leptons were investigated. For that purpose, the nominal decay-angle distribution was changed from $1 + \cos\theta^*$ (Sect. 2.2.2) to an isotropic distribution, which made the efficiency deviate by at most $5\,\%$. Those signal-related effects have not been reevaluated for this analysis. The quoted uncertainties are assumed to persist approximately.

As can be seen from Figs. 6.6 and 6.7, for most channels and sources of systematic uncertainties the upper limits do not deviate more than about $\pm 25\,\%$ from the nominal curves. However, in some cases larger deviations are observed. That holds for the electron-finder check (A) in $e^* \to e\gamma$ and $\nu^* \to eq\bar{q}'$, where the use of SINISTRA 95 leads to considerably weaker limits in the medium-mass range and to an increased number of data and background events selected (Table 6.1).

Varying the number of background events (G,H) generates changes of the $\sigma \times \mathrm{BR}$ limits in either direction (increased background means stronger limits). In spite of $\pm 50\,\%$ being quite a drastic variation, substantial changes are observed only for $e^* \to eq\bar{q}$ and, particularly, for $e^* \to \nu q\bar{q}'$. As pointed out above, $\nu^* \to \nu\gamma$ is presumably associated with the largest background uncertainty among the channels under study. Thus it is reassuring to note that for $\nu^* \to \nu\gamma$ the background-induced impact on the upper limits is fairly negligible.

The second background-related check consists in the use of an alternative hadronisation model for the NC and CC samples (B). This check gives rise to substantial changes in case of the $e^* \to \nu q\bar{q}'$ limits only, reflecting the numbers of expected events being reduced over the complete mass range (Table 6.1).

The energy-scale checks (C, D) lead to noteworthy changes in the $e^* \to eq\bar{q}$ limits only. The largest deviations observed are confined to the low-mass region. These deviations, which are towards weaker limits, correspond to varying the energy scale by $-3\,\%$.

The variation of the vertex cut (E, F) does not give rise to mentionable changes in the upper limits except for $\nu^* \to \nu\gamma$. In this channel, two additional candidates enter the final event sample (Table 6.1), leading to weaker limits for masses $\lesssim 200\,\mathrm{GeV}$.

systematic check		$e^* \to e\gamma$		$e^* \to \nu q\bar{q}'$		$e^* \to eq\bar{q}$	
		obs.	expected	obs.	expected	obs.	expected
A	Sinistra	20	21.8 ± 1.4	65	72.7 ± 1.0	37	50.6 ± 1.7
B	Ariadne	11	11.3 ± 0.6	75	46.9 ± 0.9	43	55.2 ± 1.1
C	E scale +3 %	11	12.7 ± 0.9	86	82.4 ± 1.2	45	53.9 ± 1.7
D	E scale −3 %	10	12.7 ± 0.9	65	63.3 ± 1.0	38	44.4 ± 1.7
E	$\lvert Z_{\text{vtx}}\rvert < 65\,\text{cm}$	11	13.6 ± 1.0	76	73.5 ± 1.1	44	51.6 ± 1.7
F	$\lvert Z_{\text{vtx}}\rvert < 35\,\text{cm}$	11	13.4 ± 1.0	71	71.0 ± 1.0	43	50.6 ± 1.7
nominal analysis		11	13.6 ± 1.0	75	72.7 ± 1.1	43	51.2 ± 1.7

systematic check		$\nu^* \to \nu\gamma$		$\nu^* \to eq\bar{q}'$		$\nu^* \to \nu q\bar{q}$	
		obs.	expected	obs.	expected	obs.	expected
A	Sinistra	5	2.4 ± 0.2	12	11.6 ± 0.6	5	4.5 ± 0.2
B	Ariadne	3	3.1 ± 1.4	8	14.9 ± 0.6	5	3.2 ± 0.2
C	E scale +3 %	3	3.3 ± 1.4	10	13.0 ± 0.6	5	5.4 ± 0.3
D	E scale −3 %	3	3.3 ± 1.4	8	10.1 ± 0.5	5	4.1 ± 0.2
E	$\lvert Z_{\text{vtx}}\rvert < 65\,\text{cm}$	5	3.4 ± 1.4	8	12.0 ± 0.6	5	5.0 ± 0.2
F	$\lvert Z_{\text{vtx}}\rvert < 35\,\text{cm}$	3	3.3 ± 1.4	8	11.8 ± 0.6	5	4.9 ± 0.2
nominal analysis		3	3.3 ± 1.4	8	12.0 ± 0.6	5	4.9 ± 0.2

Table 6.1: *Overview of observed and expected events obtained when performing the different systematic checks. For comparison, the event numbers of the nominal analyses are also stated. All numbers shown have been obtained with the probability-based selection method.*

As for the f/Λ limits, the stated checks would lead to smaller relative changes, because those limits are proportional to the square root of $(\sigma \times \text{BR})_{ul}$ (Sect. 6.1). On the other hand, as being more theory-loaded, the upper limits on f/Λ are affected by additional sources of theoretical uncertainties, for instance the ceasing validity of the narrow-width approximation at higher masses or the interpolation of the production cross-sections. Since $(f/\Lambda)_{ul}$ is a highly model-dependent quantity anyway, the latter effects have not been evaluated.

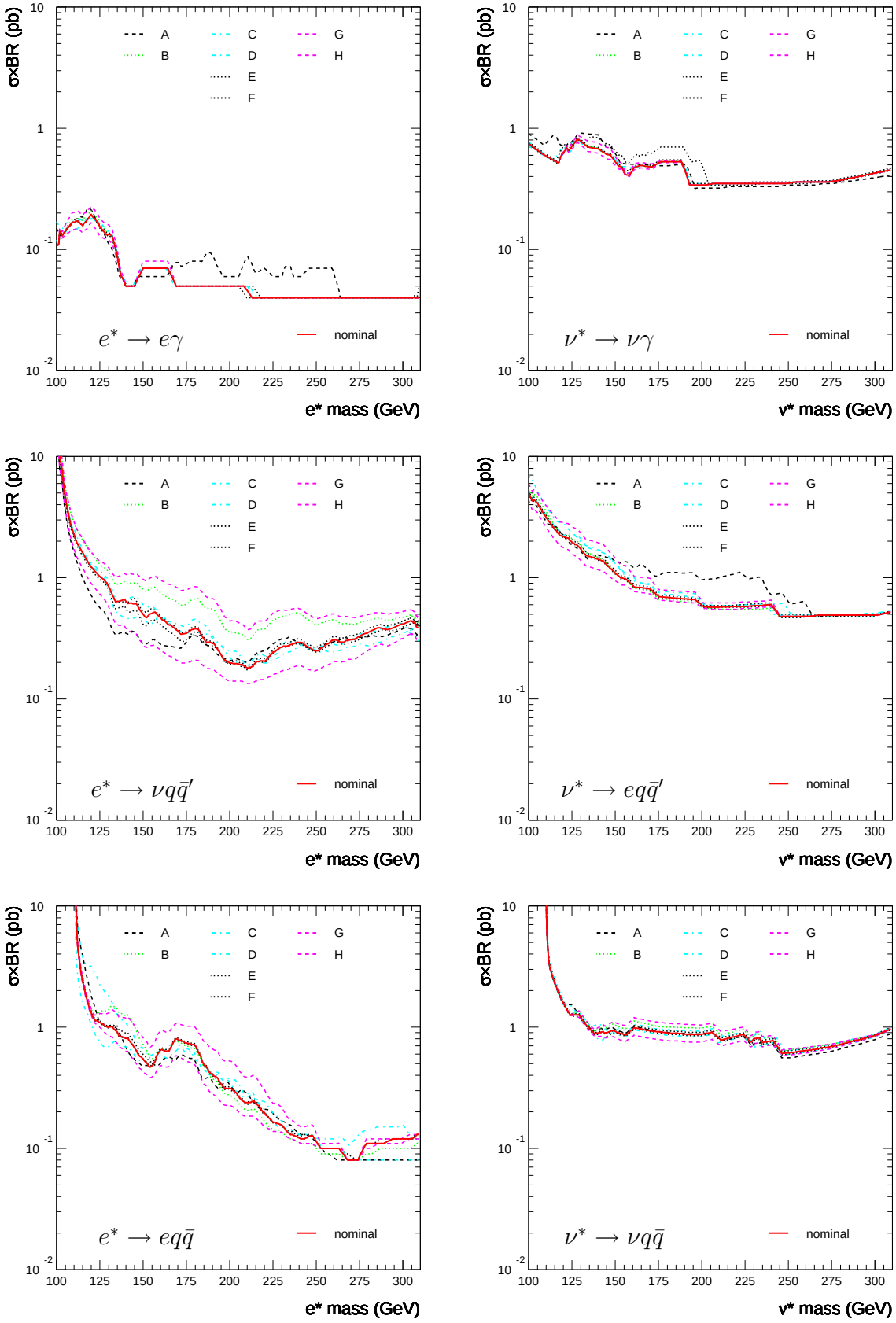

Figure 6.6: *Upper limits on $\sigma \times \mathrm{BR}$ resulting from the different systematic checks (A–H). Also shown are the nominal curves (solid lines), which correspond to the single-channel limits in Fig. 6.1 (e^*) and Fig. 6.2 (ν^*), respectively. All curves displayed have been obtained using the probability-based selection method.*

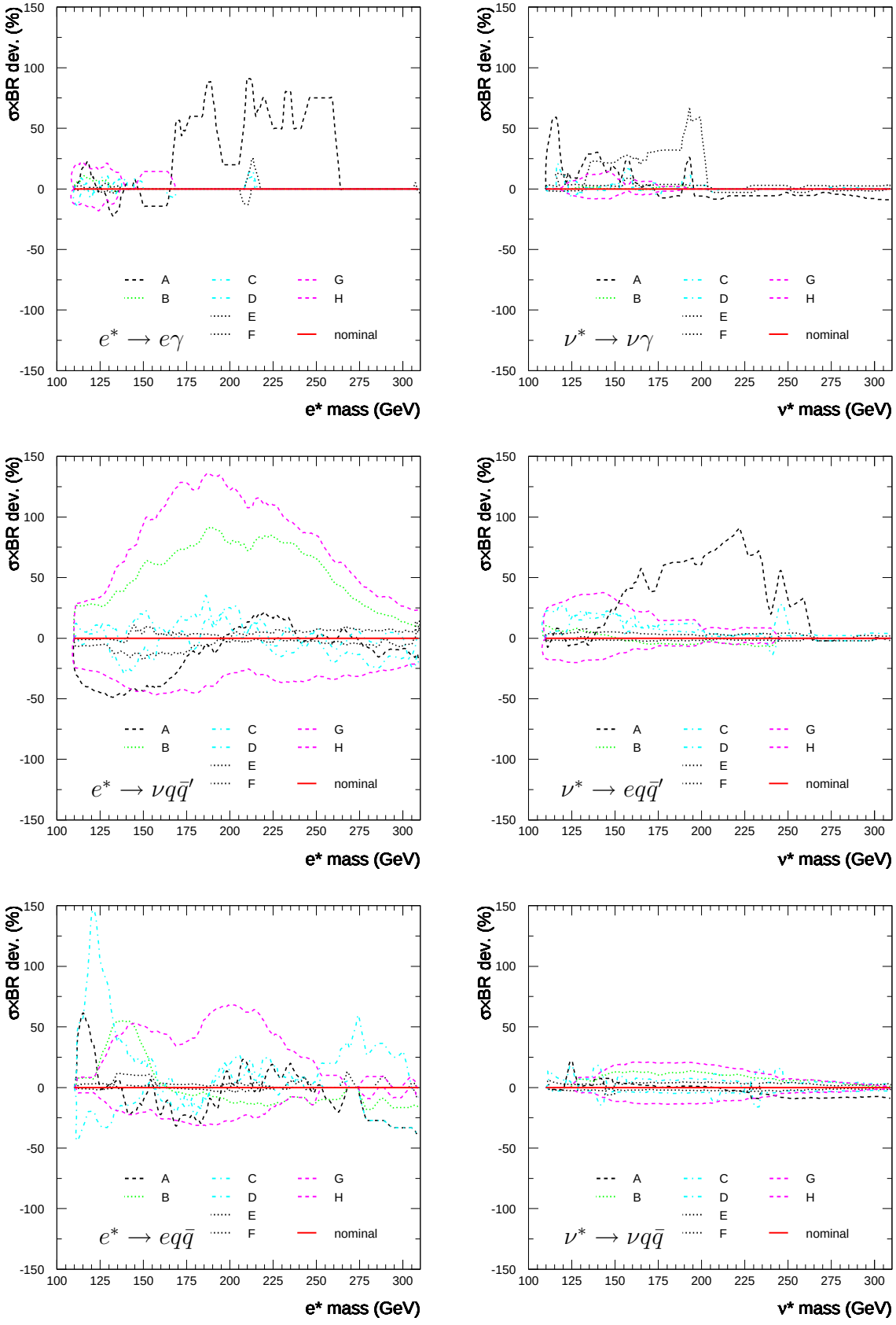

Figure 6.7: *Relative deviations of the $\sigma \times \mathrm{BR}$ limits due to the different systematic checks, measured with respect to the nominal limits. The corresponding limit curves are displayed in Fig. 6.6.*

Chapter 7

Summary

The analysis presented in this thesis is concerned with the question whether electrons and neutrinos are actually composite rather than elementary particles. With the leptons up to now being considered as pointlike objects, the idea of their having substructure is not only compelling by itself, but also constitutes the basis for a number of compositeness theories which are intended to cure inherent problems of the Standard Model.

Lepton compositeness would give rise to the existence of heavy excited states. Given that their mass was smaller than the centre-of-mass energy, these excited states could be produced directly in high-energy ep scattering, as provided by the HERA collider. Once produced, an excited electron or neutrino would decay into a standard lepton and a gauge boson (γ, Z, W). The energies and trajectories of the decay particles could then be measured with the ZEUS detector.

In the framework of this analysis, e^-p and e^+p scattering data, taken at a centre-of-mass energy of 318 GeV, have been used. The former were recorded with the ZEUS detector during the running period 1998/99 and correspond to an integrated luminosity of $16.7\,\mathrm{pb}^{-1}$. The latter stem from the subsequent data-taking period which lasted until 2000 and represent an integrated luminosity of $66.1\,\mathrm{pb}^{-1}$.

Excited neutrinos have been sought via the decay channels $\nu^* \to \nu\gamma$, $\nu^* \to eW \to eq\bar{q}'$ and $\nu^* \to \nu Z \to \nu q\bar{q}$. This search has been performed in the e^-p scattering data, since the excited neutrinos' being produced via W exchange gives rise to a considerably higher ν^* cross section for e^-p than for e^+p reactions. As for excited electrons, the production of which is mediated by γ/Z exchange, both types of reactions offer the same sensitivity for a search. Consequently, the full amount of data has been employed, considering the decay channels $e^* \to e\gamma$, $e^* \to \nu W \to \nu q\bar{q}'$ and $e^* \to eZ \to eq\bar{q}$.

The experimental data have been subjected to a number of cleaning cuts to suppress backgrounds from non-ep reactions which have made their way into the data samples in spite of the selective trigger system. Monte Carlo simulations have been used to estimate

the backgrounds from well-known ep processes such as NC/CC DIS, photoproduction and QED-Compton scattering. The simulations of the sought-after signal events are based on the phenomenological compositeness model of Hagiwara et al. which is commonly used for excited-lepton searches. All types of simulated events have undergone the same offline reconstruction as the experimental data.

Prior to the actual event selection, a set of preselection cuts has been applied in each channel. The aim is to preselect decent event samples and to demonstrate that the experimental data are well described by the background simulations. For the final event selection, two different approaches have been employed, providing a means of mutual cross checking.

The first incorporates a conventional approach, making use of fixed selection cuts. In contrast to that, the second method consists in a multi-dimensional, probability-based procedure. That approach features a systematic way of optimising the selection criteria. The outcome of both selection methods comprises the mass spectra of the candidate events and the corresponding backgrounds, as well as the selection efficiencies and mass resolutions determined with the signal simulations.

The mass spectra have been subjected to a statistical test, investigating the compatibility of the observed events with the expected backgrounds. No evidence for an excited-electron or -neutrino signal is seen in any of the channels analysed. Since no excess of events is observed, upper limits at 95 % confidence level have been set on the production cross-section times the branching ratio, $\sigma \times \mathrm{BR}$. These limits contain no model-related input other than the selection efficiencies.

Upper limits, for the single decay channels as well as combining them, on the coupling over the compositeness scale, f/Λ, have in addition been derived directly from the cross-section limits. Thereto additional model-specific assumptions and the narrow-width approximation have been used. In the e^* case, the f/Λ limits have been derived assuming $f = f'$ for the coupling constants; for the ν^* limits, the two cases $f = f'$ and $f = -f'$ have been considered.

The limit curves displayed have been derived from the results of the probability-based selection method, because this approach has proven to yield better overall performance than the cut selection. With the exclusion limits obtained, considerable improvement compared to existing limits has been achieved. The improvement is twofold: Firstly, the covered range is extended towards higher masses; secondly, in many cases these new limits are more stringent than the existing ones.

Appendix A

Examples of candidate events

For each decay channel under study, one candidate event is displayed below. Shown here are the events with the highest reconstructed mass in the respective channel, using the probability-based selection method.

$e^* \to e\gamma$ $\qquad\qquad$ $m_{e\gamma} = 156.1\,\mathrm{GeV}$

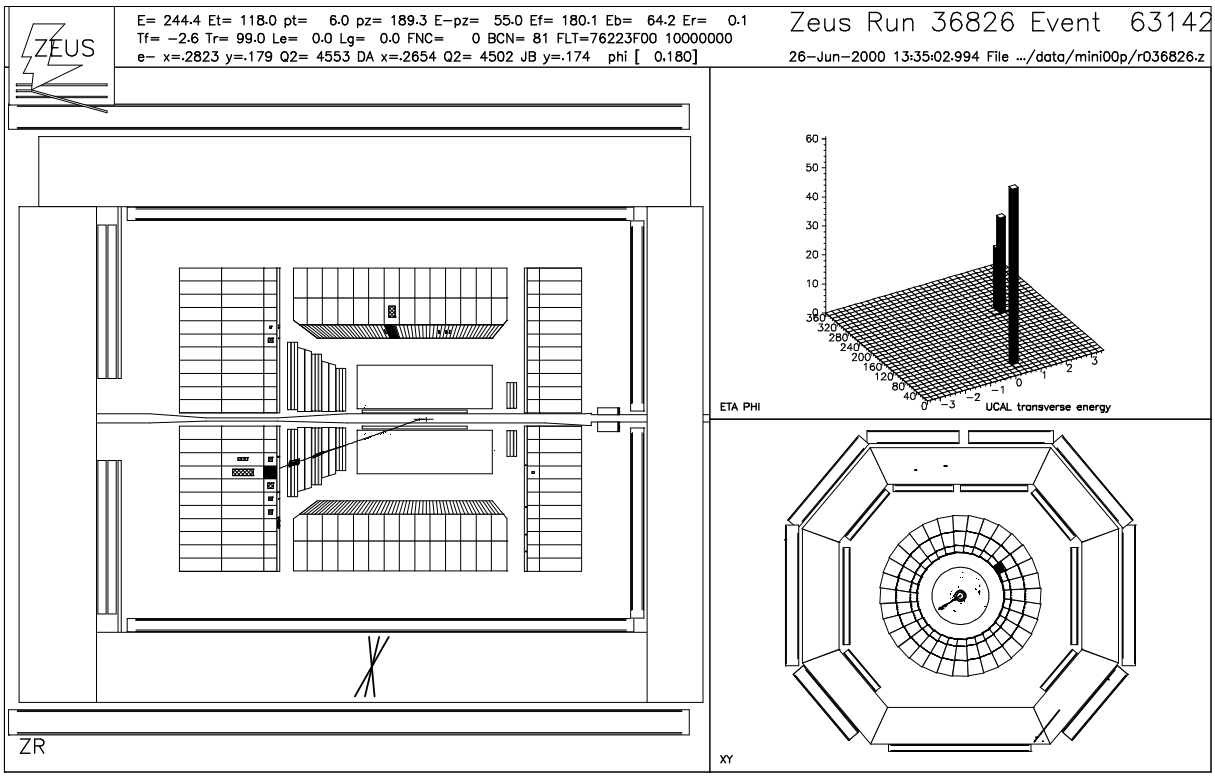

$e^* \to \nu W \to \nu q\bar{q}'$ $\qquad m_{\nu W} = 249.1\,\mathrm{GeV}$

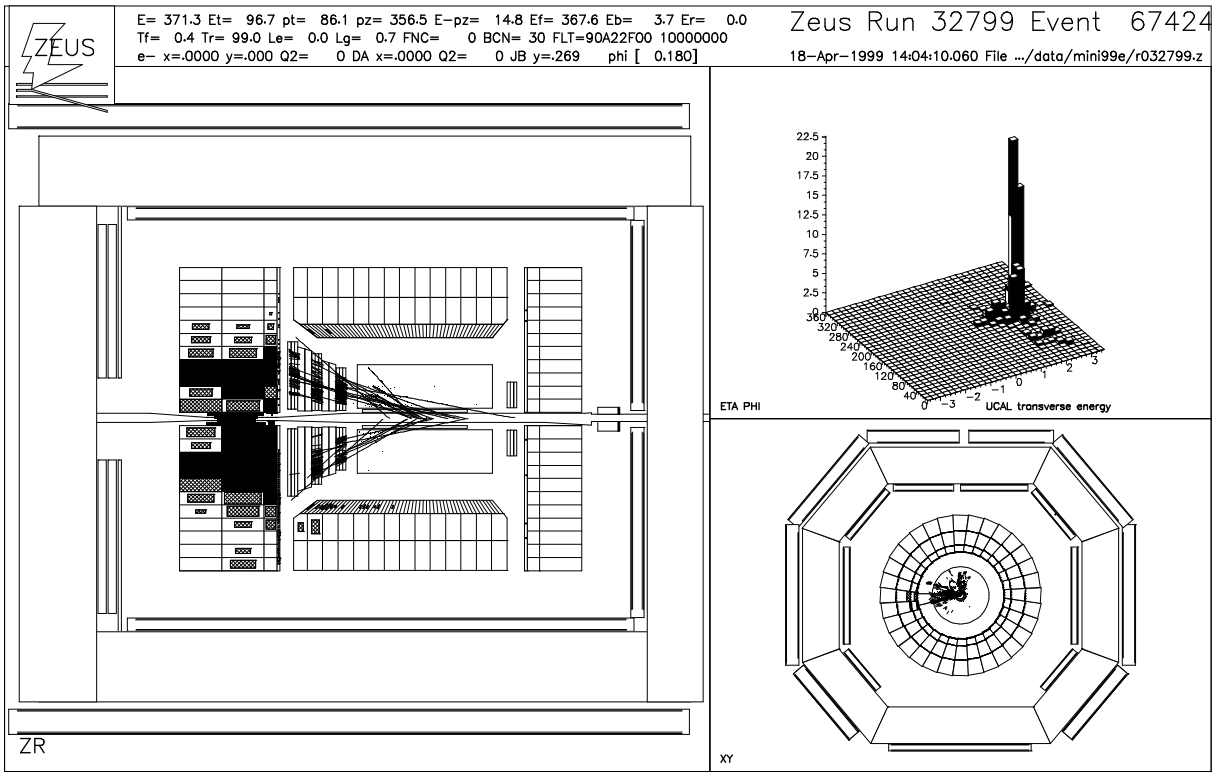

$e^* \to eZ \to eq\bar{q}$ $\qquad m_{eZ} = 299.2\,\mathrm{GeV}$

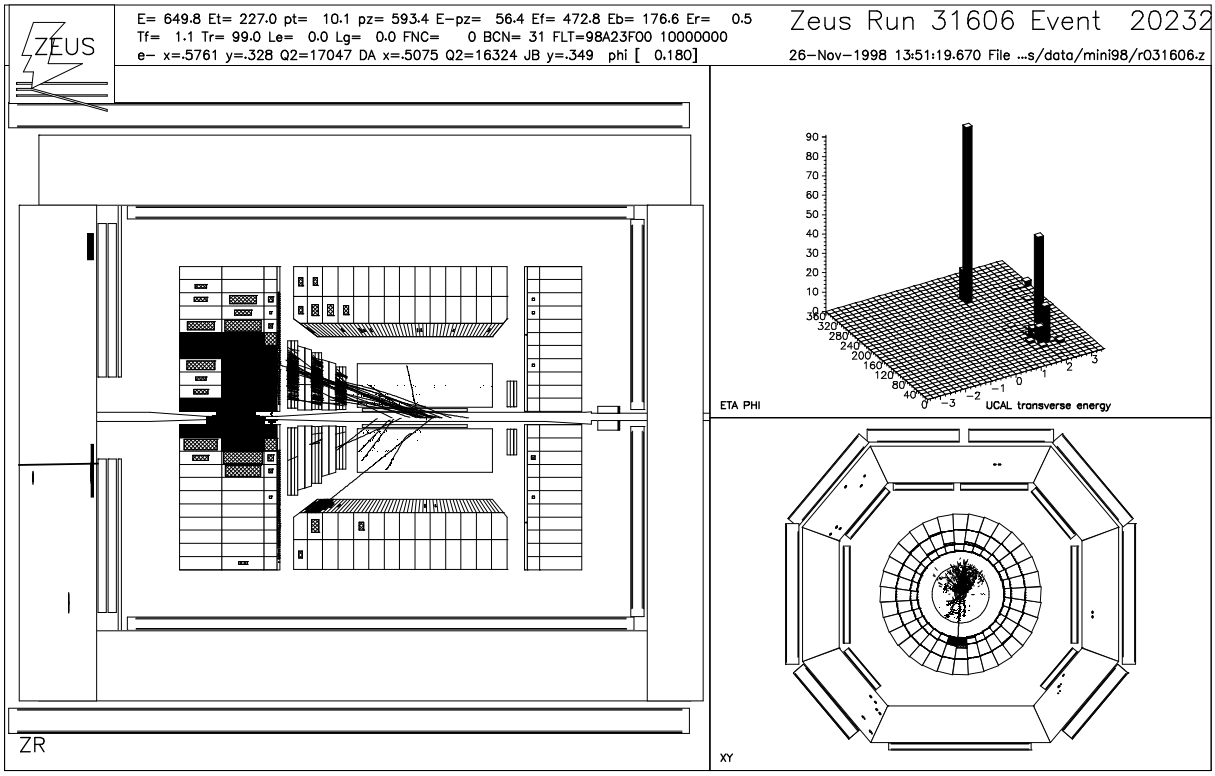

$\boldsymbol{\nu^* \to \nu\gamma}$ $\qquad\qquad$ $m_{\nu\gamma} = 174.3\,\mathrm{GeV}$

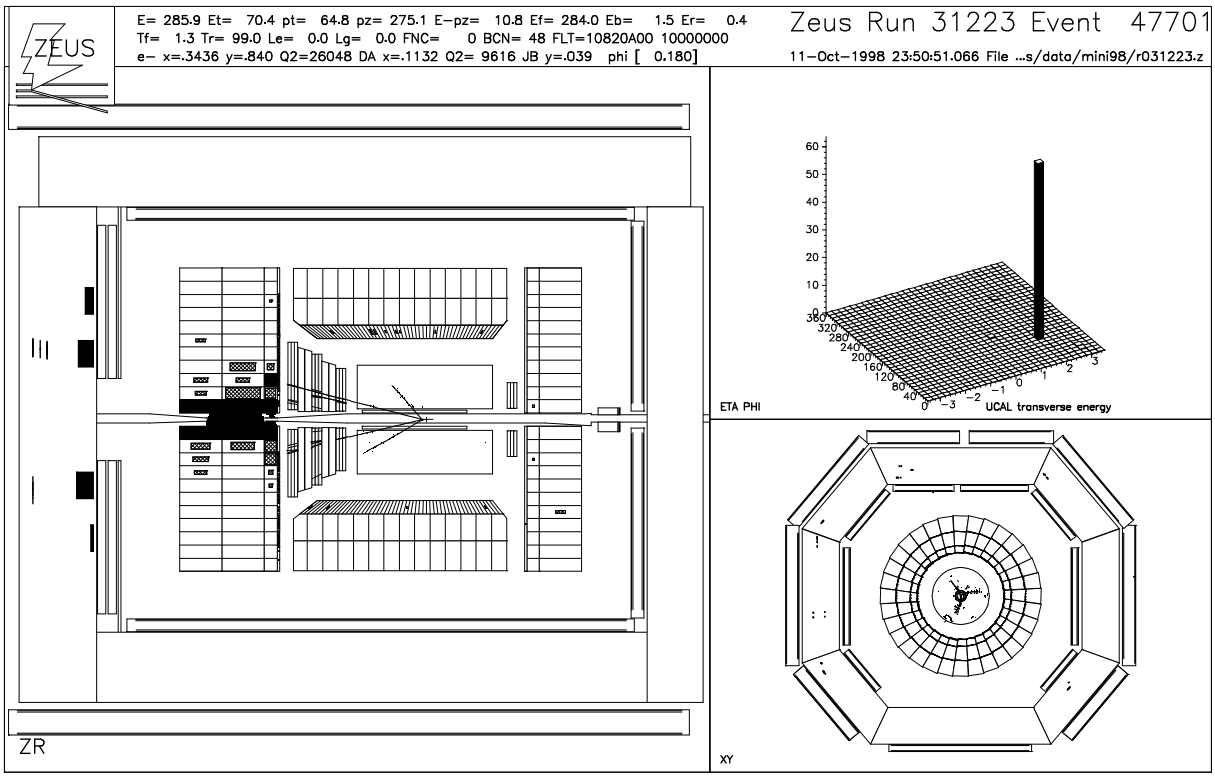

$\boldsymbol{\nu^* \to eW \to eq\bar{q}'}$ $\qquad\qquad$ $m_{eW} = 198.6\,\mathrm{GeV}$

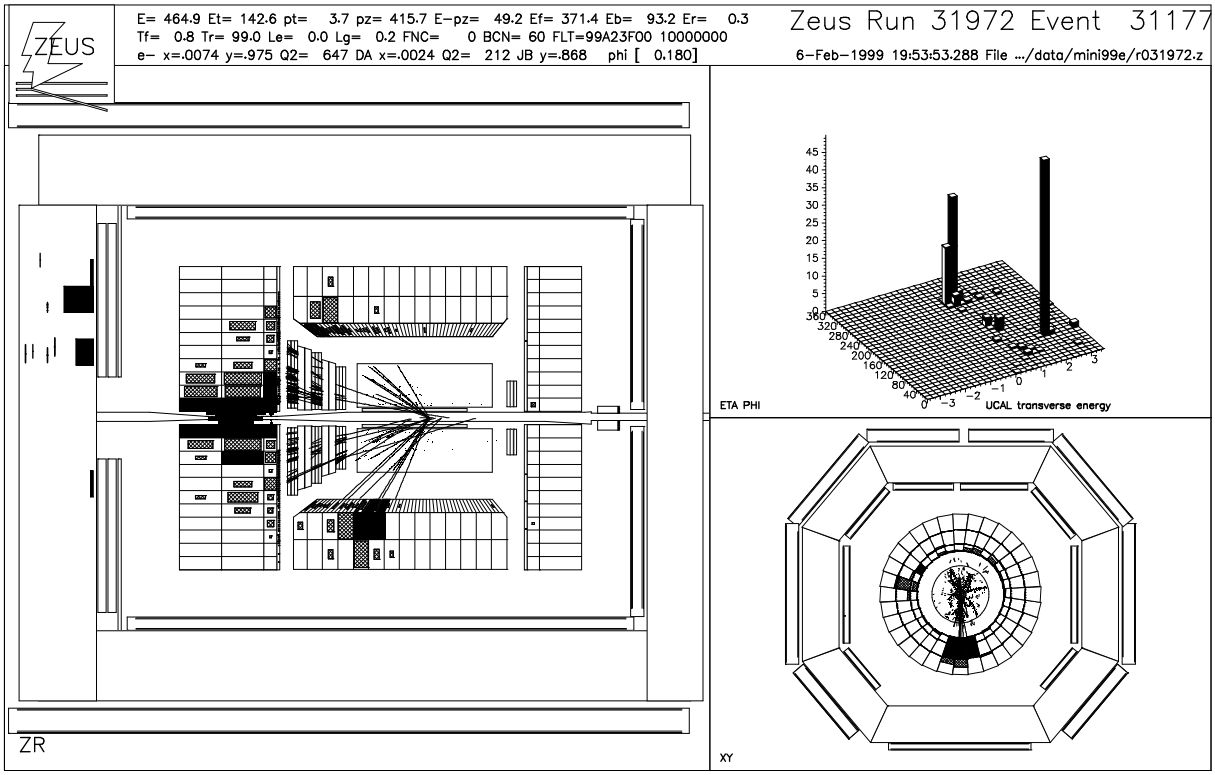

$\boldsymbol{\nu^* \to \nu Z \to \nu q\bar{q}}$ $\qquad m_{\nu Z} = 242.6\,\mathrm{GeV}$

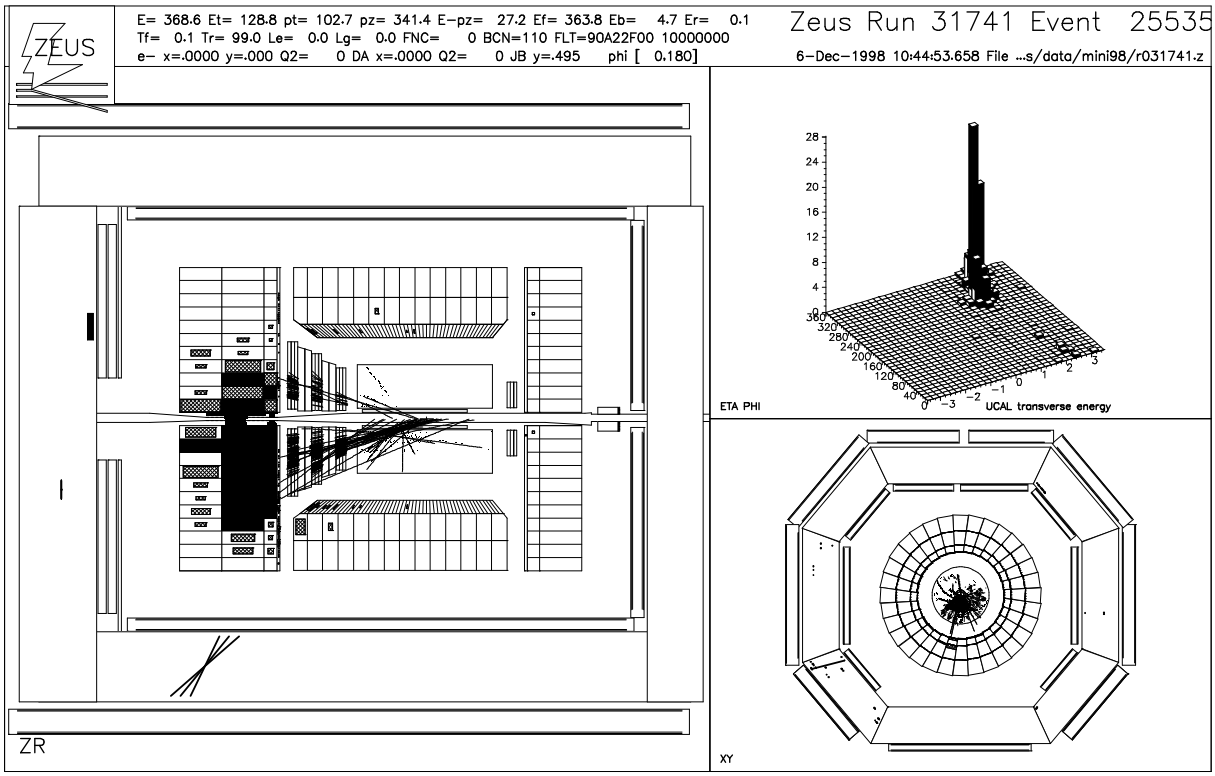

Appendix B

Definitions of DST bits

Listed below are the definitions of the DST bits used for this analysis (Sect. 5.4.1):

- B33 Neutral Current:

  1. TLT(4) | TLT(5) | TLT(7) | MuTrig
  2. Timing Cuts
  3. E-Pz > 32 GeV
  4. Ee > 8 GeV
  5. Q2e > 160 GeV2 | Q2da > 160 GeV2
  6. Pt,e > 2 GeV

- B34 Charged Current:

  1. TLT(2) | TLT(6) | Pt[-ir] > 6 GeV
  2. Pt > 7 GeV
  3. Events which satisfy all of the following 8 conditions are vetoed:
     1) .not.ExoTLT(2)
     2) Pt[-ir] < 10 GeV
     3) Pt < 25 GeV
     4) Pt/Et < 0.7
     5) E-Pz < 10 GeV
     6) Pt/Pz < 0.08
     7) Px < 0
     8) abs(Py) < 4 GeV

- B35 Island Et:

  1. TLT(15) | Et(-islands with Eta > 2.7) > 20 GeV
  2. Vertex with -60 cm < zVtx < 120 cm

- B36 High Et:

  1. TLT(3) |
     (Et(-ir) > 35 GeV | Et(-ir) > 30 GeV & E-Pz > 10 GeV)
  2. Vertex with -60 cm < zVtx < 120 cm

  OR

  1. Et(-ir) > 50 GeV

- B37 Good Vertex:

  1. Either VC or TLT vtx with -60 cm < zVtx < 120 cm

References

[1] H. Spiesberger, M. Spira and P.M. Zerwas, Preprint hep-ph/0011255, 2000. Also available as DESY T-00-01, MZ-TH/00-53, PSI-PR-00-17.

[2] Particle Data Group, D.E. Groom et al., Eur. Phys. J. **C 15**, 1 (2000).

[3] S.L. Glashow, Nucl. Phys. **22**, 579 (1961).

[4] A. Salam, *Elementary Particle Physics*. (1968). Reprinted in Gauge Theory of Weak and Electromagnetic Interactions, C.H. Lai, ed.(Singapore: World Scientific, 1981).

[5] S. Weinberg, Phys. Rev. Lett. **19**, 1264 (1967).

[6] P.W. Higgs, Phys. Lett. **12**, 132 (1964).

[7] F. Englert and R. Brout, Phys. Rev. Lett. **13**, 321 (1964).

[8] G.S. Guralnik, C.R. Hagen and T.W.B. Kibble, Phys. Rev. Lett. **13**, 585 (1964).

[9] Super-Kamiokande Coll., Y. Fukuda et al., Phys. Rev. Lett. **81**, 1562 (1998).

[10] SNO Coll., Q.R. Ahmad et al., Phys. Rev. Lett. **87**, 071301 (2001).

[11] R. Kerger, *A Search for Lepton Flavor Violating Transitions* $e \leftrightarrow \tau$ *via Leptoquarks in* e^+p *Scattering with the ZEUS Detector at HERA*. Ph.D. Thesis, Bonn University, Bonn (Germany), Report BONN-IR-01-01, 2001, available on `http://www-zeus.physik.uni-bonn.de/german/phd.html`.

[12] N. Cabibbo, Phys. Rev. Lett. **10**, 531 (1963).

[13] M. Kobayashi and T. Maskawa, Prog. Theor. Phys. **49**, 652 (1973).

[14] CDF Coll., F. Abe et al., Phys. Rev. Lett. **74**, 2626 (1995).

[15] DØ Coll., S. Abachi et al., Phys. Rev. Lett. **74**, 2632 (1995).

[16] DONUT Coll., K. Kodama et al., Phys. Lett. **B 504**, 218 (2001).

[17] P.D.B. Collins, A.D. Martin and E.J. Squires, *Particle Physics and Cosmology*. John Wiley & Sons, New York, 1989.

[18] H.P. Nilles, Phys. Rep. **110**, 1 (1984).

[19] R.S. Chivukula, Preprint hep-ph/0011264, 2000.

[20] I.A. D'Souza and C.S. Kalman, *PREONS – Models of Leptons, Quarks and Gauge Bosons as Composite Objects*. World Scientific, Singapore, 1992.

[21] R.J. Cashmore et al., Phys. Rep. **122**, 275 (1985).

[22] E.J. Eichten, K.D. Lane and M.E. Peskin, Phys. Rev. Lett. **50**, 811 (1983).

[23] R. Rückl, Phys. Lett. **B 129**, 363 (1983).

[24] F. Boudjema and A. Djouadi, Phys. Lett. **B 240**, 485 (1990).

[25] M. Kuze, for the ZEUS and H1 Coll., Preprint hep-ex/0106030, 2001. To appear in *Proc. 15th Renc. de Physique de la Vallee d'Aoste: Results and Perspective in Particle Physics*, La Thuile, Italy, March 2001.

[26] F.E. Low, Phys. Rev. Lett. **14**, 238 (1965).

[27] J.C. Pati, A. Salam and J. Strathdee, Phys. Lett. **B 59**, 265 (1975).

[28] H. Terazawa, Phys. Rev. **D 22**, 184 (1980).

[29] M.E. Peskin, *Proc. Lepton-Photon Symposium, Bonn*, W. Pfeil (ed.), p. 880. (1981).

[30] R. Kögerler, *Proc. DESY Workshop on Electroweak Interactions at High Energies*, R. Kögerler and D. Schildknecht (eds.), p. 296. (1982).

[31] R. Barbieri, *Proc. DESY Workshop on Electroweak Interactions at High Energies*, R. Kögerler and D. Schildknecht (eds.), p. 325. (1982).

[32] H. Harari, *Proc. DESY Workshop on Electroweak Interactions at High Energies*, R. Kögerler and D. Schildknecht (eds.), p. 334. (1982).

[33] R.D. Peccei, *Gauge Theories of the Eighties, Proc. Arctic School of Physics 1982, Äkäslompolo, Finland*, Lecture Notes in Physics, No. 181, p. 355. Springer, Berlin (1983). Also in preprint 181.

[34] H. Fritzsch, *Gauge Theories of the Eighties, Proc. Arctic School of Physics 1982, Äkäslompolo, Finland*, Lecture Notes in Physics, No. 181, p. 387. Springer, Berlin (1983). Also in preprint 181.

[35] L. Lyons, Prog. Part. Nucl. Phys. **10**, 227 (1983).

[36] W. Buchmüller, R.D. Peccei and T. Yanagida, Nucl. Phys. **B 227**, 503 (1983).

[37] R.R. Volkas and G.C. Joshi, Phys. Rep. **159**, 303 (1988).

[38] H. Harari, Phys. Lett. **B 86**, 83 (1979).

[39] M.A. Shupe, Phys. Lett. **B 86**, 87 (1979).

[40] H. Harari and N. Seiberg, Phys. Lett. **B 98**, 269 (1981).

[41] H. Fritzsch and G. Mandelbaum, Phys. Lett. **B 102**, 319 (1981).

[42] K. Hagiwara, S. Komamiya and D. Zeppenfeld, Z. Phys. **C 29**, 115 (1985).

[43] U. Baur, M. Spira and P.M. Zerwas, Phys. Rev. **D 42**, 815 (1990).

[44] F. Boudjema, A. Djouadi and J.L. Kneur, Z. Phys. **C 57**, 425 (1993).

[45] CDF Coll., F. Abe et al., Phys. Rev. Lett. **77**, 438 (1996).

[46] H1 Coll., C. Adloff et al., Z. Phys. **C 74**, 191 (1997).

[47] ZEUS Coll., J. Breitweg et al., Z. Phys. **C 74**, 207 (1997).

[48] K. Akama, K. Katsuura and H. Terazawa, Phys. Rev. **D 56**, 2490 (1997).

[49] Muon g–2 Coll., H.N. Brown et al., Phys. Rev. Lett. **86**, 2227 (2001).

[50] K. Lane, Preprint hep-ph/0102131, 2001.

[51] S. Rakshit, Preprint hep-ph/0111083, 2001.

[52] Y.-B. Dai, C.-S. Huang and A. Zhang, J. Phys. **G 28**, 139 (2002).

[53] P. Das, S.K. Rai and S. Raychaudhuri, Preprint hep-ph/0102242, 2001.

[54] M. Hayakawa and T. Kinoshita, Preprint hep-ph/0112102, 2001.

[55] CDF Coll., F. Abe et al., Phys. Rev. Lett. **77**, 5336 (1996).

[56] CDF Coll., F. Abe et al., Phys. Rev. **D 55**, 5263 (1997).

[57] DØ Coll., B. Abbott et al., Phys. Rev. Lett. **80**, 666 (1998).

[58] DØ Coll., B. Abbott et al., Phys. Rev. Lett. **82**, 2457 (1999).

[59] DØ Coll., B. Abbott et al., Phys. Rev. Lett. **82**, 4769 (1999).

[60] DØ Coll., B. Abbott et al., Phys. Rev. **D 62**, 031101 (2000).

[61] CDF Coll., T. Affolder et al., Phys. Rev. Lett. **87**, 231803 (2001).

[62] L3 Coll., M. Acciarri et al., Phys. Lett. **B 502**, 37 (2001).

[63] The ALEPH, DELPHI, L3 and OPAL Collaborations and the LEP Exotica Working Group, *Search for Excited Leptons: Preliminary Combined Results of the LEP Experiments*. LEP Exotica WG 2001-02, DELPHI 2001-120 CONF 543, L3 Note 2705, OPAL Technical Note TN701, 2001. Preliminary LEP results to be presented at EPS01 and LP01.

[64] H1 Coll., I. Abt et al., Nucl. Phys. **B 396**, 3 (1993).

[65] H1 Coll., S. Aid et al., Nucl. Phys. **B 483**, 44 (1997).

[66] H1 Coll., C. Adloff et al., Eur. Phys. J. **C 17**, 567 (2000).

[67] H1 Coll., C. Adloff et al., Phys. Lett. **B 525**, 9 (2002).

[68] T. Köhler, *Suche nach angeregten Leptonen mit dem H1-Detektor*. Ph.D. Thesis, RWTH Aachen, 1995. In German.

[69] ZEUS Coll., M. Derrick et al., Phys. Lett. **B 316**, 207 (1993).

[70] ZEUS Coll., M. Derrick et al., Z. Phys. **C 65**, 627 (1995).

[71] ZEUS Coll., J. Breitweg et al., Z. Phys. **C 76**, 631 (1997).

[72] ZEUS Coll., S. Chekanov et al., Preprint DESY-01-132 (hep-ex/0109018), 2001. Subm. to Phys. Lett. B.

[73] A. Sabetfakhri, *A Search for Electron and Neutrino Compositeness in ep Collisions at HERA*. Ph.D. Thesis, University of Toronto, 2000.

[74] G.A. Voss and B.H. Wiik, Ann. Rev. Nucl. Part. Sci. **44**, 413 (1994).

[75] M. Seidel, *The Upgraded Interaction Regions of HERA* (unpublished). DESY-HERA-00-01.

[76] ZEUS Coll., U. Holm (ed.), *The ZEUS Detector*. Status Report (unpublished), DESY (1993), available on `http://www-zeus.desy.de/bluebook/bluebook.html`.

[77] N. Harnew et al., Nucl. Inst. Meth. **A 279**, 290 (1989).

[78] B. Foster et al., Nucl. Phys. Proc. Suppl. **B 32**, 181 (1993).

[79] B. Foster et al., Nucl. Inst. Meth. **A 338**, 254 (1994).

[80] M. Derrick et al., Nucl. Inst. Meth. **A 309**, 77 (1991).

[81] A. Andresen et al., Nucl. Inst. Meth. **A 309**, 101 (1991).

[82] A. Caldwell et al., Nucl. Inst. Meth. **A 321**, 356 (1992).

[83] A. Bernstein et al., Nucl. Inst. Meth. **A 336**, 23 (1993).

[84] J. Krüger, *The Uranium Scintillator Calorimeter for the ZEUS Detector at the Electron - Proton collider HERA: The Heart of ZEUS*. Habilitation Thesis, Universität Hamburg, Report DESY-F35-92-02, 1992.

[85] H. Bethe and W. Heitler, Proc. Roy. Soc. Lond. **A146**, 83 (1934).

[86] J. Andruszków et al., Report DESY-92-066, DESY, 1992.

[87] ZEUS Coll., M. Derrick et al., Z. Phys. **C 63**, 391 (1994).

[88] ZEUS Luminosity Group, J. Andruszków et al., Acta Phys. Pol. **B 32**, 2025 (2001).

[89] R.G. Roberts, *The Structure of the Proton – Deep Inelastic Scattering*. Cambridge University Press, Cambridge, 1990.

[90] W. Buchmüller and G. Ingelman, *Proceedings of the Workshop on Physics at HERA, Volumes I and II*, 1991.

[91] *Future Physics at HERA Volumes I and II*, ed. G. Ingelman, A. De Roeck, R. Klanner, 1996.

[92] G. Wolf, Preprint DESY-94-022, 1994.

[93] H. Abramowicz and A. Caldwell, Rev. Mod. Phys. **71**, 1275 (1999).

[94] A.M. Cooper-Sarkar, R.C.E. Devenish and A. De Roeck, Int. J. Mod. Phys. **A 13**, 3385 (1998).

[95] G. Wolf, Preprint hep-ex/0105055, 2001.

[96] U.F. Katz, *Deep-Inelastic Positron–Proton Scattering in the High-Momentum-Transfer Regime of HERA*, Springer Tracts in Modern Physics, Vol. 168. Springer, Berlin, Heidelberg, 2000.

[97] ZEUS Coll., J. Breitweg et al., Eur. Phys. J. **C 11**, 427 (1999).

[98] ZEUS Coll., J. Breitweg et al., Eur. Phys. J. **C 12**, 411 (2000).

[99] A. Kappes, *Verwendung von Neuronalen Netzen zur Identifikation des gestreuten Elektrons in ep-Ereignissen mit hohem Q^2 bei ZEUS*. Diploma Thesis, Universität Bonn, Bonn, Germany, Report BONN-IB-97-28, 1997.

[100] A. Kappes, *Measurement of $e^- p \to e^- X$ Differential Cross Sections at High Q^2 and of the Structure Function xF_3 with ZEUS at HERA*. Ph.D. Thesis, Bonn University, Bonn (Germany), Report BONN-IR-2001-16, 2001, available on `http://www-zeus.physik.uni-bonn.de/german/phd.html`.

[101] H. Abramowicz, A. Caldwell and R. Sinkus, Nucl. Inst. Meth. **A 365**, 508 (1995).

[102] R. Sinkus and T. Voss, Nucl. Inst. Meth. **A 391**, 360 (1997).

[103] R. Brun et al., GEANT3, Technical Report CERN-DD/EE/84-1, CERN, 1987.

[104] K. Charchula, G.A. Schuler and H. Spiesberger, Comp. Phys. Comm. **81**, 381 (1994).

[105] H. Spiesberger, DJANGO6 *Version 2.4 – A Monte Carlo Generator for Deep Inelastic Lepton Proton Scattering Including QED and QCD Radiative Effects*, 1996, available on `http://www.desy.de/~hspiesb/django6.html`.

[106] CTEQ Coll., H.L. Lai et al., Eur. Phys. J. **C 12**, 375 (2000).

[107] G. Ingelman, A. Edin and J. Rathsman, Comp. Phys. Comm. **101**, 108 (1997).

[108] T. Sjöstrand, Comp. Phys. Comm. **39**, 347 (1986).

[109] T. Sjöstrand and M. Bengtsson, Comp. Phys. Comm. **43**, 367 (1987).

[110] T. Sjöstrand, Comp. Phys. Comm. **82**, 74 (1994).

[111] L. Lönnblad, Comp. Phys. Comm. **71**, 15 (1992).

[112] G. Marchesini et al., Comp. Phys. Comm. **67**, 465 (1992).

[113] H.L. Lai et al., Phys. Rev. **D 55**, 1280 (1997).

[114] M. Glück, E. Reya and A. Vogt, Phys. Rev. **D 46**, 1973 (1992).

[115] T. Carli et al., *Proc. Workshop on Physics at HERA*, W. Buchmüller and G. Ingelman (eds.), Vol. 3, p. 1468. Hamburg, Germany, DESY (1992).

[116] H.J. Kim and S. Kartik, Preprint LSUHE-145-1993, 1993.

[117] Ch. Berger and W. Wagner, Phys. Rep. **146**, 1 (1987).

[118] F.W. Brasse et al., Nucl. Phys. **B 39**, 421 (1972).

[119] A.D. Martin, R.G. Roberts and W.J. Stirling, Phys. Rev. **D 50**, 6734 (1994).

[120] H. Plothow-Besch, *PDFLIB, CERN Program Library Entry W5051.* CERN, Geneva, 1995.

[121] O. Helene, Nucl. Inst. Meth. **212**, 319 (1983).

[122] Particle Data Group, R.M. Barnett et al., Phys. Rev. **D 54**, 1 (1996).

[123] ZEUS Coll., *Search for Excited Electrons in e^+p Collisions at HERA.* Abstract 758, International Conference on High Energy Physics, Vancouver, Canada, 1998.

[124] ZEUS Coll., *Search for Excited Fermions in ep Collisions at HERA.* Contributed paper 555 to EPS '99, Tampere, Finland, 1999.

[125] ZEUS Coll., *Search for Excited Fermions in ep Collisions at HERA.* Abstract 1040, XXXth International Conference on High Energy Physics, Osaka, Japan, 2000.

[126] ZEUS Coll., *Search for Excited Fermions in ep Collisions at HERA.* Abstract 607, International Europhysics Conference on High Energy Physics, Budapest, Hungary, 2001.

[127] T. Helbig and H. Spiesberger, Nucl. Phys. **B 373**, 73 (1992).

[128] H. Spiesberger, private communication, 2001.

Acknowledgements

It is due to many people in Bonn and Hamburg that my time as a doctoral candidate was enjoyable and has led to successful results. My thanks must first go to my supervisor Erwin Hilger, who gave me the freedom to proceed with my work as I wished. At the same time, he could always be counted on for very helpful discussions and for strong support in any respect.

It is also a pleasure to thank Uli Katz and Masahiro Kuze for particularly valuable advice and fruitful discussions. Their wisdom has provided me with many new insights.

I am grateful to Stefano Dusini, Andrea Parenti and Ali Sabetfakhri for their cooperation on the topic of excited-fermion searches, which was both helpful and pleasant. I would also like to thank Lorenzo Bellagamba, Elisabetta Gallo, Roberto Sacchi and Bruce Straub for their coordinating activities in the ZEUS exotics physics group and for much useful advice.

The presence of my office mate Alexander Kappes has been very beneficial to my work due to much software-related help and various interesting discussions on both physical and non-physical topics. Many thanks also go to my other colleagues in Bonn, Detlef Bartsch, Robert Kerger, Julian Rautenberg and Meng Wang, for answering numerous questions and for providing an extremely pleasant group atmosphere. Special thanks to Alexander and Julian for maintaining our local computer cluster in such an outstanding way.

As experimental particle physics is a collaborative effort, the results presented in this thesis could not have been obtained without hardware and software contributions by a large number of people at DESY. Their work is gratefully acknowledged.

Finally, I sincerely thank my parents and my dear Sabine for giving me so much love and support.